Synthesis and Processing of High Entropy Materials and their Integration into Lithium Batteries

TECHNISCHE UNIVERSITÄT DARMSTADT

Vom Fachbereich Material- und Geowissenschaften
der Technischen Universität Darmstadt

zur Erlangung des akademischen Titels
Doktor-Ingenieur (Dr.-Ing.)

genehmigte Dissertation von
Yanyan Cui

Betreuer: Prof. Dr.-Ing. Horst Hahn,
Gutachter: Prof. Dr. Bai-Xiang Xu

Darmstadt 2022

Yanyan Cui: Research in the Field of high entropy materials for lithium ion batteries

Darmstadt, Technische Universität Darmstadt,

Year thesis published in TUprints 2023

Date of the viva voce 02. 12. 2022

Ehrenwörtliche Erklärung

Ich erkläre hiermit ehrenwörtlich, dass ich die vorliegende Arbeit selbstständig angefertigt habe. Sämtliche aus fremden Quellen direkt oder indirekt übernommenen Gedanken sind als solche kenntlich gemacht.

Die Arbeit wurde bisher keiner anderen Prüfungsbehörde vorgelegt und noch nicht veröffentlicht.

Darmstadt, den 02. 12. 2022

Abstract

With the increasing demand for renewable energy sources such as solar, geothermal, and wind energy, the development of efficient energy storage devices is necessary. Lithium-ion batteries (LIBs) have been considered a potentially revolutionary technology for storing renewable energy due to their advantages of low self-discharge, long life span, high output voltage, and high energy density [1]. Over the past few decades, LIBs have undergone extensive development in both industry and academia. In current LIB technology, the cell voltage and capacity are primarily determined by the electrode materials, which also dominate the battery cost. Therefore, exploring alternative electrode materials and investigating their structure-composition-performance relationships is essential for further development.

Recently, the use of the high entropy concept to develop materials is gaining significant interest. The high entropy concept is derived from high entropy alloys (HEAs), which possess high configurational entropy (S_{config}) by incorporating 5 or more elements into a single-phase structure, leading to the so-called "cocktail effect", where the multiple synergies among the constituent elements may result in additional or changed properties. That means HEMs can have the potential to outperform the parent material system. Inspired by the high entropy concept, high entropy oxides (HEOs) were investigated as a new class of conversion electrode materials for LIBs, which show unexpected reversibility due to their unique structural stability. These unexpected findings have stimulated many recent studies on the performance of high entropy materials in electrochemical energy storage devices.

In this work, a new photonic curing method was used to synthesize high entropy oxides for more rapid and efficient synthesis. The material was used as a binder-free electrode material for LIBs. Since HEO has a high mixed lithium-ion and electronic conductivity at room temperature, HEO was also synthesized by the photonic curing method for coating on NCM851005. In addition, the mechanism as a coating material for performance improvement was investigated. Inspired by the application of HEO as a conversion electrode material as an anode, high-entropy fluorides (HEFs), as conversion materials, were synthesized and used as cathode materials for LIBs and their underlying storage mechanisms were investigated. Due to the elemental dissolution of metal fluorides during cycling, high entropy oxides have also been studied as a coating for HEFs.

The application and research of high entropy materials in electrode materials provide new guidelines for designing and manufacturing new electrode materials for LIBs.

Zusammenfassung

Angesichts der steigenden Nachfrage nach erneuerbaren Energiequellen wie Solar-, Erdwärme- und Windenergie ist die Entwicklung effizienter Energiespeicher erforderlich. Lithium-Ionen Batterien (LIBs) werden aufgrund ihrer Vorteile wie geringe Selbstentladung, lange Lebensdauer, hohe Ausgangsspannung und hohe Energiedichte als potenziell revolutionäre Technologie zur Speicherung erneuerbarer Energien angesehen. In den letzten Jahrzehnten wurden LIBs sowohl in der Industrie als auch im akademischen Bereich intensiv weiterentwickelt. Bei der derzeitigen LIB-Technologie werden die Zellspannung und -kapazität in erster Linie durch die Elektrodenmaterialien bestimmt, die auch die Batteriekosten dominieren. Daher ist die Erforschung alternativer Elektrodenmaterialien und die Untersuchung der Beziehungen zwischen Struktur, Zusammensetzung und der erzielten Leistung für die Weiterentwicklung von entscheidender Bedeutung.

In letzter Zeit gewinnt die Anwendung des Konzepts der hohen Entropie zur Entwicklung von Materialien stark an Interesse. Das Konzept der hohen Entropie leitet sich von Hochentropielegierungen (HEAs) ab, die eine hohe Konfigurationsentropie (Sconfig) aufweisen, indem fünf oder mehr Elemente in einer einphasigen Struktur eingebaut sind, was zum so genannten "Cocktaileffekt" führt, bei dem die vielfältigen Synergien zwischen den Bestandteilen zu zusätzlichen oder veränderten Eigenschaften führen können. Das bedeutet, dass Hochentropiematerialien (HEMs) das Potenzial haben können, das Ausgangsmaterialsystem zu übertreffen. Inspiriert durch das Konzept der hohen Entropie wurden Hochentropieoxide (HEOs) als neue Klasse von Konversionselektrodenmaterialien für LIBs untersucht, die aufgrund ihrer einzigartigen strukturellen Stabilität eine unerwartete Reversibilität aufweisen. Diese unerwarteten Ergebnisse haben in jüngster Zeit viele Studien über die Leistung von HEMs in elektrochemischen Energiespeichern angeregt.

In dieser Arbeit wurde eine neue photonische Aushärtungsmethode für die Synthese von Hochentropieoxide verwendet, um eine schnellere und effizientere Synthese zu erzielen. Das Material wurde als bindemittelfreies Elektrodenmaterial für LIBs verwendet. Da HEO eine hohe gemischte Lithium-Ionen und elektronische Leitfähigkeit bei Raumtemperatur aufweist, wurde HEO durch die photonische Aushärtungsmethode zur Beschichtung von NCM851005 synthetisiert. Darüber hinaus wurde der Mechanismus als Beschichtungsmaterial zur Leistungsverbesserung untersucht. Inspiriert durch die Anwendung von HEO als Konversionselektrodenmaterial in der Anode wurden Hochentropiefluoride (HEFs) als Konversionsmaterialien synthetisiert und als Kathodenaktivmaterialien für LIBs verwendet und

ihre zugrunde liegenden Speichermechanismen untersucht. Aufgrund der elementaren Auflösung von Metall Fluoriden während des Zyklisierens, wurden auch Oxide mit hoher Entropie als Beschichtung für HEFs untersucht.

Die Anwendung und Erforschung von HEMs bei Elektrodenmaterialien liefern neue Leitlinien für die Entwicklung und Herstellung neuer Elektrodenmaterialien für LIBs.

Content

Chapter 1

1. Introduction

1.1. Background of lithium-ion batteries

At present, the severe air pollution from fossil fuels and potential hazards brought by radioactive nuclear waste have driven policies and communities to seek new, green, and renewable energy sources such as wind, solar, geothermal, and hydroelectric power [2]. Simultaneously, the generated electrical energy requires a balanced supply and convenient energy storage devices. Lithium-ion batteries (LIBs) have recently been considered a potentially revolutionary technology for storing renewable energy due to their low self-discharge, long life span, high output voltage, and high energy density [1]. Moreover, they have achieved wide use in electronics, power tools, and hybrid/full-electric vehicles, which have significantly changed our lives since their commercialization [3]. Given its fundamental advantages, the demand and quality of rechargeable lithium batteries will continue to grow with the successful development of flexible electronic devices and electric vehicles. Therefore, LIBs are gaining intense interest from industry and government funding agencies, and research in this field has been abounded in recent years. In general, the performance of LIBs (e.g., cell potential, capacity, or energy density) is related to the intrinsic properties of their electrode material [4]. Electrodes with higher rate capability, higher charge capacity, and sufficiently high voltage can improve the energy and power densities of LIBs and make them smaller and cheaper [5]. A great deal of research on LIBs has been in the optimization of electrode materials to address both energy and power demands of secondary LIBs for future energy storage applications.

1.1.1. The working principle of Li-ion batteries

Generally, a LIB contains an anode, a cathode, an ionically conductive and electronically insulating medium, an electrolyte between the electrodes [6]. The active component in the cathode is typically a material that can incorporate Li-ions through intercalation, e.g. lithium cobalt oxide

($LiCoO_2$) and lithium iron phosphate ($LiFePO_4$) [7]. The anode is typically composed of graphite, while lithium metal anodes are as well under investigation [8]. The state-of-the-art LIB contains a polymer electrolyte that is usually composed of polyethylene oxide (PEO) as a host matrix infiltrated with an ionically conductive solution of, e.g., $LiPF_6$ or LPSCl. A purely liquid electrolyte consisting of a solution of a lithium salt (e. g., $LiPF_6$, LTFSI) in a mixed organic solvent (e. g., ethylene carbonate–dimethyl carbonate, EC–DMC) embedded in a separator is as well utilized [9, 10]. In addition, the system is packed in an Aluminum plastic film or stainless-steel shell. Figure 1-1 summarizes recent developments and the technological status of a typical LIB configuration, including the cathode, the anode, and the electrolyte.

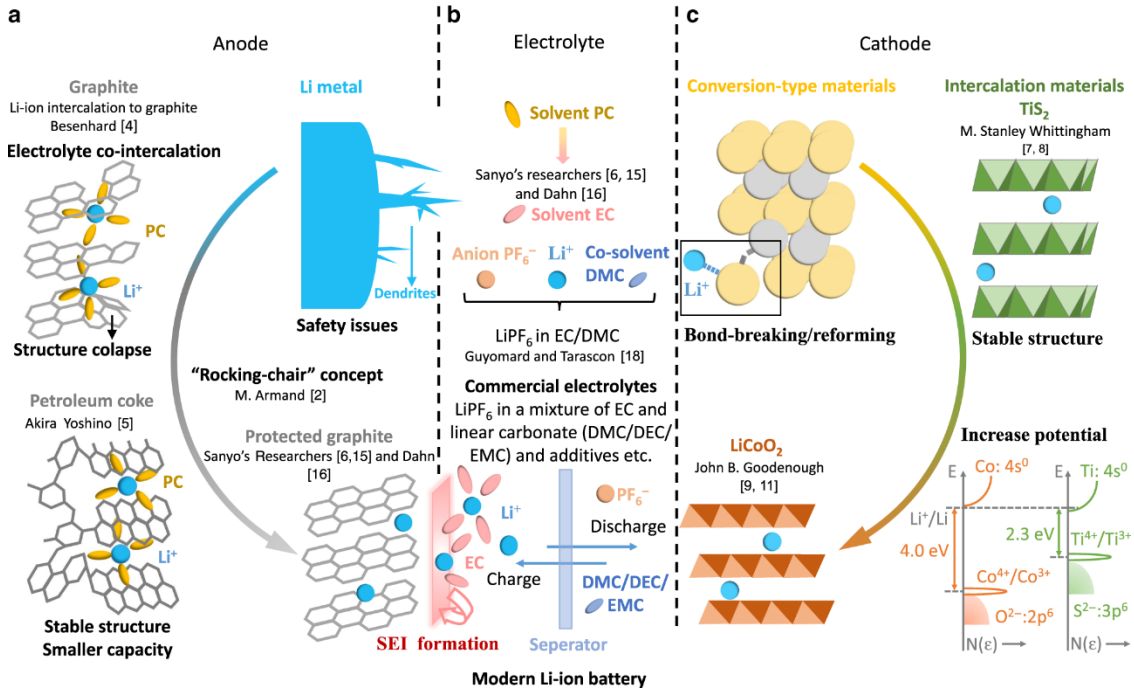

Figure 1-1: Milestone discoveries shaped modern lithium-ion batteries. The development of (a) anode materials including lithium metal, petroleum coke, and graphite, (b) electrolytes with the solvent propylene carbonate (PC), a mixture of ethylene carbonate (EC), and at least one linear carbonate selected from dimethyl carbonate (DMC), diethyl carbonate (DEC), ethyl methyl carbonate (EMC) and many additives, (c) cathode materials including conversion-type materials, intercalation materials titanium disulfide (TiS_2) and lithium cobalt oxide ($LiCoO_2$) [11].

The anode and cathode are capable of storing lithium ions, which migrate back and forth between the negative and positive electrodes upon discharging/charging via the electrolyte, while electrons do so similarly via the outer electrical circuit. For example, in the first commercialized lithium-ion batteries of $Li_xC_6/Li_{1-x}CoO_2$ cell as shown in Figure 1-2, during discharge, lithium ions diffuse from a lithiated graphite (Li_xC_6) structure (the anode) into a delithiated $Li_{1-x}CoO_2$ structure (the cathode) with concomitant oxidation and reduction of the two electrodes, respectively, releasing the stored

energy [12]. When the battery cell is charging, the lithium ions move back via the electrolyte to the graphite anode, taking in and storing energy. In both cases, the flow of electrons follows with the ions through the outer circuit.

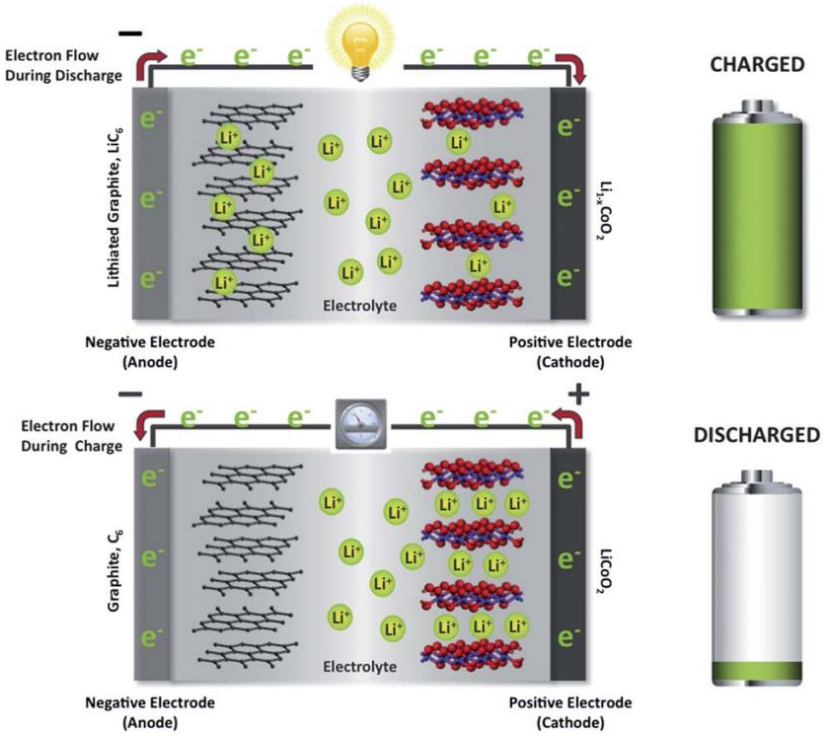

Figure 1-2: A schematic illustration of the working principles of a $Li_xC_6/Li_{1-x}CoO_2$ lithium-ion cell [12].

1.2. Electrode materials

In general, electrode materials for Li-ion batteries can be classified as intercalation type, conversion type, and alloy type according to their dominant Li-ion storage mechanism [13]. Typical intercalation electrodes possess intrinsic one, two, or three-dimensional diffusion pathways to facilitate Li-ion transport without any severe (irreversible) deterioration of the initial crystal structure and with very low volume variation, which allows for excellent cycle stability and good capacity retention [14]. The classic intercalation-type cathode material, i.e., $LiNi_{1-y-z}Mn_yCo_zO_2$, $LiFePO_4$, and $Li_4Ti_5O_{12}$, have reached the market at different stages, bringing about incremental performance improvements [15]. Differently, the alloying-type materials (Si, Sn, Ge, or Zn) provide high lithium storage capacities, commonly exceeding one lithium ion per atom of the alloying element by direct bonding between inserted Li-ions and the host element with the formation of composite alloys (e.g., $Li_{15}Si_4$ or $Li_{4.4}Sn$) [16]. However, extensive volume changes lead to continuous exposure of the fresh surface to the electrolyte, resulting in continuous electrolyte decomposition and formation of solid electrolyte interphase (SEI), limiting the cycle life of such electrodes. The conversion reaction happens when Li-ions are inserted into nano-sized binary

compounds as denoted by MX (M for transition metals, e.g. Fe, Co, Cu, and X for anions like O, S, F), and results in a reduction of M cations to M0 and formation of LiX, which leads to higher capacities than those achieved using intercalation-based compounds [17]. Generally, the three mechanisms differ significantly in the charge storage of electrode materials, resulting in different electrode capacity, morphology, and structure. A schematic representation of the different reaction mechanisms of intercalation, alloying and conversion observed in electrode materials is shown in Figure 1-3.

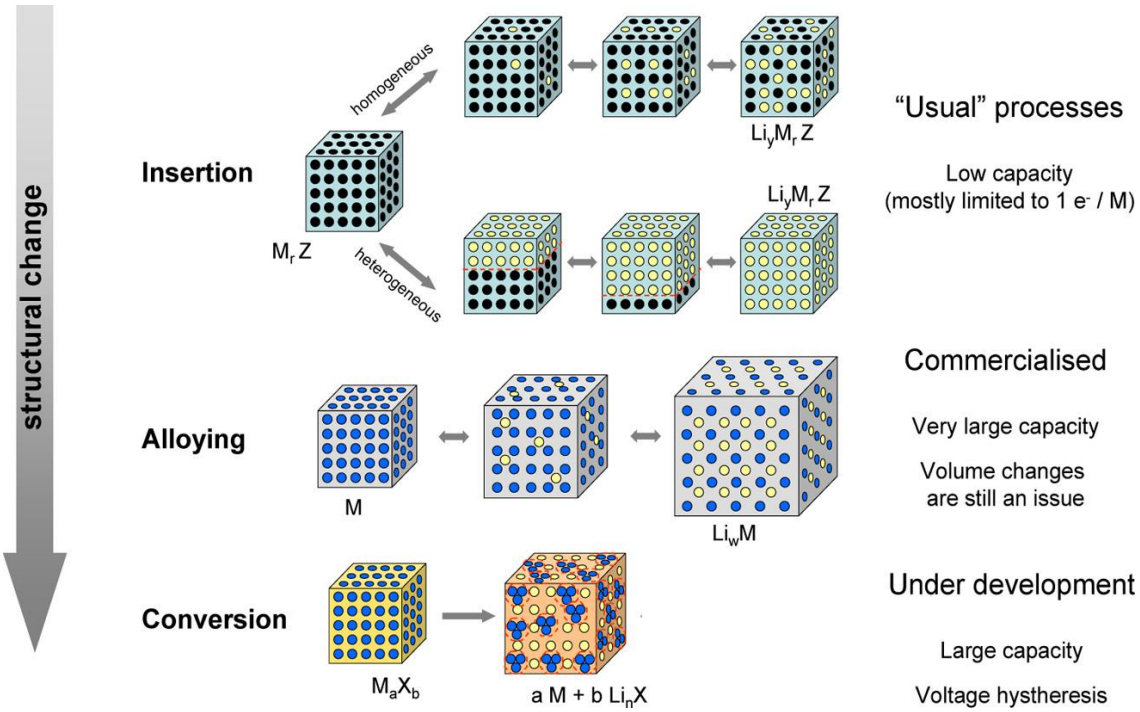

Figure 1-3: A schematic representation of the different reaction mechanisms observed in electrode materials for lithium batteries. Black circles: voids in the crystal structure, blue circles: metal, yellow circles: lithium [13].

1.2.1. $LiNi_{1-y-z}Mn_yCo_zO_2$ based insertion type materials

An intercalation cathode is a solid host network that stores guest ions. The guest ions can be inserted into and be removed from the host network reversibly. Li^+ is the guest ion in a Li-ion battery, and the host network compounds are metal chalcogenides, transition metal oxides, and polyanion compounds [18]. These intercalation compounds can be divided into several crystal structures, such as layered (e.g., $LiCoO_2$, $LiNi_{1/3}Mn_{1/3}Co_{1/3}O_2$, $LiTiS_2$), spinel (e.g., $LiMn_2O_4$, $LiCo_2O_4$), olivine (e.g., $LiFePO_4$, $LiMnPO_4$), and tavorite (e.g., $LiFeSO_4F$, $LiVPO_4F$). Compared to all other cathode materials, the layered transition metal (TM) oxides have attracted extensive interest due to their high theoretical capacity of ~ 280 mAh g^{-1} compared to ~ 170 mAh g^{-1} for olivine and ~ 150 mAh g^{-1} for tavorite [19–21].

$LiCoO_2$

$LiCoO_2$ (LCO) was discovered by replacing the Na in Na_xCoO_2 with Li and proposed as a cathode material by Goodenough in 1979 [22]. It has a well-ordered α-$NaFeO_2$-type layered structure with oxygen atoms arranged in a cubic close-packed (ccp) framework and the Li^+ and Co^{3+} ions ordered in alternating (111) planes of $R\bar{3}m$ space group. In 1991, the LIBs with LCO as cathode and nongraphitizable carbon as an anode was firstly commercialized by Sony [23]. Since then, LCO has dominated the cathode materials market for nearly 30 years in the field of portable electronics due to its unique advantages, including the high theoretical capacity of 274 mAh g^{-1}, the high theoretical volumetric capacity of 1363 mAh cm^{-3}, low self-discharge, high discharge voltage, and good cycling performance [24]. However, the high cost of cobalt makes LCO expensive and toxic. Moreover, the practical discharge capacity for LCO is only ~ 140 mAh g^{-1} due to the limitation of only 0.5 mol of Li^+ ions per formula extract from $LiCoO_2$ with a cutoff voltage of 4.2 V to avoid rapid capacity decay [25]. In principle, all Li^+ in LCO could be extracted. However, when the lithium was removed from bulk LCO, Co^{3+} is oxidized to Co^{4+} in an unstable oxidation state, and once the fraction of lithium removed exceeded 0.5 mol, peroxide on the surface, resulting in the loss of O_2 and instability of the structure [26]. Charging to higher voltages is the most promising and effective way to extract more lithium-ions from LCO to increase capacity. However, at voltages >4.2 V, the dissolution of cobalt in the electrolyte and its irreversible phase transition from hexagonal to monoclinic phase lead to a rapid decrease in the cycling efficiency and discharge capacity. At voltages >4.55 V, the phase transition from O3 to the H1-3 host occurs while the c-lattice parameter decreases significantly and volume shrinkage in bulk LCO particles is observed, with the consequence of decrease, which leads to increased concentration gradients and large internal strains.

To meet the demand for high energy density of LIBs with a stable cycling performance, various strategies, including element doping, surface coating, and co-modification approaches, have been made to overcome the issues of $LiCoO_2$. For example, Mg, Al, and Ti were used for doping to increase the electronic conductivity of host materials, stabilize the structure and inhibit the dissolution of Co, and stabilize the surface oxygen at high voltages, respectively [27–29]. Al_2O_3, ZrO_2 and metal fluorides were synthesized as coating layers to protect the electrode surface, which is usually the starting point of the failure process [30–32]. Besides, some work focuses on the electrolyte compatibility with $LiCoO_2$ at high cutoff voltage based on additives, solvents, and lithium salts. So far, the charging voltages of $LiCoO_2$ has been increased to 4.5 V (vs. Li/Li^+), achieving a reversible capacity of ≈180 mAh g^{-1} with good cycling life [33].

$LiMnO_2$

After discovering LCO, considering the low cost, high abundancce, and low toxicity of Mn, Mn-based lithium manganese oxides of layered $LiMnO_2$ and spinel $LiMn_2O_4$ composites were investigated as a promising alternative cathode material for LIBs. However, $LiMn_2O_4$ exhibits a lower theoretical capacity of 145 mAh g^{-1} [34]. The available capacity of the manganese-based cathode material can be increased by using $LiMnO_2$, which contains a more significant initial amount of lithium. $LiMnO_2$ has various crystal structures, including monoclinic (m-$LiMnO_2$, space group $C2/m$), orthorhombic (o-$LiMnO_2$, space group $Pmmn$), and layered $LiMnO_2$ (space group $R\bar{3}m$) with α-$NaFeO_2$-like structure. But only the orthorhombic phase o-$LiMnO_2$ is thermodynamically stable among these structures [34].

$LiMnO_2$ has a high theoretical specific capacity of 285 mAh g, and the higher redox potential of the $Mn^{3+}/^{4+}$ band relative to the oxygen band makes it more chemically stable than LCO. However, this also leads to poor electronic conductivity because of the more significant energy barrier between the manganese and oxygen bands and the electron localization in $Mn^{3+/4+}$ [35]. Besides, the $LiMnO_2$ cathodes in LIBs can hardly display the satisfied electrochemical performance due to the cooperative Jahn–Teller effect (Figure 1-4) and the high-spin state of Mn^{3+}, which leads to an irreversible phase transformation from the layered structure into the spinel structure upon cycling, resulting in rapid voltage and capacity fade. When Mn^{3+} disproportionate into Mn^{4+} and Mn^{2+} when exposed to HF formed by electrolyte degradation, Mn^{2+} rapidly dissolves into the solution. This leads to cathode degradation and is detrimental for the anode after Mn^{2+} deposition on the graphite surface [36,37].

To stabilize the structure and improve the electrochemical stability of layered LiMnO2, various strategies, including doping, coating, surface/bulk structural regulations, and electrolyte modification, have been carried out. For example, Al or Cr was used for substitution to form a phase intermediate between layered and spinel to get a thermodynamically stable state [38,39]. High-temperature LiMnO2 materials transform to spinel-type structures when delithiated during charging but generally show better cycling stability over a wide voltage window than in low-temperature phases.

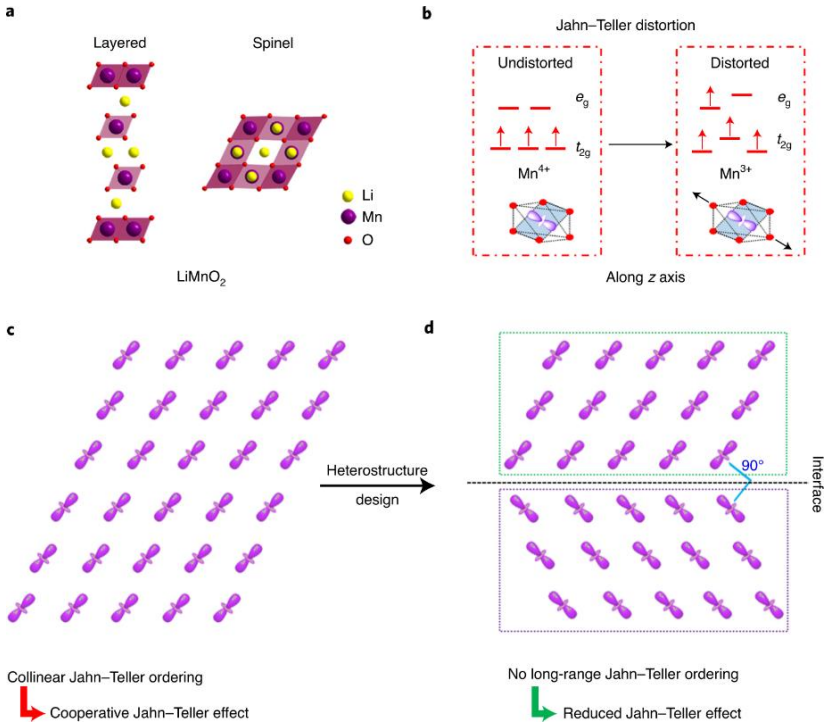

Figure 1-4: Jahn–Teller distortion correlated with orbital ordering in $LiMnO_2$. (a) Crystal structures of spinel and layered $LiMnO_2$. (b) Splitting the levels of d orbitals in an octahedral environment because of Jahn–Teller distortion. (c) Cooperative Jahn–Teller distortion with collinear orbital ordering. (d) Alleviated Jahn–Teller distortion with interfacial orthogonal orbital sequence [37].

$LiNiO_2$

$LiNiO_2$, which has a relatively high energy density and low cost compared to cobalt-based materials, has also attracted attention. It has a similar theoretical specific capacity of 275 mAh g^{-1} as $LiCoO_2$, and it also has the same α-$NaFeO_2$ layered structure, with Li^+ and Ni^{3+} occupying octahedral sites in the (111) plane [40].

In contrast to Co and Mn, Ni shows moderate structural and chemical stabilities as Ni^{3+} has higher OSSE (octahedral site stabilization energy, i.e., a small difference between the crystal field stabilization energies in the octahedral and tetrahedral sites [41]) than Mn^{3+}, lower OSSE than Co^{3+} and the low-spin of Ni^{3+}. However, pure stoichiometric LNO cathodes are challenging to synthesize. It always exists as $Li1\text{-}yNi_{1+y}O_2$ because of the cation mixing disorder between Ni^{2+} and Li+ due to the radius of Ni^{2+} (0.69 Å) being similar to that of Li^+ (0.76 Å)[42]. Cation mixing shifts the hierarchical $R\bar{3}m$ space group of LNO to the tightly packed spinel $Fd\bar{3}m$ space group, which leads to shorter ion spacing and more extensive interactions, making Li^+ diffusion difficult [43]. Besides, the presence of Ni^{3+}, which is usually reduced to Ni^{2+} during the synthesis process and continuously occupies Li sites in the Li layer, creating disorder that hinders diffusion of Li ions. Eventually, this leads to poor lithium conductivity and a severe decrease in capacity during the

delithiation process. Secondly, the highly oxidized Ni^{4+} charged materials are thermodynamically unstable. They are easily reduced in reaction with the electrolyte, thus causing a phase change in the material structure from layered to spinel and rock-salt phases. In addition, $LiNiO_2$ undergoes irreversible phase changes during charging, triggering surface oxygen loss, which leads to a severe drop in capacity and cell voltage. Finally, due to the thermal instability of high valence Ni ions and the Jahn-Teller distortion phenomenon, $LiNiO_2$ also exhibits severe thermal instability [44]. Doping has been shown to be as an efficient way to address these problems and improve electrochemical performance; for example, partial replacement of Ni with Co can reduce cationic disorder; doping with Mg can improve thermal stability in a high state of charge (SOC); doping with a small amount of Al can enhance thermal stability and electrochemical properties, and doping with Cu can form a stable, protective layer without destroying the bulk structure. [45]

$LiNi_xCo_yMn_{1-x-y}O_2$

Considering characteristics of the individual elements of layered oxides: $LiCoO_2$ has good cycle stability but a moderate practical capacity [46]; $LiMnO_2$ has good cycle performance, but a severe phase degradation and low preparation efficiency [47]; and $LiNiO_2$ has high energy density but cation mixing disorder [48]. A ternary transition metal material $LiNi_xCo_yMn_{1-x-y}O_2$ (NCM), prepared by mixing different transition metals of nickel-cobalt-manganese based oxides, combining the advantages of $LiCoO_2$, $LiNiO_2$ and $LiMnO_2$ has been proposed as a way to improve their performance as cathode materials in LIBs. In NCM materials, the valences of nickel, cobalt, and manganese cations are usually +2, +3, and +4, respectively [49]. Generally, Co can reduce cation mixing and surface energy by oxidation +3 to +4. In contrast, nickel oxidation from +2 valence to +4 valence can increase the capacity of materials. Simultaneously, Mn remains in a +4-oxidation state that creates a very high energy barrier for cationic diffusion through tetrahedral sites and thus guarantees structural stability during cycling [50] .

NCM has a similar or higher achievable specific capacity than LCO and similar operating voltage while allowing for lower costs by reducing the Co content. In 2001, Ohzuku [51] reported a solid ternary solution with the composition $LiNi_{1/3}Mn_{1/3}Co_{1/3}O_2$ (NMC-111), which provided a capacity of 160 mAh g^{-1} in the voltage window of 2.5-4.4 V and 200 mAh g^{-1} in the voltage window of 2.8-4.6 V. In addition, it also exhibits excellent rate capability and good structural stability at high potentials. This makes NMC-111 a possible alternative to $LiCoO_2$ with potential application as a cathode material for high-energy LIBs for hybrid electric vehicles (HEVs). In addition, NMC-811, NMC-622, and NMC-532 have also been widely studied materials.

Nickel rich $LiNi_xCo_yMn_{1-x-y}O_2$

In pursuit of higher energy density and lower cost, nickel-rich NCM of $LiNi_xCo_yMn_{1-x-y}O_2$ ($x \geq 0.8$) has been proposed [52]. As shown in Figure 1-5, the capacity and stability change with the lithium content.

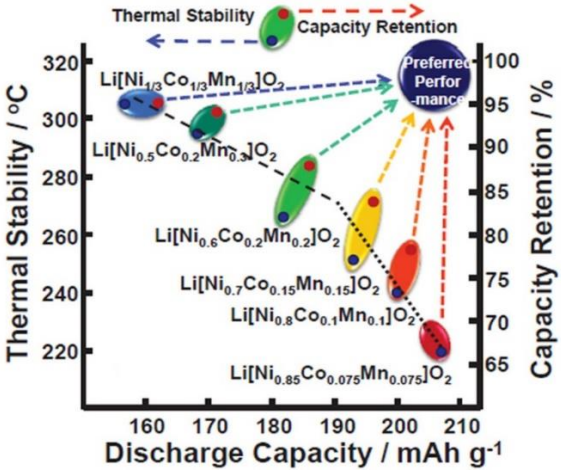

Figure 1-5: A map of the relationship between discharge capacity, thermal stability and capacity retention of $Li/Li[Ni_xCo_yMn_{1-x-y}]O_2$ (x=1/3, 0.5, 0.6, 0.7, 0.8, and 0.85) [53].

However, with the increase of energy density, the thermal and cycling stability also decreases, as some disadvantages similar to LNO appear. First, the higher Ni content implies a severe mixing of Li^+/Ni^{2+} cations during charge/discharge, which will seriously hinder the diffusion of Li ions, leading to a decreased electrochemical performance [54]. In addition, Ni-rich NCMs tend to release surface oxygen accompanied by susceptibility to thermally induced phase transition to spinel and rock-salt structures of NiO phase, which leads to thermal runaway of the battery, especially at the overcharged state [55] . More seriously, residual lithium compounds such as LiOH and Li_2CO_3 are easily formed on the surface of Ni-rich NCM materials during synthesis and storage, which is due to the sensitive Ni^{3+}, resulting in irreversible loss of active lithium [56].

To address these problems, element doping, surface coating, or structure modification were employed to solve specific problems. Element doping promotes the stability of the structure and thermal properties through lattice adjustment at the atomic scale. However, due to the small number of doping elements in the nickel-rich layered transition metal oxide material, it is crucial that the dopants are uniformly distributed and partially replace the elements at the doping site. In addition, surface modification can prevent side reactions between the material and the electrolyte, thus improving its thermal stability and cyclability [57]. For example, La_4NiLiO_8 coating on NCM8111 reduces the oxygen evolution near the cathode surface, inhibits the side reactions on the cathode surface, and maintains the materials structural integrity, resulting in

superior rate capability and cycle stability [58]. Qu et al. recently developed a $Li_{1.3}Al_{0.3}Ti_{1.7}(PO_4)_3$ (LATP) coated Ni-rich NMC using a sol-gel method. The LATP coating improved the structural stability of the material, and, as a result, the cathode exhibited enhanced cycling stability [59].

1.2.2. Conversion type materials

With the rapid development of ultra-high capacity anodes such as silicon anode, lithium metal anode, and carbon-based materials, the commercial intercalation-type transition metal oxide cathode materials (i.e., $LiCoO_2$ (LCO), $LiNiMnCoO_2$ (NMC), and $LiFePO_4$ (LFP)) encounter challenges to exceed energy densities of 300Wh kg^{-1}, which limit the further developing of LIBs [60]. Therefore, it is highly necessary to investigate high-capacity materials for catering to the need for high energy density LIBs. Conversion-based electrode materials with potentially higher energy densities than conventional intercalation-based electrode materials have drawn attention in recent years [61]. The conversion reaction can be expressed as:

$$MX_m + \mathrm{nLi} = \mathrm{nLi}X_{m/\mathrm{n}} + \mathrm{M} \qquad (1)$$

where M are transition metals and X represents F, Cl, O, S, P or N [62]. During the conversion reaction, the particles are generally reduced inside to a nanocomposite consisting of metal and $LiX_{m/n}$ nanoparticles. The reaction mechanism based on conversion reaction and intercalation reaction is shown in

Figure 1-6; in contrast to intercalation cathodes, conversion materials break and create new chemical bonds during insertion and extraction of Li.

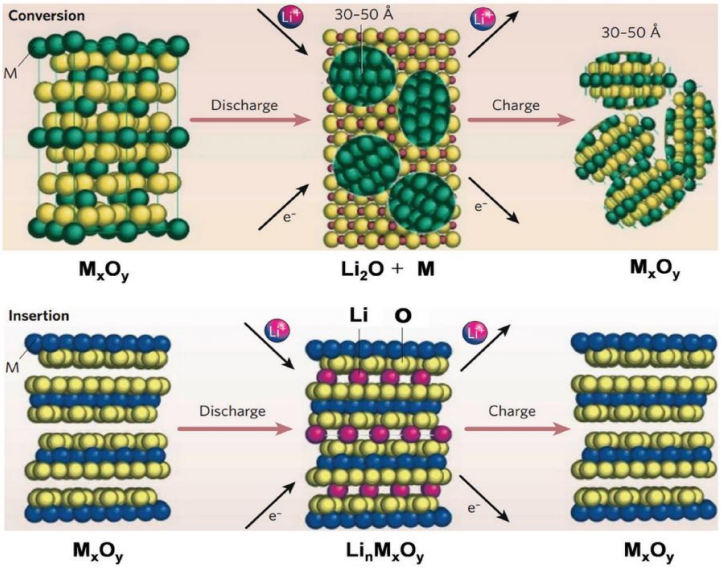

Figure 1-6: (a) Schematic of the reaction mechanism based on conversion reaction. (b) Schematic of the reaction mechanism based on intercalation/deintercalation reaction [63].

As shown in Figure 1-6, intercalation type electrode materials have their advantages in structural stability and fast and reversible Li-ion diffusion. Still, their capacity is limited by the crystal structure and the number of available vacancies that host Li ions. In contrast, conversion-type materials can achieve significantly larger capacities due to the advantage of multiple electron transfers per metal center in the conversion reaction, so these conversion materials could deliver capacity three to five times greater than conventional cathode materials, which could be possible to match the ultrahigh capacity anode [17]. The conversion process usually passes through several intermediate steps and phases during charge and discharge, as shown in Figure 1-7, where the conversion of FeF_2 is shown as an example. Generally, elements such as O, S, Fe, Cu, and other constituents of conversion materials are inexpensive and elementally abundant. Although halogens (which may be part of converted materials) are dangerous in their pure form, they usually become stable and environmentally benign as part of the salt for benign halogen salt [64].

Figure 1-8 and Figure 1-9 shows theoretical potentials and specific capacities of the main classes of conversion-type materials for cathode and anode. Among these conversion-type materials, metal fluorides are the most promising for the cathode due to their high theoretical discharge potential and gravimetric and volumetric capacities. At the same time, transition metal oxides are the most promising candidates as anode due to their lower discharge potential than sulfides and high gravimetric and volumetric capacities.

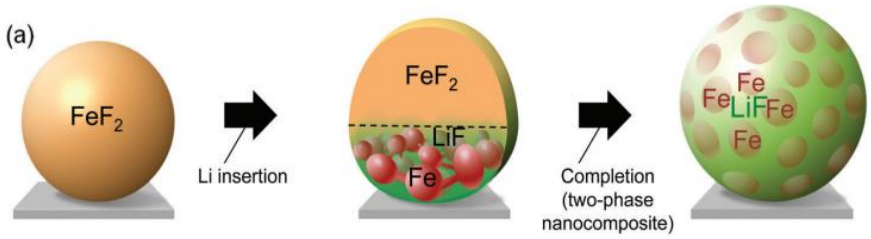

Figure 1-7: Typical conversion reaction mechanism selecting the lithiation of FeF_2 as an example [65].

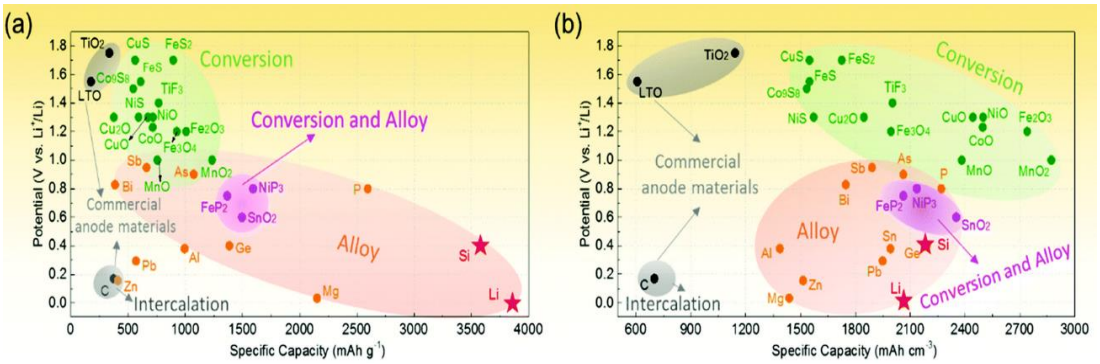

Figure 1-8: Approximate range of average discharge potentials, specific capacity and crystal structure of the selected most-common anode materials: (a and b) the theoretical gravimetric and volumetric capacities [66].

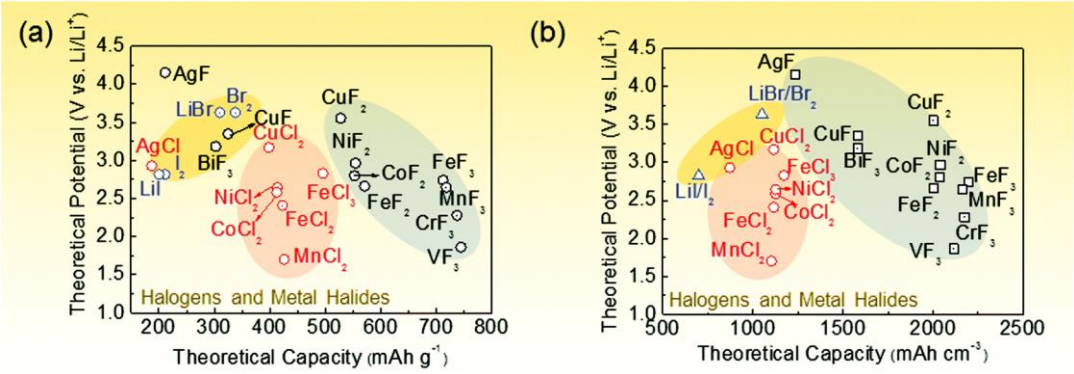

Figure 1-9: Theoretical specific capacity and operational voltage for typical conversion materials of selected transition metal halides, sulfides, and oxides [61].

Transition metal fluorides

Due to the highest electronegativity of F, conversion-type metal fluorides exhibit higher theoretical potentials than oxide, sulfide, nitrides, and phosphides, enabling them as alternatives for the positive electrode with noticeably higher specific capacity than intercalation-based candidates [67]. Among them, CuF_2 shows the highest theoretical potentials of 3.55 V vs.Li^+/Li and high gravimetric and volumetric capacities of 528 mAh g^{-1} and 2002 mAh cm^{-3}, making it an attractive. Iron-based FeF_2 and FeF_3 are also representative examples of metal fluorides for LiBs, whereas FeF_2 exhibits 571 mAh g^{-1} and 712 mAh g^{-1} for FeF_3 [68]. In general, metal fluoride (FeF_2) particles are transformed into nanocomposites consisting of metal nanoparticles distributed in a LiF matrix. Ideally, the metal (Fe) nanoparticles are interconnected to form an electron conduction network. However, the highly insulating nature of fluoride leads to inadequate material reactions. In addition, the volume change during conversion leads to contact between the electrode and the electrolyte, which results in irreversible decomposition and consumption of the electrolyte by the repeated generation of the SEI. Therefore, the cyclic performance of the material can be improved by increasing its electronic conductivity and suppressing the volume change of the material by reducing the particle size. For example, highly reactive carbon is compounded with metal fluorides by ball milling method, such as carbon-FeF_2 composites with high electrical conductivity and superior lithium storage properties [69], C/FeF_3 nanocomposites can reduce the length of ion diffusion paths while ensuring good electronic conductivity and interparticle contact [70]. The synthesis of nanoparticles smaller than 5 nm with rich active interfaces, that include many defects, leads to electronic and ionic activity. In addition, CoF_2 and NiF_2 are promising cathodes due to their higher capacities (~550 mAh g^{-1}) [71,72].

Transition metal oxides

Transition metal oxides (TMOs) have attracted the most attention due to their ease in preparation and high capacities putting them at the forefront as a class of conversion type anode materials. TMO-based anodes have higher operating voltages than graphite-based anodes and are safer since lithium metal does not separate easily on the TMO surface. So far, iron oxides (FeO, Fe_2O_3, and Fe_3O_4), cobalt oxides (CoO and Co_3O_4), and copper oxides (Cu_2O and CuO), as well as mixed TMOs, such as $NiCo_2O_4$ and $MnCo_2O_4$, have also been investigated as anode materials in LIBs. For example, Fe_2O_3 and Fe_3O_4 possess a high theoretical specific capacity of 1007 mAh g^{-1} and 926 mAh g^{-1}, respectively, and they also have low toxicity and cost, making them an attractive candidate [73]. Generally, mixed TMOs combined with the synergetic effects of multiple metal species display better electrochemical performance and better electrical conductivity. For instance, $NiCo_2O_4$ shows higher electrical conductivity than nickel oxide and cobalt oxide [74]. However, the commercial application of conversion anode materials is still a long process due to high initial irreversible capacity, significant volume changes, poor cycling stability, and large voltage hysteresis. The addition of additional conductive materials to improve the reaction kinetics or modify the electrode structure often becomes an important strategy to improve their performance effectively. For example, insulating and reactive binders typically reduce the capacity and rate capability of the material because the binder reduces the electronic conductivity and blocks the diffusion path of Li^+ [75]. Therefore, the development of binder-free electrodes can improve electronic conductivity and enhance the performance of the cell.

1.3. Background of high entropy materials

Recently, a new class of materials, namely high entropy materials (HEMs) has gained increasing attention as an emerging field. HEMs offer a variety of elemental compositions resulting in synergies between the constituent elements that may lead to new or unexpected properties and the possibility for tailoring the functional properties. That means HEMs can have the potential to outperform the parent material systems. Following the concept, many HEMs, including different compounds, such as alloys, oxides, oxyfluorides, borides, carbides, nitrides, sulfides, and phosphides, have been prepared to explore unique properties in numerous potential applications, e.g., thermoelectrics [76], dielectrics [77], and Li-ion batteries. In 2015, Rost et al. gave account of the first high entropy oxide (HEO), demonstrating the entropy stabilization effect [78]. Notably, a HEO with promising and unexpected properties has been explored as a conversion type electrode material in LIBs. Sarkar et al. depicted that the configurational entropy is one of the critical factors for the cycling stability of the HEO anode ($(Co_{0.2}Cu_{0.2}Mg_{0.2}Ni_{0.2}Zn_{0.2})O$), probably due to the partial

reduction of cations. In contrast, other cations remain in the rock-salt structure and facilitate the reintegration into the parent structure after conversion [79]. Ersu Lökçü et al. indicated that the electrochemical performance of HEOs would significantly improve by increasing the lithium cation concentration in the form of $(MgCoNiZn)_{1-x}Li_xO$ (x= 0.05, 0.15, 0.25, and 0.35), thereby oxidizing Co^{2+} and generating more oxygen vacancies [80].

These reports and many more demonstrate the role of chemical disorder, i.e., mixed cations and created vacancies, for cycling stability and tailoring ability. Considering the potential of HEMs for LIBs, it is of great interest to explore HEMs that can be utilized as cathodes for LIBs.

1.3.1. Definition of high entropy materials

The general high-entropy concept was first introduced by Yeh et al. [81] and Cantor et al. [82] in 2004 independently, incorporating multi composition with five or more equimolar elements into a single-phase solid solution alloy, in which atoms with different sizes are homogeneously distributed in an ideal situation. Yeh et al. proposed the definition of high entropy materials by composition based on the configurational entropy of mixing (ΔS_{conf} from Eqn (2)).

$$\Delta S_{conf} = -R ln x_i \qquad (2)$$

where R and x_i are the ideal gas constant and the molar fraction of each component *i*. The highest configurational entropy is calculated for an equimolar composition and the ΔS_{conf} is then dependent solely on the number of elements n:

$$\Delta S_{conf} = -R \sum \frac{1}{n} ln \frac{1}{n} = R \ln n \qquad (3)$$

Later, [83] et al. synthesized compounds, $Mg_{0.2}Co_{0.2}Ni_{0.2}Cu_{0.2}Zn_{0.2}O$, with a solid solution rock salt structure formed by five metal oxides. The entropy for single-phase stability due to the temperature dependence of its stability was demonstrated, with reversible solid-state transitions between the multiphase and single-phase (high-temperature) states and the entropy stabilization concept was first transferred to a multicomponent oxide. In this system, oxygen occupies anion sublattice, and five metal cations are incorporated into a single cation sublattice. Similar to multi-element alloys, for a given number of constituents (n), the configurational entropy of the multi-element oxide can be obtained from Eq 4.

$$\Delta S_{\text{conf}} = -R[\sum_{\text{i=1}}^{\text{n}} x_{\text{i}} \ln x_{\text{i}}]_{\text{cation-site}} + \sum_{\text{j=1}}^{\text{m}} x_{\text{j}} \ln x_{\text{j}}]_{\text{anion-site}} \qquad (4)$$

where R, n/m and x_i are the ideal gas constant, the number of components, and the atomic fraction of component, respectively. More components, with larger n, would result in higher ΔS_{conf}. Generally, configurational entropy can be classified into three categories according the value, high entropy is defined as ΔS_{conf} greater than 1.5R; medium entropy alloy (MEA) is between 1 and 1.5R; and low entropy alloy is less than 1R.

1.3.2. Four core effects of HEAs

After years of research, four unique core effects in HEAs were summarized by Yeh [84]: high entropy effect, sluggish diffusion effect, lattice distortion effect, and cocktail effect. These effects are closely related to HEAs' phase stability, microstructures, and mechanical properties, playing a significant role in instigating and directing a great deal of HEA research. Providing numerous versatile properties and hence making them suitable for many applications.

High-entropy effect

Generally, the entropy effect for HEAs refers mainly to configurational entropy; i.e., the high entropy produced by multiple principal elements can inhibit the generation of the intermetallic phase and promote the formation of a solid solution with a single phase structure [85].

According to Gibbs free energy formula:

$$\Delta G_{mix} = \Delta H_{mix} - T\Delta S_{mix} \qquad (5)$$

Where G is the Gibbs free energy, H is enthalpy, T is temperature, and S is entropy. In general, the higher mixing entropy (ΔS_{mix}) in a minimum of five equimolar elements system will overcome the enthalpy (ΔH_{mix}) contribution of formation of intermetallic compounds, reducing the free energy (ΔG_{mix}) of the formation of solid solution phase and facilitating their formation, particularly at higher temperatures. However, if the formation enthalpy of an intermetallic compound is high enough to overcome the effect of entropy, the intermetallic compound will still exit at high temperatures [86].

Sluggish diffusion

Generally, sluggish diffusion effects are exhibited in HEAs due to the lattice's diversity of atomic bonding environments, leading to more difficult atomic diffusion through solid solutions of multi principal elements. This is widely used to explain exceptional elevated recrystallization

temperatures, impressive high-temperature structural stability, and the formation of nanostructures or amorphous phases [87].

Compared to traditional alloys, the neighboring atoms of each lattice site in HEAs are diverse. During the atom diffusion, the interaction with the surrounding atoms is constant in conventional alloys, whereas various activation energies are required for each lattice site in HEAs. When an atom jumps into a low-energy site, it becomes 'trapped,' and the chance to jump out of that site will be lower. In contrast, if the site is high-energy, the atom has a higher chance of hopping back to its original location [88]. Both the process can slow down the diffusion process. On the other hand, the diffusion rate of each element in the HEA is different. Some elements are less active than others, so these elements have less success in jumping to vacancies when competing with other elements, and phase transitions usually require coordinated diffusion of multiple elements. Although the activation energy of distribution varies significantly with the element, the activation energy of diffusion increases from low to high entropy [89]. The retarded diffusion theoretically inhibits the grain growth of HEAs and explains the formation of nanoscale precipitates. In addition, sluggish diffusion increases the strength and structural stability of HEA, especially at high temperatures [90].

Severe lattice distortion

HEAs contain many kinds of elements; lattices of HEAs can be severely strained due to different compositional atomic sizes and random positions. Larger atoms push away from their neighbors, while smaller atoms have extra space around them. The strain energy associated with lattice distortion raises the overall free energy of the HEA lattice. Usually, lattice strain, proportional to the dislocation parameter of the atomic size difference in the solid solution, increases the strength and hardness of the material; lattice distortion hinders dislocation migration and leads to significant solid solution strengthening, which reduces the X-ray diffraction intensity [91]. In addition, lattice distortion in HEAs leads to increased scattering of propagating electrons and phonons, which translates into reduced electrical and thermal conductivity and a reduction in the temperature dependence of these properties [92].

Cocktail effect

The cocktail effect is one of the most abstract of the HEA core effects, and it is difficult to determine precisely what it means and how it influences material properties. Ranganathan [93] first mentioned the cocktail effect for alloys to describe some essential characteristics of the elements that affect the properties of an alloy. For HEA, the cocktail effect does not mean that the properties

of an alloy are just a superposition of the properties of each component but rather an unpredictable result of a synergistic mixture that is greater than the sum of the parts. There are interactions between the different elements that ultimately lead to the compounding effect of the HEA and the average compounding properties. The final properties of this alloy are not equal to the sum of the properties of its components, and this synergism and unpredictability is the cornerstone of many eccentric and exciting materials.

1.4. High entropy materials for battery application

High entropy materials (HEMs), including high entropy alloys (HEAs), high entropy oxides (HEOs), and other high entropy compounds, have gained significant attention in the past few years. These materials with synergistic hybrid elements have unique structures and properties increasingly investigated for energy-related applications such as catalysis and energy storage. Recently, HEOs have been explored for use as electrode materials for lithium/sodium batteries, solid electrolytes, and lithium-sulfur batteries because of their properties such as high capacity, high electron conductivity, or high ionic conductivity.

1.4.1. High entropy oxides as ionic conductors

Following the pioneering study of HEOs, Bérardan et al. [94] investigated the electrochemical properties of HEOs. They found that they have excellent lithium ionic conductivity at room temperature, making them a new potential material for lithium conductors. It was found that the ionic conductivity of HEOs increased with increasing lithium doping content, reaching a maximum ionic conductivity at 30% lithium doping (10^{-3} S cm^{-1}), which is five orders of magnitude higher than that of the pristine HEOs (10^{-8} S cm^{-1}). This may be because the cations in (Mg, Cu, Ni, Co, Zn) O can be replaced by Li-ions through an intrinsic charge compensation mechanism or a combination of +1 and +3 elements, which are replaced by +1 elements while maintaining the rock-salt structure, may involve oxygen vacancies, opening possible diffusion pathways for lithium ions through the lattice, leading to an increase in conductivity. Later, Maciej Moździerz et al. [95] found that, in addition to ionic conductivity, the contribution of electronic conductivity also increases significantly with increasing lithium doping content. Therefore, the Li-doped HEOs should be classified as mixed ionic-electronic conductors rather than solid electrolytes. With the increase of the ionic composition, the electronic conductivity was determined to increase significantly with the addition of Li in the $(Co, Cu, Mg, Ni, Zn)_{1-x}Li_xO$ series. Nevertheless, these unexpected findings have stimulated many recent studies on the performance of high entropy materials in electrochemical energy storage devices.

1.4.2. High entropy materials as conversion type electrodes

In 2018, Sarkar et al. [96] investigated (CoCuMgNiZn)O as anode materials for LiBs, which mainly undergo a conversion reaction upon the charge and discharge process. The cells showed an outstanding long-term cycling performance, with a specific capacity of about 650 mAh g^{-1} and Coulombic efficiencies of >99.5% at 200 mA g^{-1} after 900 cycles without capacity fading. Unlike conventional conversion materials, some cations in the lattice are involved in the reaction and are reduced to the metal, while other cations with stable oxidation state are not involved and act as hosts to helps the reversibility of the redox-reaction. Additionally, by comparing the electrochemical properties of each medium-entropy oxide material with HEOs, they demonstrated that entropy stabilization has a very significant effect on the stabilization structure of electrode materials and their cyclic stability. Since then, the outstanding electrochemical properties of high-entropy materials have attracted attention, inspiring researchers to study and develop other types of high-entropy materials for battery electrodes. Chen et al. [97] studied the spinel HEO $(MgTiZnCuFe)_3O_4$ as an anode material in a half cell LIB. The cells delivered a specific capacity of 504 mAh g^{-1} at 100 mA g^{-1} after 300 cycles and an excellent 96.2% capacity retention at a high current density of 2000 mA g^{-1} after 800 cycles. This electrode material's excellent electrochemical performance and stability are attributed to the fast reaction kinetics, capacitive behavior, and structural equilibrium of the high-entropy oxide. Besides, Ling et al. [98] found that high-entropy sulfides have better performance as electrode materials than binary CoS_2 due to the favorable influence of the cocktail effect of high entropy compounds. Yan et al. [99] synthesized perovskite-type $[(NaBi)_{0.2}(LiLa)_{0.2}(CeK)_{0.2}Ca_{0.2}Sr_{0.2}]TiO_3$ and studied the material as an anode for LIBs, and found that the stability of the cell cycle can be attributed to the charge compensation mechanism and the unique entropic stabilization of the structure.

1.4.3. High entropy materials as insertion type electrodes

Most of the reported studies on HEOs are based on multi-cation systems with only oxygen in the anion sites. The total stabilizing configurational entropy of the material comes from the cations. Wang et al. [100] reported a multi-anionic and multi-cationic system where cations and anions contribute to the total S_{config}, resulting in a higher stabilizing entropy. In this system, Li(HEO)F with a rock salt structure is formed by mixing LiF and HEO and is used as a cathode for LIBs. Typically, Li(HEO)F can deliver a discharge capacity of 120 mAh g^{-1} at 0.1 C with a middle discharge voltage of 3.4 V vs. Li^+/Li and no significant voltage plateau upon charging/discharging, indicating an insertion type reaction for Li(HEO)F. Furthermore, they compared Li(HEO)F with the rock-salt low-entropy, single-metal LiNiOF. Surprisingly, Li(HEO)F presented a more stable cycling

performance and higher capacity even though it had more inactive TM in the structure. Entropy stabilization is essential for maintaining the rock-salt material active upon cycling. Zhao et al. [101] applied the concept of high entropy to design a high entropy oxide $NaNi_{0.12}Cu_{0.12}Mg_{0.12}Fe_{0.15}Co_{0.15}Mn_{0.1}Ti_{0.1}Sn_{0.}1Sb_{0.04}O_2$ containing nine components as a Na ion layered cathode. The material exhibited long-time cycle stability and excellent capacity retention of 83% after 500 cycles at 3C. In addition, the material structure exhibited reversible phase change between O3 and P3 phases during the cycling process. It was found that more than 60% of the total capacity was stored in the O3-type region than other O3-type Na-ion cathodes. The presence of multiple transition metal components in the layered HEO during Na+ (de)intercalation, which retain its structure during cycling, was suggested as a possible mechanism for this reversible phase transition and the long cycle life of the cathode material. Ceder et al. [102] has recently applied the high entropy concept to prepare cation-disordered rock salt (DRX) cathodes. As expected, the long-standing SRO challenge has been greatly suppressed by the systematic decrease in short-range order and the systematic increase in energy density and rate capability due to the increase in TM species in the high-entropy DRX cathode. Compared with $Li_{1.3}Mn_{0.43}Ti_{0.3}O_{1.7}F_{0.3}$ and $Li_{1.3}Mn_{0.22}Mn_{0.23}Ti_{0.1}Nb_{0.2}O_{1.7}F_{0.3}$, $Li_{1.3}Mn_{0.12}Co_{0.12}Mn_{0.13}Cr_{0.13}Ti_{0.1}Nb_{0.2}O_{1.7}F_{0.3}$ has the highest specific capacity at low rates (20 mA g^{-1}) reaching 307 mAh g^{-1} (955 Wh kg^{-1}) and remaining over 170 mAh g^{-1} when cycled at a high rate of 2,000 mA g^{-1}. Later, A series of layered cathode HEOs, $Li(CoNiAlMnZn)O_2$, $Li(CoNiAlMnFe)O_2$, and $Li_{0.8}Na_{0.2}(CoNiAlMnFe)O_2$, demonstrating Li^+ reversible intercalation/extraction from Li-HEO, were reported by Wang et al. [103] However, the material capacity is relatively low, and the capacity decays rapidly which may be caused by cation disorder. Interestingly, $Li_{0.8}Na_{0.2}(CoNiAlMnFe)O_2$ shows a much improved electrochemical performance of the lithium (de)intercalation layer after adding a small amount of sodium, which may be due to the enlarged diffusion channel of the layered structure.

1.5. Experimental methods

1.5.1. Scanning electron microscopy

Scanning electron microscopy (SEM) is a technique that obtains the morphology information and composition of a sample by scanning the surface with a focused, high-energy beam of electrons. In a typical SEM, an electron beam is thermionically emitted from an electron gun of thermionic emission mode (tungsten or LaB_6), field emission mode (cold-cathode type (single tungsten crystal), or thermally assisted Schottky type (zirconium oxide)) [107]. As the electrons interact with the sample, they produce secondary electrons (SE), backscattered electrons (BSE), and

characteristic X-ray radiation (CR). Normally, SEs can collect images of the sample surface with a high resolution of below 1 nm since that secondary electron is emitted very close to the specimen surface. Back-scattered electrons (BSE) are beam electrons reflected from deeper specimen locations. Consequently, the resolution of BSE images is less than SE images. BSE is often used in analytical SEM, along with the spectra made from the characteristic X-rays, because the intensity of the BSE signal is strongly related to the specimen's atomic number (Z). Characteristic X-rays are emitted when the electron beam removes an inner shell electron from the sample, causing a higher-energy electron to fill the shell and release energy. The energy or wavelength of these characteristic X-rays can be measured by Energy-dispersive X-ray spectroscopy or Wavelength-dispersive X-ray spectroscopy and used to identify and measure the abundance of elements in the sample and map their distribution. For standard imaging in SEM, specimens must be electronically conductive to prevent electrostatic charge accumulation, avoiding scanning faults and other image artifacts. Non-conductive materials are usually coated with an ultrathin layer of gold or graphite by sputter coating or thermal evaporation.

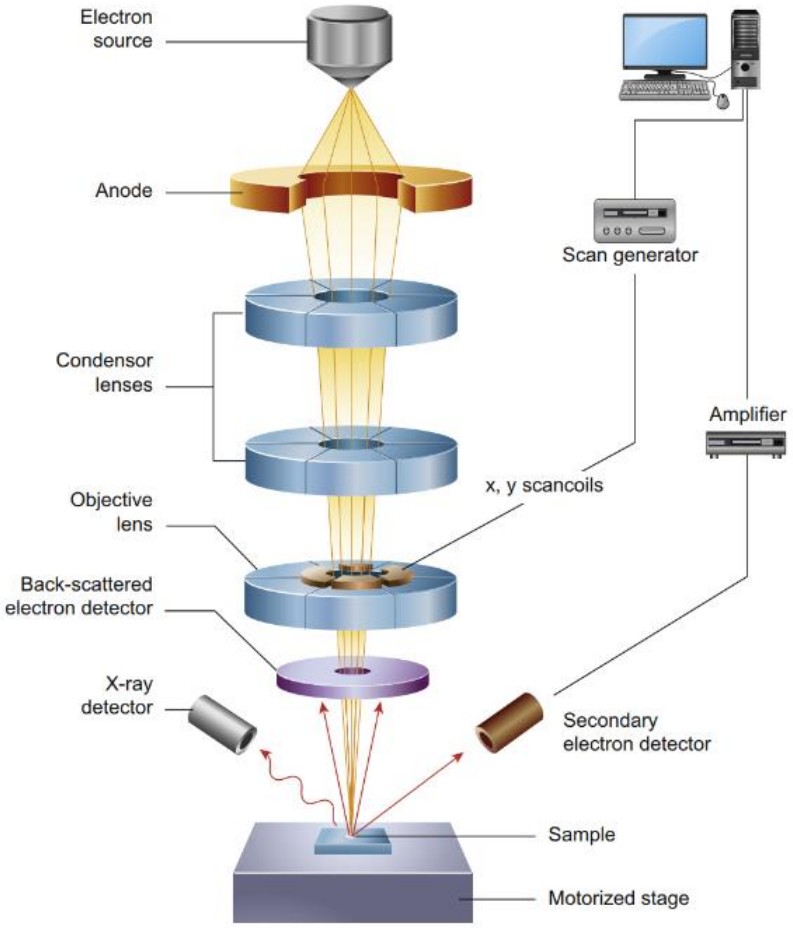

Figure 1-10: Schematic diagram of the core components of an SEM microscope [108].

1.5.2 Transmission electron microscopy

Transmission electron microscopy is performed by irradiating a beam of high-energy electrons transmitted through a fragile sample, typically less than 100 nm thick. An image is formed from the interaction between electrons and atoms, which can be used to observe the crystal structure and features in the structure for chemical analysis. Because the wavelength of electrons is much smaller than that of light, the best resolution achievable with TEM images is many orders of magnitude better than that of light microscopy. As a result, TEM can reveal structures down to the atomic level. TEM instruments have multiple operating modes, including conventional imaging and diffraction.

In imaging mode, the beam of electrons from the electron gun is focused into a small, thin, coherent beam using the condenser lens. This beam is restricted by the condenser aperture, which excludes high-angle electrons. The beam then strikes the specimen, and parts of it are transmitted depending upon the thickness and electron transparency of the sample. The objective lens focuses this transmitted portion into an image on a phosphor screen or charge-coupled device (CCD) camera. As the electrons pass through the sample in diffraction mode, they are scattered by the electrostatic potential set up by the constituent elements in the specimen. After passing through the specimen, they pass through the electromagnetic objective lens, which focuses all the electrons scattered from one point of the specimen into one point in the image plane.

The intensity of the intermediate lens is not the same in both cases, i.e., the current added is not the same. In the diffraction mode, the medium lens reunites the electron beam passing through the selected diffraction diaphragm into a diffraction spot on the object plane of the projector lens, which is then projected onto the phosphor screen by the projector lens. In the normal imaging mode, the intermediate lens forms the image of the sample on the object plane of the projection lens. In contrast, the diffracted image is still higher up, so that finally only the sample image is projected onto the phosphor screen. In addition, electron energy loss spectroscopy (EELS) can be used to detect the elemental composition and valence state of a sample by selecting electrons with a specific velocity to identify the elements [109].

1.5.3. X-ray diffraction

X-ray diffraction (XRD) is used to determine, e.g., the crystal structure, the materials' phase purity and lattice parameters. For non-crystalline materials, the XRD patterns are some diffusely scattered reflections because their structures are not long-range ordered with the atomic arrangement in the crystalline layout, but only short-range ordering in the range of a few atoms.

However, the atomic ordering is long-range in three-dimensional space for crystalline materials, and their XRD diffraction patterns show enhanced peaks at specific positions. Generally, the characteristics of a diffraction pattern can be considered to consist of two aspects: a) the position of the diffraction lines - determined by the size, crystal structure, and orientation of the cell; b) the intensity of the diffraction beam - depending on the type of atoms and their position in the cell [110]. A qualitative and quantitative relationship between X-ray diffraction and crystal structure can be established by identifying the location and intensity of the diffraction pattern in space.

(1) The Bragg equation can reveal the intrinsic relationship between diffraction and crystal structure. When X-rays are irradiated into a crystal, the optical range difference nλ between X-rays irradiated to two adjacent crystal faces is 2dsinθ. Suppose the visual range difference is equal to n times the wavelength of X-rays. In that case, In that case, X-rays undergo constructive interference and strengthen each other, and vice versa; the diffraction intensity will remain the same or weaken elsewhere.

$$n\lambda = 2dsin\theta \qquad (6)$$

(n=1, 2, 3.....), where λ, d, and θ represent the wavelength of X-rays, the crystal plane spacing, and the angle between the incident X-rays and the corresponding crystal plane, respectively. Therefore, by using the Bragg equation, one can use X-rays of known wavelength to solve for the crystal face spacing d to obtain crystal structure information, which is structural analysis; one can also use a crystal with known crystal face spacing to measure the wavelength of unknown X-rays, which is X-ray spectroscopy.

(2) Scherrer's formula is the theoretical basis for measuring crystallite size by XRD. It mainly describes the relationship between crystallite size and diffraction peak half-peak width.

$$D = K\lambda/Bcos\theta \qquad (7)$$

where D, K, λ, B, θ are the average thickness of the grain perpendicular to the crystallite size, Scherrer's constant, X-ray wavelength, half-height width (radian) of the diffraction peak of the measured sample, and diffraction angle, respectively.

1.5.4 X-ray photoelectron spectroscopy

X-ray Photoelectron Spectroscopy (XPS), by using an electron spectrometer to measure the photoelectron and auger electron energy distribution emitted from the sample surface during X-ray photon irradiation, collects the electron energy and angle of excitation from the material

surface to analyze the elements on the sample surface (0~10 nm depth) by comparing the electron energies of the different shell layers with those of known elements. In XPS measurements, photoelectrons are excited from the inner shell of an atom when a constant frequency beam of X-rays irradiates the specimen. After measuring both the kinetic energy and the number of escaping electrons, the binding energy of the element can be obtained according to the work of Ernest Rutherford.

$$E_{binding} = E_{photon} - (E_{kinetic} + \varphi) \qquad (8)$$

where Binding is the binding energy of the electron (BE), E_{photon} is the energy of the incident x-ray photon, $E_{kinetic}$ is the kinetic energy of the measured electron, and φ is the work function. XPS commonly uses Al Kα or Mg Kα X-rays as the excitation source, which can detect all elements in the periodic table except hydrogen and helium, with a general detection limit of 0.1%.

1.5.5. Cyclic voltammetry

Cyclic voltammetry is a method to measure the change of electrode reaction current with time by changing the potential applied to the working electrode at a specific rate. By controlling the electrode potential at different speeds and repeatedly scanning the electrode with a triangular waveform over time, the redox reaction occurs on the active material at the working electrode. The magnitude of the electrochemical response current at the electrode is obtained so that the reversibility of the electrode reaction, the possibility of intermediate, phase boundary adsorption or new phase formation, and the nature of the coupled chemical reaction can be judged according to the shape of the curve. As shown in Figure 1- 11, The data for cyclic voltammograms can be reported as US or IUPAC convention. The difference between these conventions is that the data is 180 degrees rotated. The arrow shows the beginning of the first segment [111].

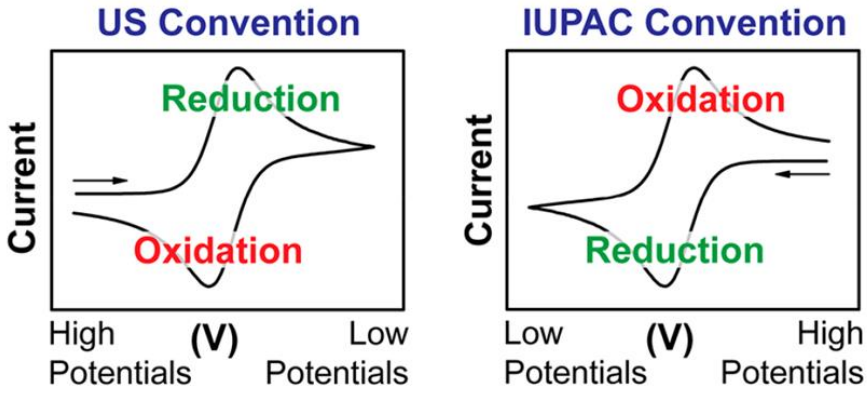

Figure 1- 11: US and IUPAC Conventions for cyclic voltammograms.

1.5.6. Electrochemical impedance spectroscopy

Electrochemical impedance spectroscopy is an essential electrochemical test method with a wide range of applications in electrochemistry, especially in the field of lithium-ion batteries, such as electrical conductivity, apparent chemical diffusion coefficient, the evolution of SEI growth, dynamic measurement of charge transfer, and material phase transition processes. EIS records the impedance of electrochemical cells at different response frequencies, which generally covers a wide frequency range (μHz-MHz), and therefore can be used to analyze the impedance of electrochemical cells with different response time constants. The EIS data are usually expressed as Nyquist plots (real versus imaginary impedance) or Bode plots for frequency dependence. As shown in Figure 1- 12 [112], the EIS spectrum could be divided into three regions: Ohmic region (frequency higher than 1000 Hz): it represents the internal resistance of the cell measured where the cell impedance switch from an inductive to capacitive behavior. The mid-frequency region (frequency interval between 1000 Hz and 0.1 Hz) represents the charge-transfer processes, both from the electrolyte to the surface of the electrode and from the electrode surface into the bulk active material of the electrodes. The Low-frequency region (frequency lower than 0.1 Hz) represents the diffusion processes at the two electrodes.

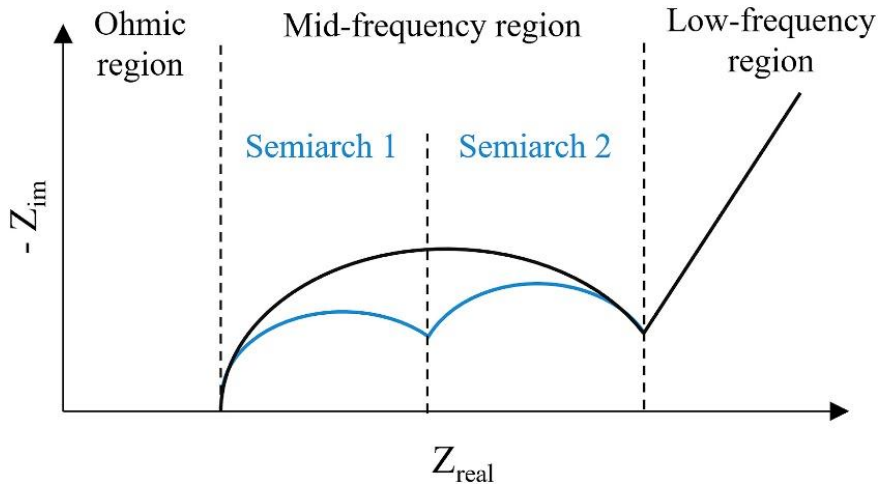

Figure 1- 12: Representation of the frequency regions on a Nyquist plot [112]. The typical EIS spectrum of a Li-ion cell could be composed of a unique semiarch or two semiarches in the Mid-frequency region.

1.5.7. Photonic curing

Photonic curing is a heat treatment in which high-energy photons are directed at the film to achieve the high temperatures required to cure the oxide film. Photonic curing is an ultra-fast, instantaneous process that typically takes from a few minutes to a few milliseconds to give an oxide layer morphology and properties comparable to most thermal curing processes (drying,

sintering, reacting, annealing, etc.). Photonic curing relies primarily on radiant heat transfer from the lamp to the object of interest when the flash is on, usually between 100 μs and 100 ms. Typically, the instrument consists of capacitors charged to a high potential to release a high-energy pulse through the xenon lamp. This allows the lamp to illuminate the sample with a high-energy light in the spectral range of 200-1100 nm. A short processing time facilitates immediate curing at a rate of approximately 1.6 ms^{-1} [104].After the radiant heat impinges on the object, heat transfer through the sample and convective losses in contact with the material will occur until the object approaches thermal equilibrium. Since the process is based on surface heating caused by photon absorption, it is safe to form oxide films on inexpensive and flexible substrates, such as PET/PEN or even paper [105] . In this work, the Novacentrix PulseForge 1200 was used for photonic curing. Exposure levels ranged from 0.01 J cm^{-2} to 20 J cm^{-2}, and the broadcast nature of the light source allowed the uniform curing of areas as large as 112 cm^{-2} in a single flash.

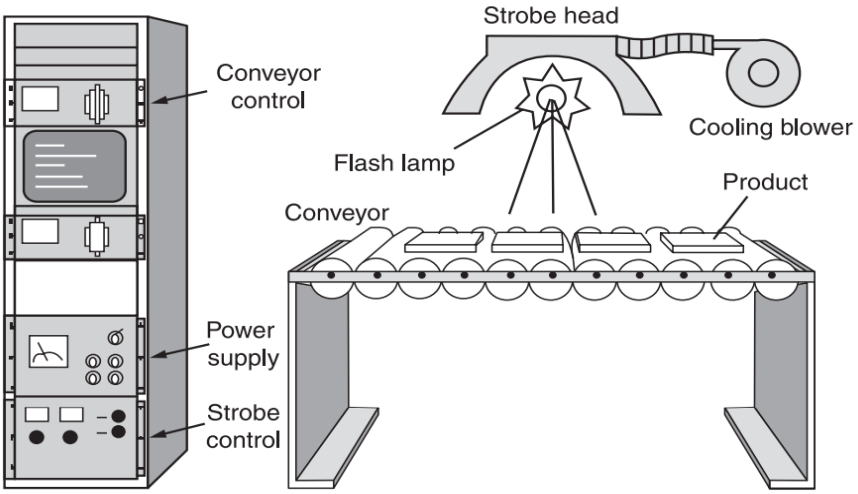

Figure 1-13: Schematic of the photonic curing lamp sintering depositions on a conveyor [106]

Chapter 2

2. Ultra-fast photonic curing synthesis of high entropy oxide as binder-free electrodes for lithium batteries

2.1. Introduction

In recent years, a large number of studies have been reported the unique physical properties and potential applications of transition metal-based HEOs (TM-HEO), rare-earth-based HEOs (RE-HEO), and hybrid HEOs with single-phase rock salt, fluorite, or perovskite structures (TM-RE-HEO) [113,114]. The fabrication of HEO powders is first reported by Rost et al.[83], (Mg, Cu, Ni, Co, Zn)O was synthesized through solid-state reaction by ball milling MgO, NiO, CuO, CoO, and ZnO for 2 h with a subsequent heat treatment in air at 1000 ^{o}C for 12 h, consuming a tremendous amount of energy, which is their main drawback. Therefore, in order to successfully prepare HEOs with different compositions and crystal structures, wet chemical methods with lower energy requirements such as co-precipitation [115], solvothermal [116], hydrothermal [115], spray pyrolysis [117], and mechanochemical methods [118] have been reported. However, the synthesized powder must be annealed at a temperature greater than 850 °C or ball milling for long time to form a phase-pure solid solution. In addition, spark plasma sintering methods (SPS) [119] is reported for the fabrication of HEOs in a short time. However, this method requires specialized equipment for regulating the applied pressure, temperature, and electric field during the sintering process.

Based on the above discussion, the ultra-fast photocurable synthesis method was applied to prepare two high-entropy oxides, (MgCoNiCuZn)O in the rock salt structure and $(CoCrFeMnNi)_3O_4$ in the spinel structure. The technique was also applied for the preparation of a binder-free electrode material by compounding with steel mesh, which can be potentially produced roll to roll by a very fast synthesis method and is expected to be used in the large-scale preparation and application of flexible electrode materials.

2.2. Materials synthesis and cell fabrication

Preparation of (MgCoNiCuZn)O

Nitrate salts of the respective metals $Co(NO_3)_2 \cdot 6H_2O$, $Ni(NO_3)_2 \cdot 6H_2O$, $Mn(NO_3)_2 \cdot 4H_2O$, $Cr(NO_3)_2 \cdot 6H_2O$, $Fe(NO_3)_3 \cdot 9H_2O$; from Sigma-Aldrich were dissolved in 1 mL of ethanol to form a 1 M solution. 20 µl solution was dispersed on a 2*2 cm silicon wafer, evaporated at 60 °C, and put for the photonic curing at 3 kV for 75 s, at a distance to the lamp of 1 cm and irradiated for 1-3 times.

Electrodes preparation

The prepared solution was added with 20% ethylene glycol; then steel mesh was immersed into the solution by the dip-coating method at withdrawal rates of 5 mm/s. The steel mesh was then dried at 60 °C and irradiated for 3 times on both sides.

2.3. Results and discussion

2.3.1. Structural characterization

Herein, we report the ultra-fast synthesis of high entropy oxides with different structures by a photonic curing approach at room temperature. The rock salt-type high-entropy oxides (MgCoNiCuZn)O, $Li_{0.33}(MgCoNiCuZn)_{0.67}O$ and spinel-type high-entropy oxides $(CoCrFeMnNi)_3O_4$ are labeled as R-HEO, R-LiHEO, and S-HEO, respectively. X-ray diffraction measurements were used to determine the crystal structure and phase purity after synthesis. Figure 2- 1 compares the X-ray diffraction patterns of the materials synthesized at different irradiation times. R-HEO (Figure 2- 1a) starts to show the phase of the rock salt-type structure after 75 s of light irradiation. Still, a small amount of heterogeneous phase is present, with two peaks of the heterogeneous phase at 25° and 27.5°, which, by comparison, is the structure of ZnO [120]. With the light irradiation, when the irradiation time reached 225 s, the peak of the heterogeneous phase completely disappeared, and the rock salt-type material with a single-phase was obtained. However, the single-phase spinel structure of S-HEO was obtained at 75 s of irradiation, which may be because the formation of spinel-structured HEO requires lower energy compared to rock salt-type HEO. No significant structural changes in the spinel structure occurred with irradiation. Refinement of XRD revealed that the cell parameters of R-HEO (Figure 2- 2a-c) were about 4.24 Å, S-HEO (Figure 2- 2e-f) were about 8.34 Å, and the cell parameters of the two structures did not

change significantly with light exposure time, which indicates that the rock salt and spinel structures can be formed in a short time by photonic curing.

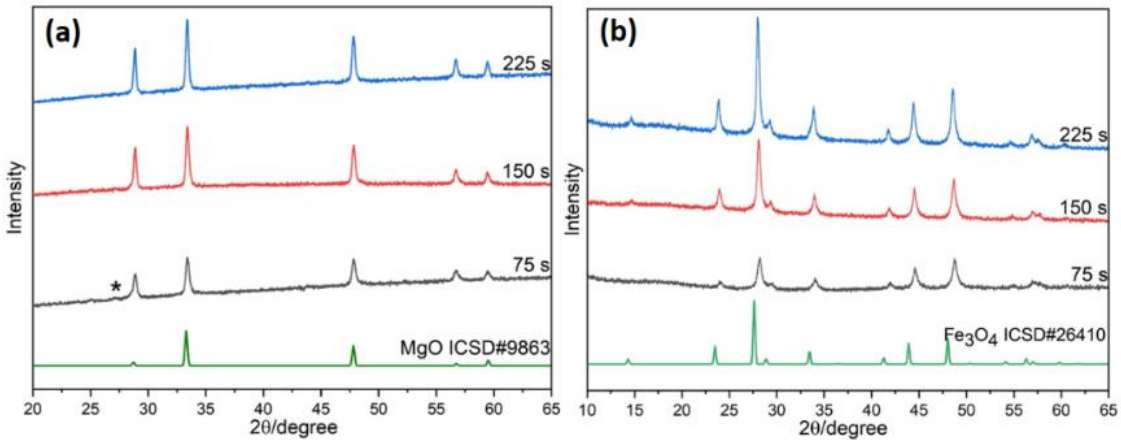

Figure 2- 1: XRD (Ga K-alpha irradiation) of R-HEO (a) and S-HEO (b) synthesized by different irradiation times.

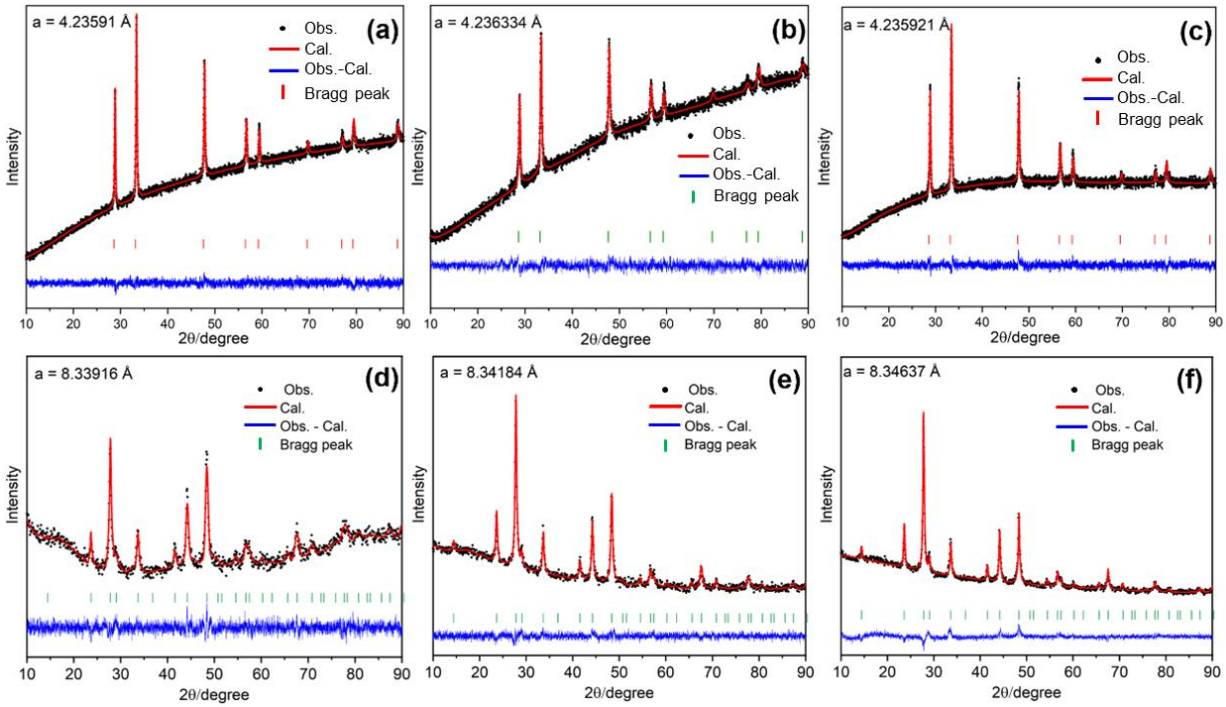

Figure 2- 2: Rietveld refinement of XRD patterns of R-HEO (a-c) and S-HEO (d-f)

However, in the case of R-LiHEO (Figure 2- 3), the phase of ZnO is still persistent after 225 s of irradiation, indicating that more energy is required for the synthesis of the pure phase of R-LiHEO, presumably for the incorporation of the additional element Li on a TM-site. With the extension of the irradiation time, it is observed that the rock salt structure of the pure phase has been formed after 550 s of irradiation.

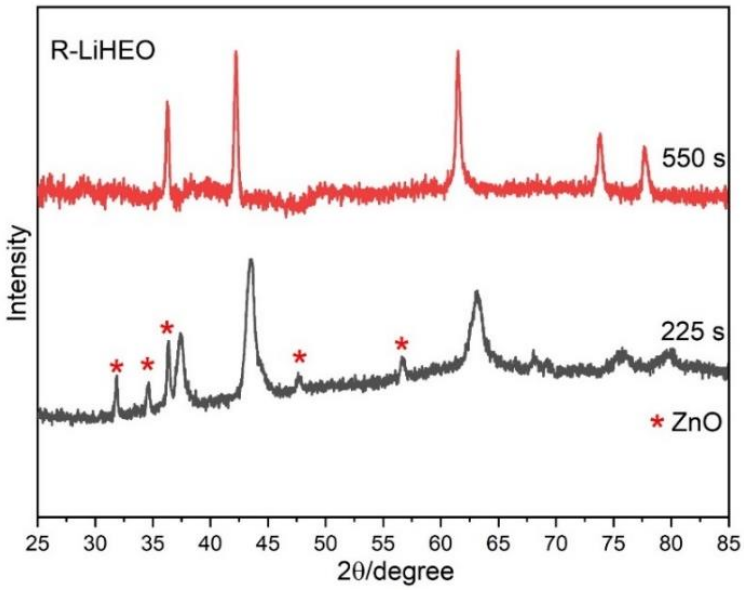

Figure 2- 3: XRD (Cu K-alpha irradiation) of R-LiHEO synthesized by different irradiation times

TEM analysis was performed to further investigate the structural details of the material. Figure 2-4 shows the high-resolution TEM (HR-TEM) micrograph of R-HEO. As shown, the morphology of R-HEO can be described as polycrystalline particles with sizes of 10 to 100 nm. Figure 2- 4c show the diffraction plane of R-HEO with a lattice spacing of 0.30 nm, and the area refers to the (002) lattice plane of the rock salt structure of R-HEO [79]. Figure 2- 5 shows a HR-TEM micrograph of S-HEO. As shown, the morphology of S-HEO can be described as polycrystalline particles with sizes of tens to hundreds of nanometers. Figure 2- 5c shows the diffraction plane of S-HEO with a lattice spacing of 0.48 nm, and the area refers to the (111) lattice plane of the spinel structure of S-HEO [121]. Both samples have low density with obvious porosity. However, the S-HEO sample is much denser compared to R-HEO. For R-HEO and S-HEO, the diffraction rings are consistent with the XRD measurements and agree with $Fm\bar{3}m$ and $Fd\bar{3}m$ space group, respectively. Figure 2- 6 showing the SAED extracted from LiHEO. Next to the (022) diffraction ring of the main phase of the rock salt, some diffraction points corresponding to a 0.19 nm d-spacing appear, most likely corresponding to some polycationic ZnO crystals or unreacted precursors. Figures 2- 4e and 2- 5e show the elemental distribution of R-HEO and S-HEO, as indicated by STEM-EDX elemental mapping. All elements are uniformly distributed on the nanoscale with no apparent accumulation or segregation.

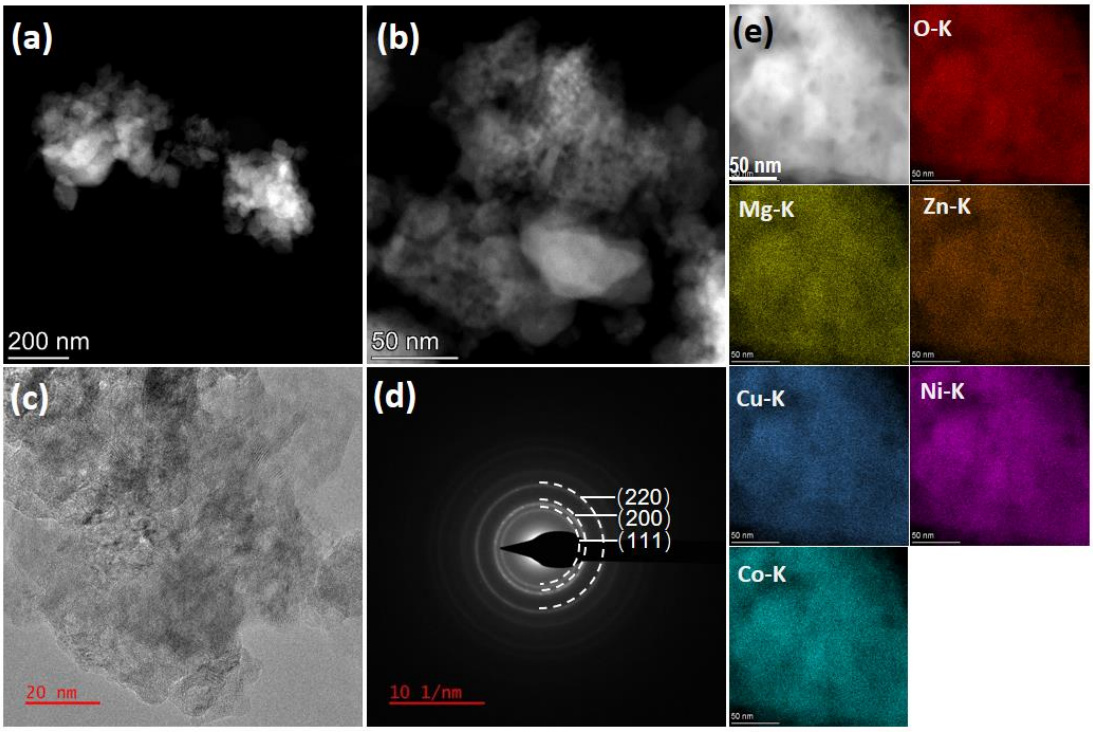

Figure 2- 4: HR-TEM of R-HEO. (a), (b) TEM image of R-HEO with different magnifications; (c) the lattice of R-HEO and (d) SAED pattern (The planes corresponding to the rings are illustrated in the figures); (e) STEM-EDX mapping of R-HEO. All constituent elements show a uniform distribution.

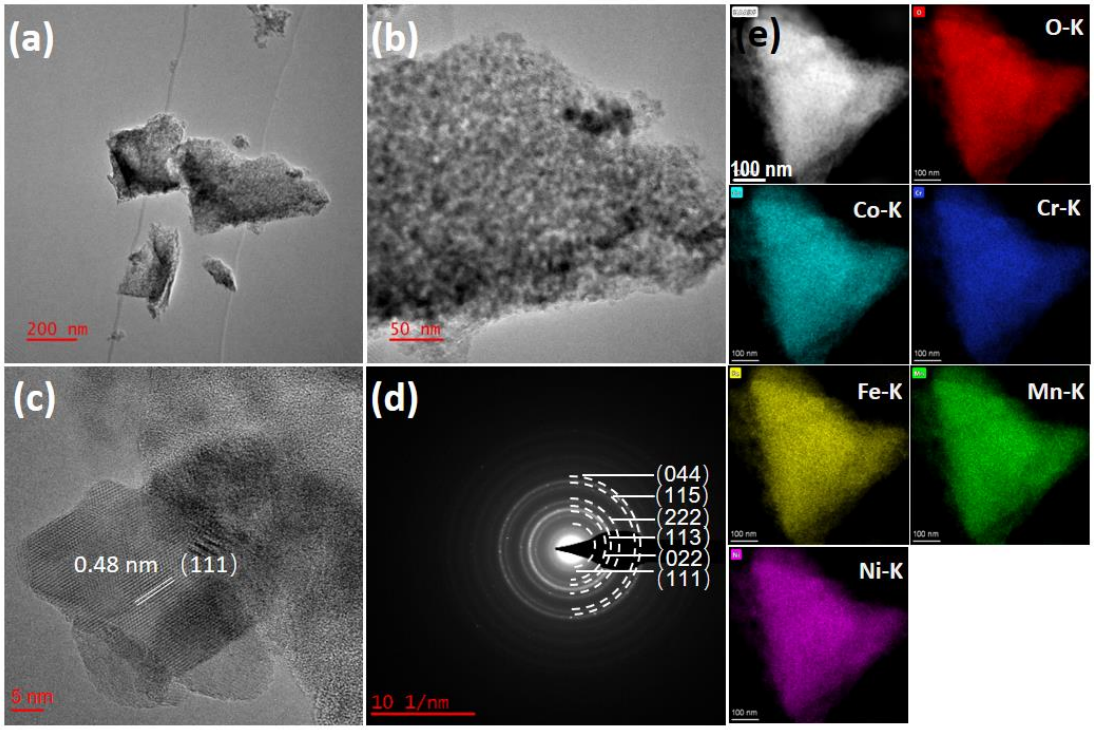

Figure 2- 5: HR-TEM of S-HEO. (a), (b) TEM image of S-HEO with different magnifications; (c) the lattice of S-HEO and (d) SAED pattern (The planes corresponding to the rings are illustrated in the figures); (e) STEM-EDX mapping of HEO. All constituent elements show a uniform distribution.

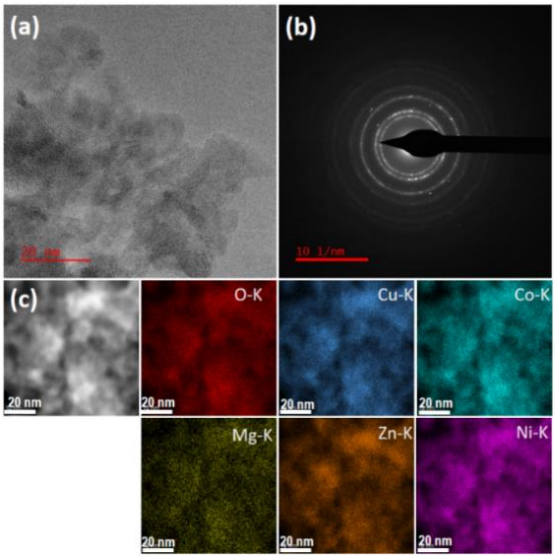

Figure 2- 6: HR-TEM of R-LiHEO. (a), (b) TEM image of R-LiHEO with different magnifications; (c) STEM-EDX mapping of R-LiHEO. All constituent elements show a uniform distribution.

Figure 2- 7 shows the SEM images of R-HEO (a-c) and S-HEO (d-f) and the corresponding EDX, from which we can see that the R-HEO and S-HEO materials are covering the surface of the stainless-steel mesh, forming a uniform coating layer. However, there are still some small cracks present in the coating layer, and since the conversion material would have undergone volume changes during cycling, the cracks may accelerate causing the electrode material to fall off from the mesh during cycling. As can be seen from the EDX, the elements are uniformly distributed in the material without any obvious segregation, and the XRD test of the scraped powder proves the formation of a single-phase. Hence, the coating layer is uniform and stable on the surface of the steel mesh.

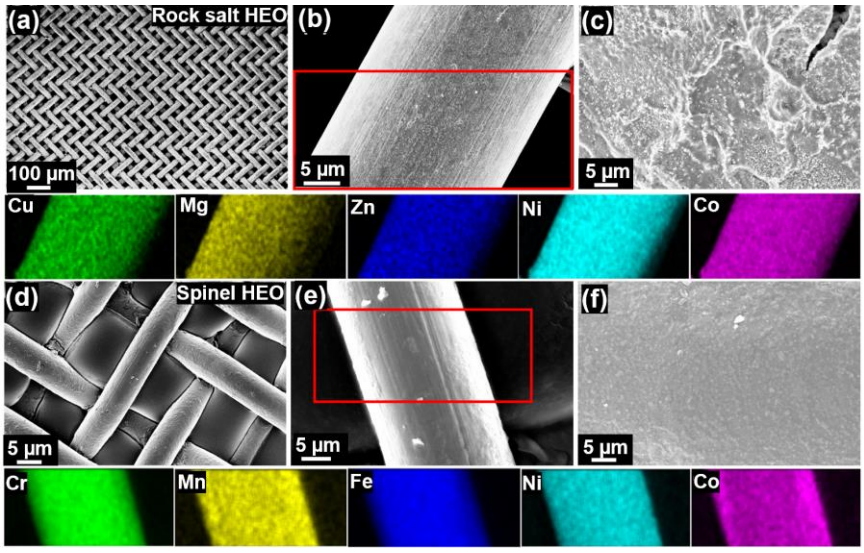

Figure 2- 7: Typical SEM of electrode with the decorated steel mesh of R-HEO (a-c) and S-HEO (d-f) and their EDX mappings of selected areas below the (b) and (e), respectively.

2.3.2. Electrochemical properties

Figure 2- 8 and 2- 9 show the cycling performance of R-HEO and S-HEO, respectively. The electrode materials exhibit high capacity at low C-rates. The capacity decays with increasing current density but reverts to 600 mAh/g when the current density returns to 0.5 A/g, which is consistent with the data reported for conventional electrode preparation methods. However, in the long term cycling in Figure 2- 8c, it can be seen that the cell capacity decays within the first ten cycles. However, light increase in capacity occurs between 10 and 40 cycles, which shows a relatively high capacity due to irreversible reactions resulting from the formation of SEI, cleavage of the particles, etc. Due to the conversion reaction the particle size and morphology of the active material is changed with every cycle, which might lead to detachment from the current collector mesh, resulting in capacity degradation. In Figure 2- 9, the S-HEO electrode also shows a good performance in C-rate cycling. However, in the long cycling, the electrode material shows an increase in capacity from the 10th to the 70th cycle before degradation, which may be due to the better bonding of S-HEO with the steel mesh substrate, so that the cycling stability can be maintained.

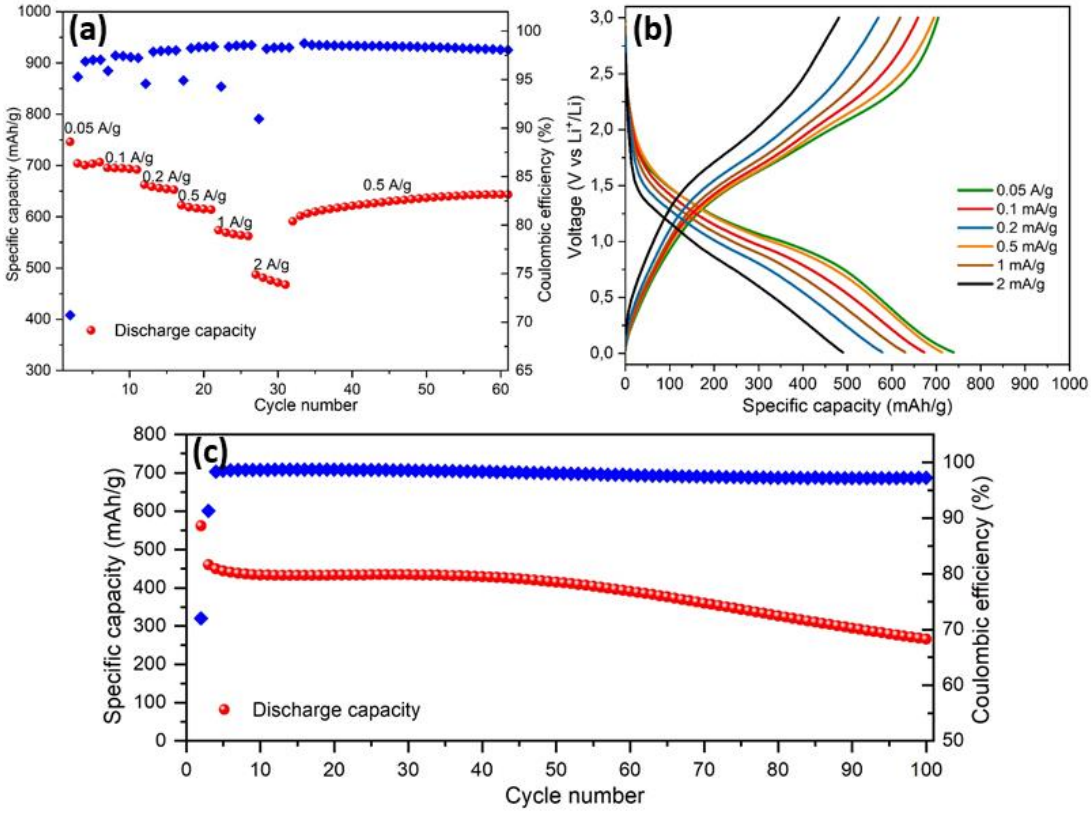

Figure 2- 8: (a) Galvanostatic rate performance test of R-HEOs half-cell at different current densities and 25 ^{o}C in the voltage range between 0.01 and 3 V versus Li^{+}/Li. (b) Voltage profiles of R-HEO half-cell at different currents. (c) Specific discharge capacity of HEOs half-cell and Coulombic efficiency as a function of cycle number with a current density of 500 mA/g in the range between 0.01 and 3 V.

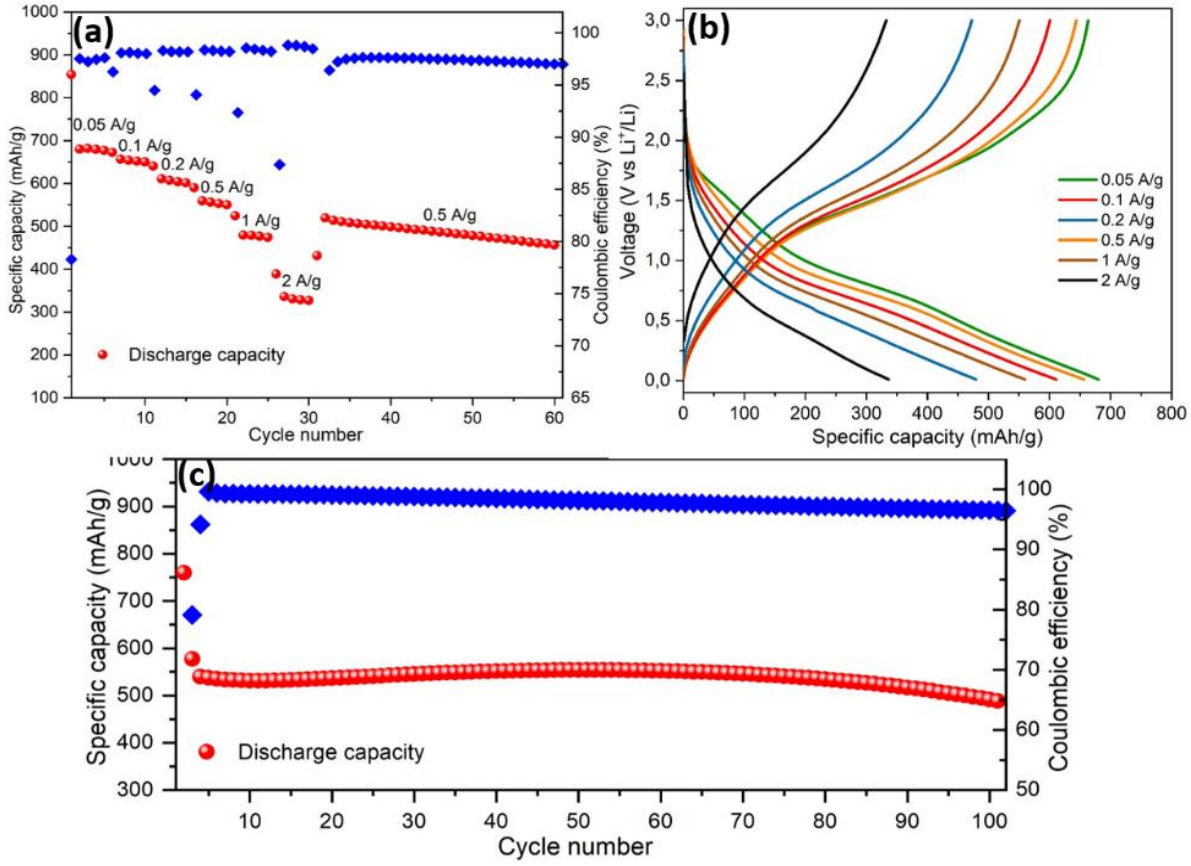

Figure 2- 9: (a) Galvanostatic rate performance test of S-HEOs half-cell at different current densities and 25 °C in the voltage range between 0.01 and 3 V versus Li^+/Li. (b) Voltage profiles of S-HEO half-cell at different currents. (c) Specific discharge capacity of S-HEOs half-cell and Coulombic efficiency as a function of cycle number with a current density of 500 mA/g in the range between 0.01 and 3 V.

2.4. Conclusion

In this work, we successfully synthesized rock salt structured R-HEOs and spinel structured S-HEOs, respectively, by photonic curing, which is a fast, simple and easy-to-operate method. In addition, we also applied the photonic curing method to prepare binder-free electrode materials, and the prepared electrode materials exhibited good cycling performance compared to the traditionally manufactured electrode [122]. Although the steel is heavier than the generally used copper foil collectors, this method of in situ formation of binder-free active material can still provide ideas for developing high energy density electrode materials. The ability to synthesize such complex materials from the liquid phase using photonic curing opens the way to coating of complex objects such as a mesh or wells, since the liquid is uniformly distributed and penetrates fine details of the surface. Additionally, this unique method makes particle coating also feasible, which is shown in the following chapter.

Chapter 3

3. Photonic curing synthesis of high entropy oxide for coating on NCM851005

3.1. Introduction

With the growing use of Li-ion batteries (LIBs) for portable devices, electric vehicles, et al., the demand for devices with higher power and energy density is increasing [60,123,124]. The cathode materials, playing a dominating role in the performance of LIBs, have been studied to increase the energy density to meet the requirement of high performance LIBs. Among the cathode materials, Ni-rich layered lithium transition metal (TM) oxides ($LiNi_xCo_yMn_zO_2$, NCMxyz) with a Ni content of more than 0.8, owing to relatively low cost due to the low range of Co and higher specific capacity based on the Ni redox, have been considered as promising candidates for next-generation advanced LIBs [52,54,57,125]. However, Ni-rich NCM suffers from poor cycle life and capacity fading because the highly reactive Ni^{4+} formed after charging can interact with the electrolyte and promote surface remodeling, resulting in the structural transformation from a layered to a rock salt structure and TM ion dissolution [55,126]. So far, a large number of studies have been conducted on Ni-rich NCM-based materials for LIB cathodes, including doping for improving cation mixing and lattice stability and coating for preventing or inhibiting side reactions between the cathode surface and electrolyte [50,127]. However, the small amount of doping elements in Ni-rich layered transition metal oxide materials makes it very difficult to make their uniform distribution and partial substitution at the doping sites. The modification of nickel-rich layered oxide cathode surface particles with electrochemically inert material coatings such as Al_2O_3 [128,129], TiO_2 [130], ZrO_2 [131], Li_3PO_4 [132,133], etc. to avoid the reaction between cathode materials and electrolyte to improve the structural stability of the particles is a more effective way to improve the cycle life of the corresponding LIBs. Currently, the primary method of coating NCM is wet chemical or atomic layer deposition (ALD) [50]. However, coating also has some drawbacks, such as blocking of ions and electrons, affecting or reducing the Coulomb efficiency, power output, and other electrochemical properties of the LIB. Besides, the wet chemical coating process often proved to be non-uniform, and the more homogeneous coating by ALD coating is inefficient and

unsuitable for industrial mass preparation [134]. Therefore, it is necessary to find materials with good coating function attainable for large-scale industrial production.

High entropy oxides have recently drawn attention due to their unique features. Bérardan et al. found that HEOs ((Mg, Cu, Ni, Co, Zn)O) have excellent lithium-ion conductivity at room temperature, making them a new potential material for lithium conductors [94]. It was found that the ionic conductivity of HEOs increased with increasing lithium doping content, reaching a maximum ionic conductivity at 30% lithium doping (10^{-3} S cm^{-1}), which is five orders of magnitude higher than that of the undoped HEOs (10^{-8} S cm^{-1}). This may be because the cations in HEOs were replaced by Li^{+} ions through an intrinsic charge compensation mechanism, resulting in a combination of +1 and +3 elements or creates oxygen vacancies while maintaining the rock salt structure, opening possible diffusion pathways for lithium ions through the lattice, increasing conductivity. Later, Maciej Moździerz et al. found that the contribution of electronic conductivity increases significantly with increasing lithium doping content in addition to ionic conductivity [95]. Therefore, the Li-doped HEOs (LiHEOs) should be classified as mixed ionic-electronic conductors rather than potential candidates for solid electrolytes. With the increase of the ionic contribution, the electronic contribution was determined to increase significantly with the addition of Li in the (Co, Cu, Mg, Ni, Zn)$_{1-x}$Li$_x$O series. Therefore, LiHEO could be a candidate for coating materials because of its good electronic and ionic conductivity. Generally, the synthesis of HEO must be performed at high temperatures (>1000 °C) or requires very long mechanical ball milling times. However, high temperatures or long ball milling can cause structural damage to NCM, so the conventional method of synthesizing HEO is unsuitable for coating. It should be noted that photonic curing can rapidly synthesize HEO with a single-phase rock salt structure at low temperatures. Therefore, by the photonic curing technique, NCM851005 was coated with HEO and LiHEO, respectively, to form a uniform coating on the surface of NCM851005 powder. This coating effectively avoids the reaction between the electrode material and the electrolyte, thus significantly improving the structural stability of the NCM particles and, in turn, the cycling stability of NCM851005. In addition, by comparing LiHEOs and HEO-coated NCM851005, we found that the improvement of ionic conductivity and electronic conductivity after lithium doping also played a vital role in improving performance.

3.2. Experiment

3.2.1. Materials preparation

LiHEO coated NCM851005

A nitrate precursor solution with a production of 20 mg of $Li_{0.33}(Mg, Cu, Ni, Co, Zn)_{0.67}O$ (LiHEO), 8.34 mg $LiNO_3$, 12.59 mg $Mg(NO_3)_2{\cdot}6H_2O$, 14.29 mg $Co(NO_3)2{\cdot}6H_2O$, 14.28 mg $Ni(NO_3)_2{\cdot}6H_2O$, 11.42 mg $Cu(NO_3)_2{\cdot}2.5H_2O$, and 14.61 mg $Zn(NO_3)_2{\cdot}6H_2O$, was dissolved in 0.48 mL ethanol, then 1 g NCM851005 (BASF) was added with a constantly stirred at ambient temperature for 60 minutes, then heated at 60 °C to enable the solution evaporation. The prepared powder is evenly dispersed on a 5*5 cm silicon wafer and put for the photonic curing at 3 kV for 75 s, shaking each time evenly and cooling to room temperature, irradiation was repeated 6 times.

HEO coated NCM851005

A nitrate precursor solution with a production of 20 mg of (Mg, Cu, Ni, Co, Zn)O (HEO), 14.62 mg $Mg(NO_3)_2{\cdot}6H_2O$, 16.59 mg $Co(NO_3)_2{\cdot}6H_2O$, 16.58 mg $Ni(NO_3)_2{\cdot}6H_2O$, 13.26 mg $Cu(NO_3)_2{\cdot}2.5H_2O$. and 16.96 mg $Zn(NO_3)_2{\cdot}6H_2O$ dissolved in 0.48 mL ethanol. The other experimental steps are the same as for LiHEO coated NCM851005.

The LiHEO and HEO coating is prepared as described above through a wet chemical method with photonic curing synthesis followed by annealing. In this process, commercial NCM851005 particles were suspended in the nitrate precursor solution of LiHEO and HEO. After ethanol was evaporated, this procedure was followed by photonic curing to form LiHEO/HEO coating layers. The LiHEO and HEO coated powders were heated at 600 °C for 2 h under air and oxygen respectively to remove LiOH and Li_2CO_3 formed during the coating process due to contact with air and ethanol and achieve a uniform coating layer. The powders are then stored in an Ar-filled glovebox. A schematic of the photonic curing process in depicted in Figure 3- 1.

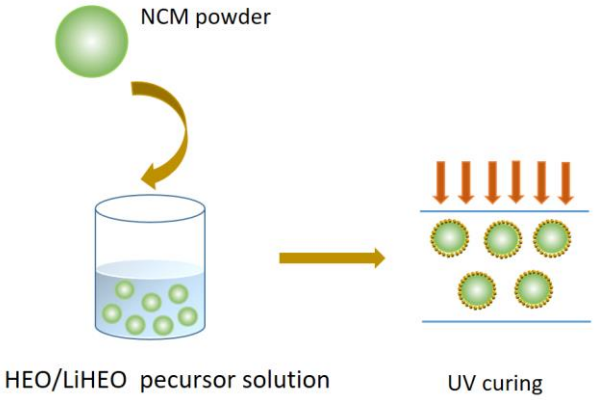

Figure 3- 1: Schematic illustration of LiHEO/HEO coating on NCM851005.

3.3. Results and discussion

3.3.1. Characterization of coating microstructure

In this work, HEO and LiHEO were used for coating NCM851005, named HEO@NCM851005 and LiHEO@NCM851005, respectively. As shown in Figure 3- 2, Raman tests indicate that Li_2CO_3 (1075 cm^{-1}) impurities were generated on the surface of the coated NCM, which could be the reason for the poor electrochemical performance of the coated NCM. Therefore, in order to remove the impurities from the surface of particles, the material was calcined in oxygen and air, respectively. Additionally, the calcination is expected to enhance contact and uniformity of the coating layer. The Raman spectra show successful elimination of Li_2CO_3 after calcination in both air and oxygen. Herein, this chapter focuses on the material properties of bare and coated NCM after heat treatment in air and oxygen and investigates the mechanism responsible for the enhancement of cycling stability.

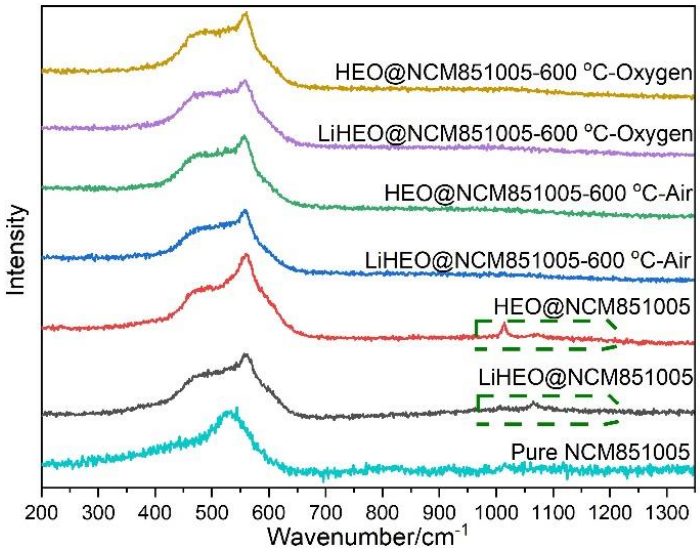

Figure 3- 2: Raman spectra of coated NCM851005 calcined in Air and oxygen.

As shown in Figure 3- 3, The XRD patterns of NCM851005, HEO coated NCM851005, and LiHEO coated NCM851005 are compared. All reflections in the XRD patterns are indexed based on a layered hexagonal structure with the $R\bar{3}m$ space group without apparent differences. No shifts are observed in the XRD patterns of the coated NCM851005, indicating the absence of expansion and contraction due to the HEO and LiHEO coatings. The different splitting of the (006)/(102) and (108)/(110) reflections of all samples demonstrates that these materials have a well-developed layered structure. This suggests that the coating process and heat treatment and atmosphere do not affect the NCM851005 crystal structure. Notably, the diffraction peaks corresponding to the rock salt of HEO and LiHEO coating layers are absent. This might be because the coating layer thickness is beyond XRD resolution.

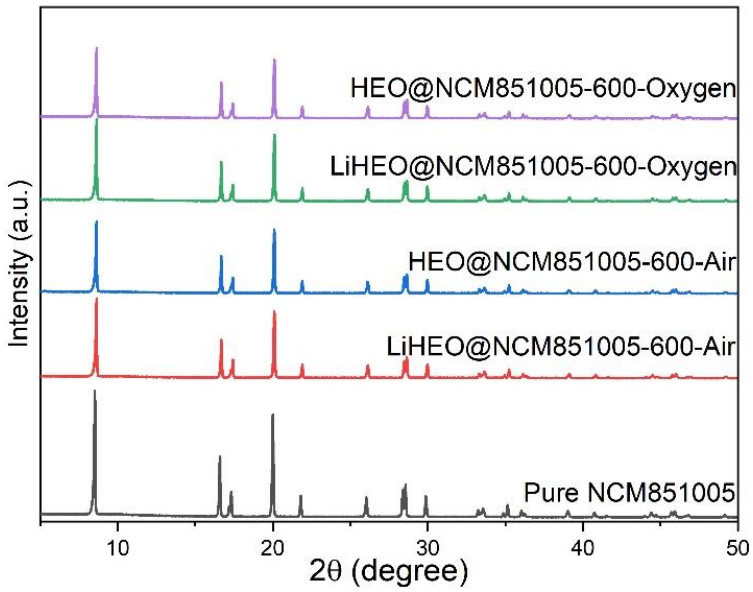

Figure 3- 3: XRD (Mo K-alpha irradiation) patterns of NCM851005, HEO coated NCM851005, and LiHEO coated NCM851005. Coated materials are calcined under air and oxygen atmosphere.

Figure 3- 4 shows the SEM morphological characteristics of the materials after air calcination. The images show that the shape of the samples before and after the coating is similar, indicating that the effect of the coating process on the surface of NCM851005 is negligible. As shown in the high magnification images of Figure 3- 4d-f, the top surface of the bare NCM851005 secondary particles appears rather clean and smooth, whereas the surface morphology of both HEO and LiHEO coated NCM851005 exhibited a rough surface morphology. EDX mapping (Figure 3- 4g) was performed to further determine the distribution of LiHEO on the surface of NCM851005. The elemental mapping of Ni, Co, Mn, O, Mg, Cu, and Zn in Figure 3- 4g shows that these elements are uniformly distributed in the selected areas, indicating that HEO is uniformly coated on the NCM851005 microspheres.

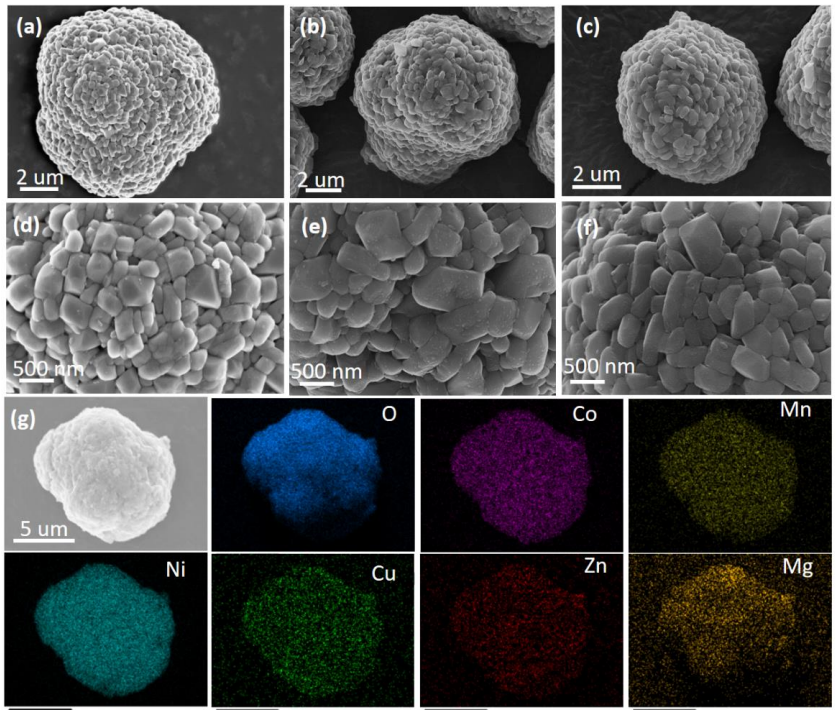

Figure 3- 4: (a) SEM image of pure NCM851005, (b) HEO coated NCM851005, (c) LiHEO coated NCM851005, and corresponding magnified images (d-f); (g) SEM-EDX mapping of LiHEO coated NCM851005

To further confirm the formation and structure of the HEO and LiHEO coating layer, TEM measurements were conducted for both HEO coated NCM851005 (Figure 3- 5) and LiHEO coated NCM851005 (Figure 3-6) samples after air calcination. As shown in Figure 3- 5 and Figure 3-6 of coated NCM851005, a uniform coating of 10-20 nm thick was deposited on NCM851005; the EDX images show that the color of Co in the coating is brighter compared to the color within the NCM851005 particles because the content of Co in the coating is higher than that in the NCM851005 particles, which also proves that Co is uniformly distributed in the coating. And the content of Ni in the coating is smaller than that in the NCM851005 particles. Therefore, although the color of Ni in the coating layer is not as bright as that within the NCM851005 particles, it is also relatively uniformly distributed. Additionally, Mg is also uniformly distributed on the surface in the nanoscale. However, Cu and Zn did not show significant segregation in the coating layer, which we speculate may be due to Cu and Zn diffusion through the surface of the NCM851005 particles into the interior of the particles during the preparation process, which might theoretically contribute to the improvement of the cycling performance of NCM851005 [135]. Figure 3-6bc shows the SAED and FFT maps of the internal and surface coating of LiHEO coated NCM851005, it can be observed that the planar spacing of 0.238 nm, 0.251 nm, and 0.500 nm corresponds to the (220), (104), and (003) crystal planes of NCM851005, respectively. This data is consistent with the XRD results. The HR-TEM image of the surface of NCM851005 is shown in Figure 3-6c where three lattice stripes are present, corresponding to the rock salt (003) plane

with a planar spacing of 0.214 nm, the (012) plane with a planar spacing of 0.238 nm, and the (220) plane with a planar spacing of 0.250 nm. These results indicate that LiHEO with rock salt structure is formed and uniformly coated on the surface of NCM851005.

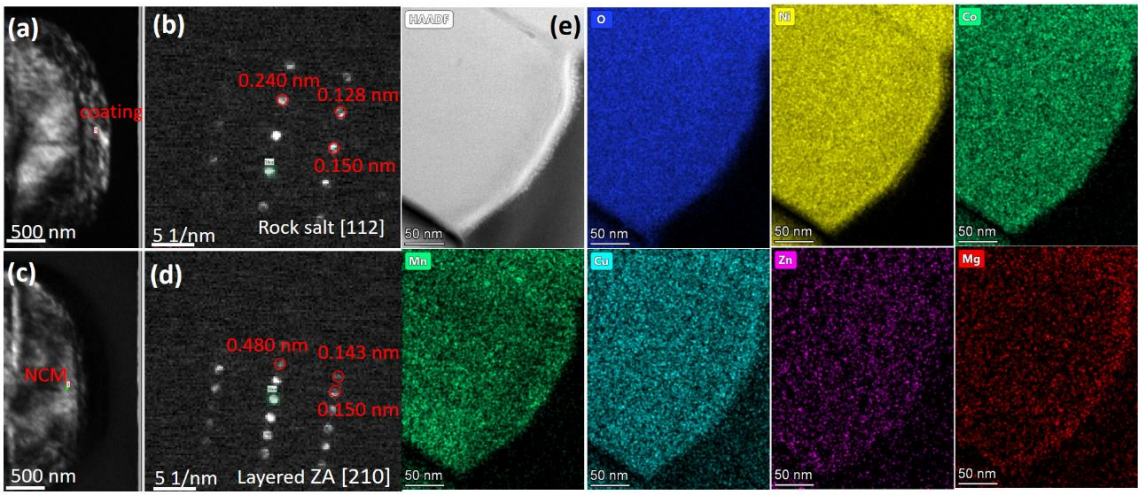

Figure 3- 5: STEM-HAADF imaging of the HEO coated NCM851005 with EDX mapping and FFT patterns. (a-b) show a rock salt structure of coating layer, and (c-d) show a layered structure of internal NCM851005.

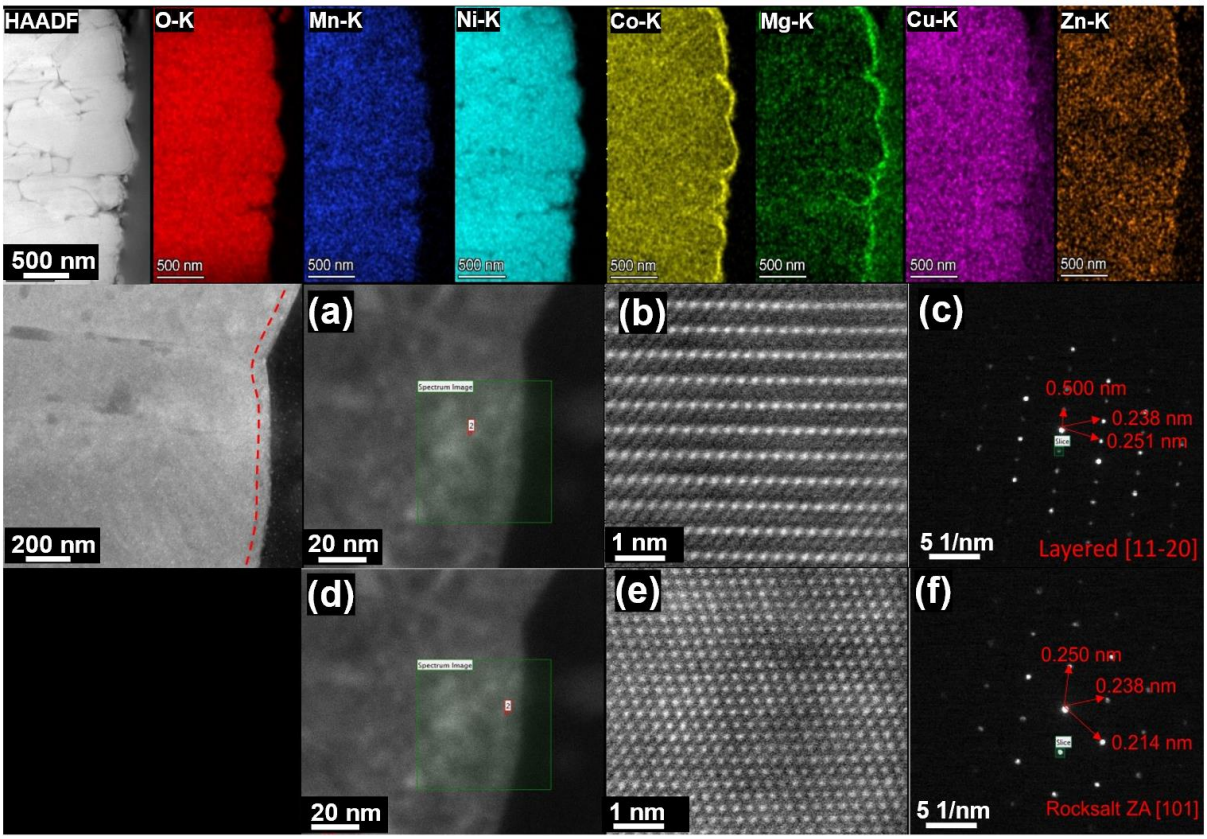

Figure 3-6: STEM-HAADF imaging of the LiHEO coated NCM851005 with EDX mapping, SEAD, and FFT patterns corresponding to atomic-level imaging marked by the green box. (a-c) show a layered structure of internal NCM851005, and (d-f) show a rock salt structure of coating layer.

3.3.2. Enhanced capacity retention and voltage stability

To reveal the effect of LiHEO/HEO surface modification of NCM851005 on electrochemical performance, a series of electrochemical tests were performed. Figure 3- 7 shows the electrochemical characteristics of NCM851005 coated with HEO and LiHEO, both of which have lower capacity than pure NCM in different rate tests. The profiles of coated NCM851005 show higher over potential in different rate tests than the pure active material. Therefore, a calcination step was introduced to ensure a better contact and a more uniform coating layer.

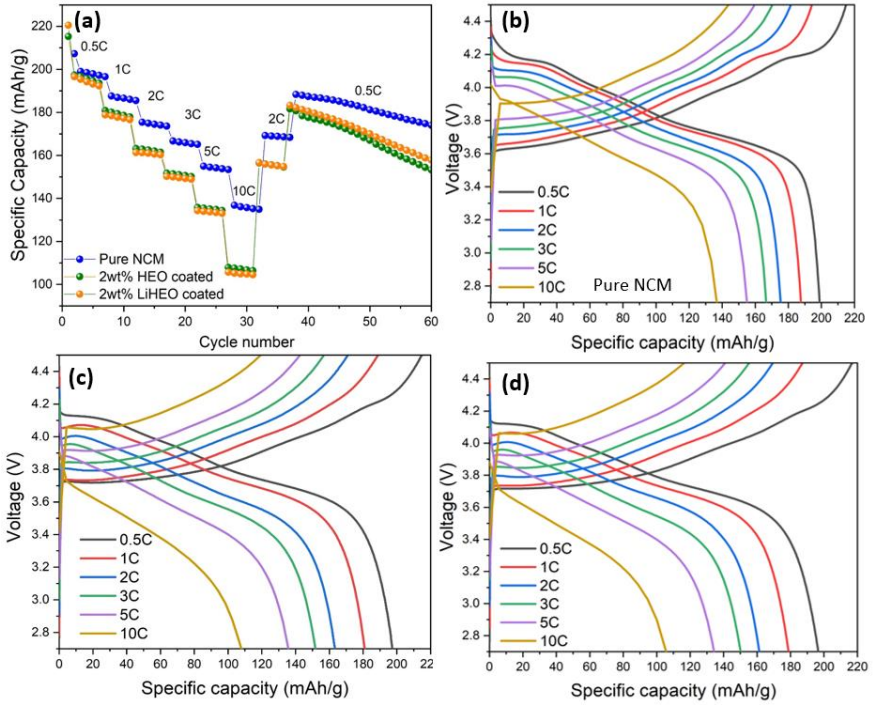

Figure 3- 7: Galvanostatic cycling of NCM851005, HEO coated NCM851005, and LiHEO coated NCM851005 without calcination (a) Rate capability measured in the voltage range of 2.7-4.5 V vs. Li^+/Li. (b-d) Cycling profiles at different current densities of 0.5C-10C.

Figure 3-8a-b show the rate test and long cycle performance of active materials calcined in air at 1C between 2.8-4.3 V vs. Li^+/Li, respectively. The rate performances of all the samples, evaluated at various rates ranging from 0.5 to 10 C (theoretical capacity 200 mAh g^{-1}) in the voltage range between 2.8 and 4.3 V, are displayed in Figure 3-8a. In the rate performance test, the capacities of LiHEO coated NCM851005 at 0.5C, 1C, 2C, 3C, and 5C showed comparable capacity to those of the uncoated NCM851005. On the contrary, the capacity of LiHEO coated NCM851005 is lower when the current increases to 10C, which may be due to the lower Li-ion conductivity of the LiHEO layer than NCM851005 at higher current. However, it is noteworthy that the LiHEO coating material shows a higher capacity than the uncoateed NCM851005 after multiples of cycles at different rates

and going back to 0.5 C, which implies that the LiHEO coating material has higher cycling stability after air calcination. In the rate test of HEO coated NCM851005, the capacity of HEO coated NCM851005 is lower than that of LiHEO coated NCM851005 and uncoated NCM851005 in almost all current tests, which may be due to the lower electron conduction and ionic conductivity of HEO, thus affecting the electrochemical performance. In the long cycle performance after 200 cycles, the capacity retention of LiHEO coated NCM851005 is 97.6%, compared to 97.5% and 87.9% for HEO coated NCM851005 and uncoated NCM851005, respectively. Although the capacity of LiHEO and HEO-coated NCM851005 are lower than that of NCM in the first 20 cycles, the capacity after the coating was constantly higher than that of pure NCM851005 in the next cycles of the test. This is probably because the coating does not provide lithium-ion storage capacity, in addition, the coating might initially hinder the diffusion of a fraction of lithium-ions, resulting in their inability to fully de-intercalate/intercalate in the NCM851005 lattice during cycling [129]. In order to exclude the effect of air calcination on NCM, bare NCM calcined at 600 °C in air was also tested separately under the same conditions, and the results showed that the cycle stability of NCM calcined at 600 °C was better than that of pure NCM, although the initial capacity was reduced, but it was also inferior to that of coated NCM. In addition to the increased stability due to the reduced capacity, on the other hand, according to reported literature [136], it may be that the calcined NCM still has traces of Li_2CO_3 on the surface, which is also responsible for the improved cycling stability. Of course, it also shows that the NCM with LiHEO and HEO coating layer is a very effective method for coating NCM. However, in the long cycling of coated NCM calcined in oxygen, the capacity of the material decreased more rapidly than that of the original NCM as well as the coated materials calcined in air. This indicates that there is a synergetic effect between the coating material and the carbonate traces on the surface of the NCM particles, that were not detectable by Raman, enhancing the cycling stability by preventing interfacial reactions with the electrolyte [137,138].

In Figure 3-8c-e, the charge-discharge profiles of LiHEO coated NCM851005 and HEO coated NCM851005 were similar to those of uncoated NCM851005 sample, which indicates that the coating did not change the structure of the NCM851005 sample. It can be observed from the charge/discharge curves (Figure 3-8) that LiHEO and HEO coated NCM851005 are more stable compared to pure NCM851005 in both capacity and discharge voltage. The voltage polarization of LiHEO coated NCM851005 does not increase compared to the bare NCM, which also indicates that the coating of LiHEO can provide diffusion channels for ions and electrons during the charge and discharge. In addition, the stability of the voltage plateau indicates that the coating reduces the reaction of the electrolyte with the electrode material and maintains the integrity of the material particles.

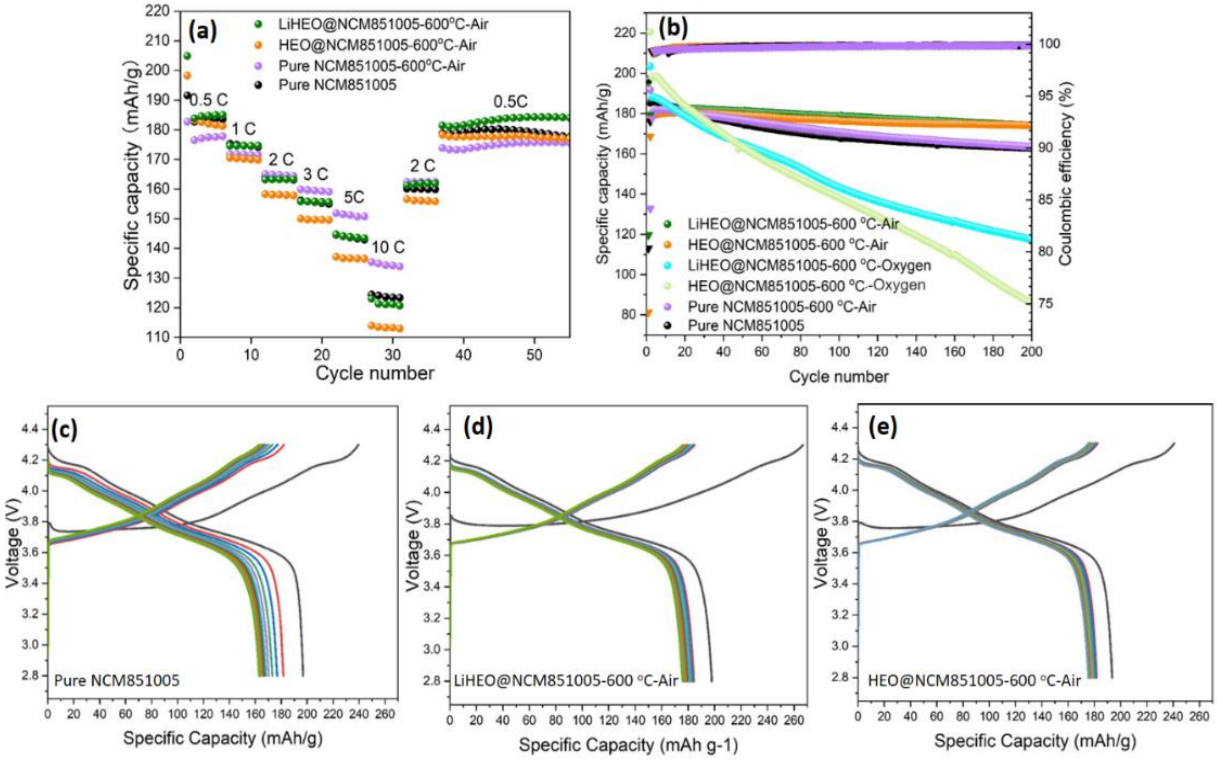

Figure 3-8: Galvanostatic cycling and rate capability of NCM851005, HEO coated NCM851005, and LiHEO coated NCM851005 (a) Cycling capacity at 1C measured in the voltage range of 2.8-4.3 V vs. Li^+/Li. (b) Cycling capacity at 0.5 C measured in the voltage range of 2.8-4.3 V vs. Li^+/Li (c-e) Cycling profiles at from 1^{st} – 350^{th} (1C = 200 mA g^{-1}).

To observe the electrochemical behavior related to the phase transition of the material, dQ/dV is applied in Figure 3-9. In general, NCM851005 undergoes a series of phase transitions during the insertion and extraction of Li-ions, from hexagonal H1 via monoclinic M to hexagonal H2 and hexagonal H3 phases [139]. The phase transition of NCM851005 is similar to that of $LiNiO_2$ in the H2/H3 phase transition region, accompanied by an abrupt c lattice parameter contraction, leading to secondary particle fracture and capacity decrease. Therefore, as the cycling continues, the position of the redox peaks shifts, and the peak area decreases with each cycle. This indicates that the polarization of the cell becomes more pronounced as the number of cycle's increases. As shown in Figure 3-9a, the oxidation peak of the original NCM851005 shifted to a higher potential. The reduction peak shifted to a lower potential during cycling, and the corresponding peak area was significantly reduced. The poor reversibility of the H2-H3 phase transition and the rapid loss of the H3 phase indicate the poor structural stability of the NCM, which is also responsible for the faster decay in the capacity of the NCM samples. In contrast, the voltage hysteresis with LiHEO coating and HEO coating are significantly suppressed, the relative dQ/dV curves of the coated NCM change slowly within the first 200 cycles, and the H3 phase becomes smaller and the H2-H3 reversibility is generally better.

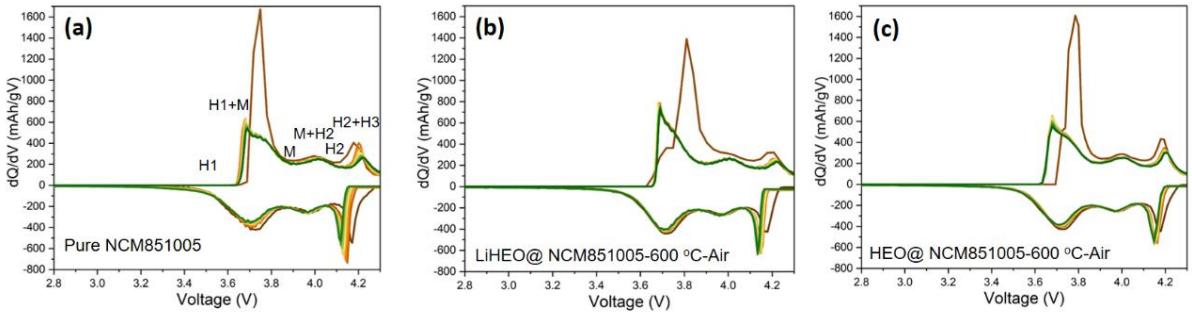

Figure 3-9: (a), (b) and (c) are dQ/dV of NCM851005, HEO coated NCM851005, and LiHEO coated NCM851005 from 1st – 350th at 1C measured in the voltage range of 2.8-4.3 V (1C =200 mA g^{-1}).

Given the coated NCM exhibited structural stability during battery cycling, we tried to expand the voltage range of the cycle and changed the test to 2.7-4.5V vs. Li^+/Li, shown in Figure 3-10. As can be seen from the graph, in the rate test, the rate test of the coated materials showed the same situation as the 2.8-4.3V test, with a lower capacity at higher rate. Meanwhile, in the long cycle test, the LiHEO/HEO coated material showed good stability, with a capacity of 183 mAh g^{-1} after 150 cycles, while the bare NCM851005 showed a capacity of 172 mAh g^{-1}. This indicates that the coating also plays an effective role in the stability of the material in the high voltage range, which is useful for investigating the application of high energy density materials.

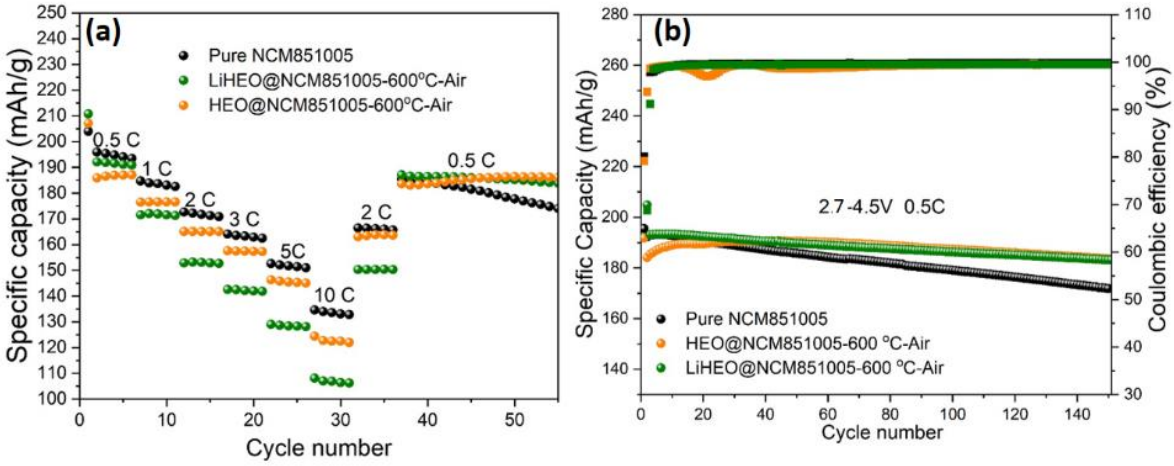

Figure 3-10: Rate performance of NCM851005, NCM851005 coated HEO, and NCM851005 coated LiHEO in the voltage range of 2.7–4.5 V vs. Li^+/Li at room temperature (1C =200 mA g^{-1})

3.3.3. Mechanism of enhanced cycling stability

The microstructural degradation of bare NCM851005 and LiHEO/HEO coated NCM851005 after 200 cycles were detected by FIB-SEM and STEM–HAADF. After 200 cycles, the three particles exhibit significantly different microstructural characteristics, as shown in the SEM images of Figure 3-11. The pristine electrode material prior to cycling is shown in Figure 3-11a. The large

NCM primary particle consists of smaller secondary particles and is surrounded by the binder and carbon black. After 200 cycles a high density of intergranular cracks are formed around the NCM secondary particles of the uncoated NCM851005 (Figure 3-11), which is usually considered one of the essential structural degradation mechanisms leading to cathode failure during cell cycling. Micro cracks lead to the penetration of the electrolyte along the grains and the reaction between the penetrating electrolyte and interior particles, accelerates structural degradation and side reactions. In contrast, reduced cracking is observed in HEO coated NCM851005 (Figure 3-11c). Surprisingly, these crack features did not appear in the LiHEO coated NCM851005 sample (Figure 3-11d). LiHEO and HEO coated NCM crack generation was significantly reduced around the secondary particles of the coated structures compared to that of the bare sample.

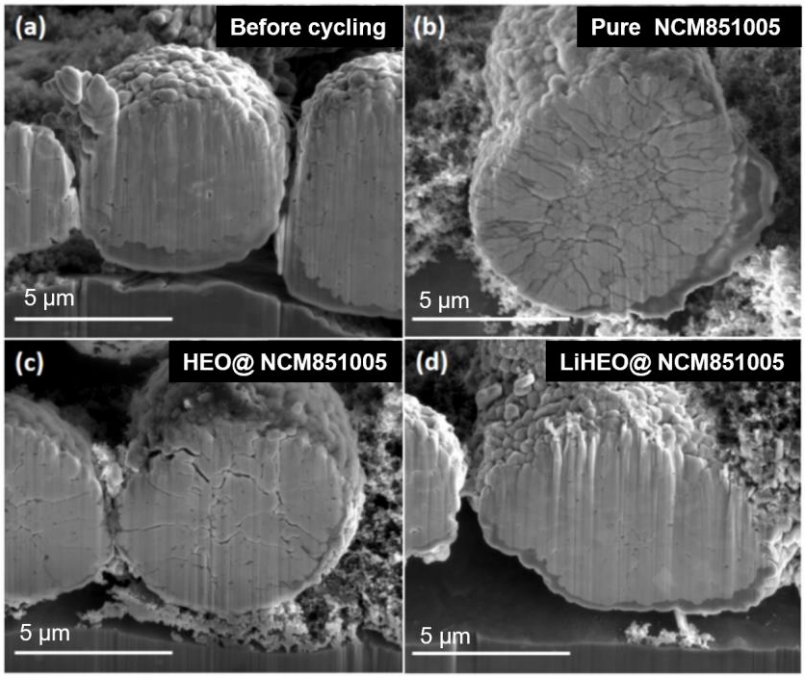

Figure 3-11: FIB-SEM of the interior of an NCM851005 secondary particle of NCM851005 before cycling (a), NCM851005 (b), HEO coated NCM851005 (c), and LiHEO coated NCM851005 (d) after 200 cycles. Scale bar=5 um

To reveal the effect of LiHEO and HEO coating on the material structure, the structural evolution of the uncoated NCM, HEO and LiHEO coated samples on the surface and internal secondary particle surface after cycling was investigated by STEM-HAADF imaging technique and is shown in Figure 3-12, Figure 3-13 and Figure 3-14, respectively. A rock salt-like phase transition occurred in a thin layer of the surface of particles cycled in Figure 3-12b, Figure 3-13b, and Figure 3-14b for the enlarged Figure 3-12c of the surface particles, and in Figure 3-12d, Figure 3-13d, and Figure 3-14d (embedded FFT), respectively. For LiHEO coated NCM851005, the phase transition of the material is from a layered structure to a rock salt structure with a rock salt-like

thickness of about 5 nm while no significant phase transition occurs at its internal grain boundaries. This may be due to the fact that the coating layer prevents the electrolyte from penetrating the primary particle along the grain boundaries of the secondary particles, so the reaction between NCM and the electrolyte occurring on the surface of the secondary particles is eliminated during cycling. In contrast, the particle surface of NCM (Figure 3-12) shows typical structural changes after cycling, with the surface showing a phase change of roughly a depth of about 90 nm, and the structure of its secondary particle surface is also disrupted during cycling. In contrast, the surface of HEO also shows the same severe phase change as NCM with a depth of about 90 nm, while the LiHEO coated surface of the secondary particles shows only a slight phase change. This also corresponds to the fact that the HEO-coated NCM shows only a small amount of cracks in the FIB-SEM.

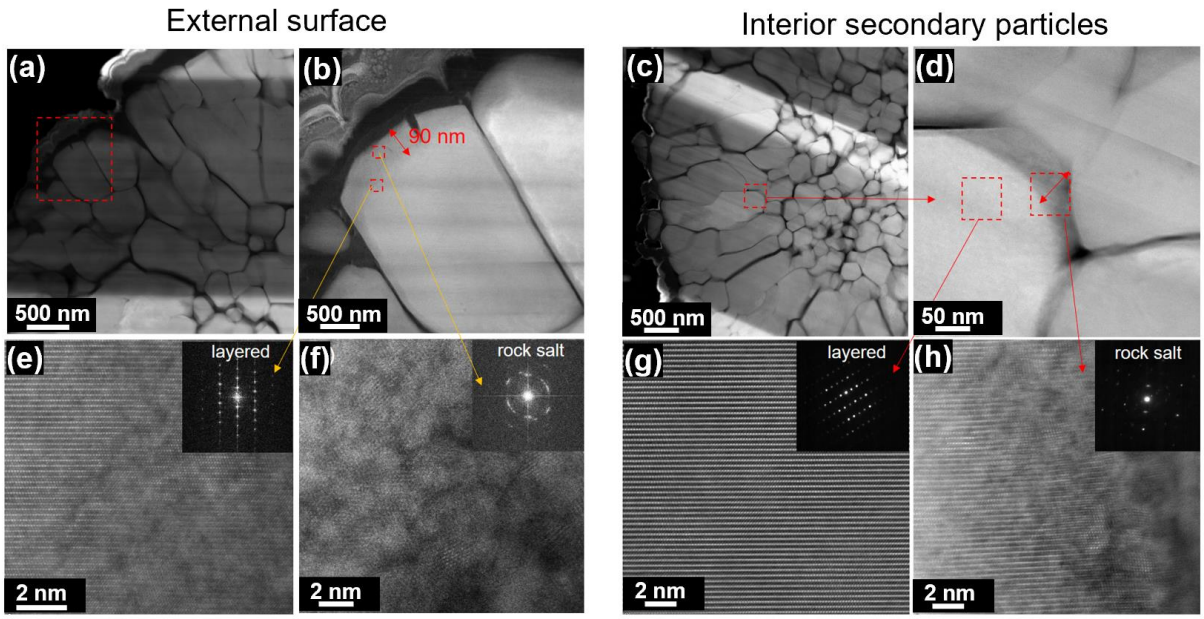

Figure 3-12: The structural degradation of NCM851005 after 200 cycles evaluated by STEM–HAADF imaging (a–d), and atomic-level STEM–HAADF imaging (e–h) which correspond to the high magnification image of the regions in b, d marked by red boxes, respectively.

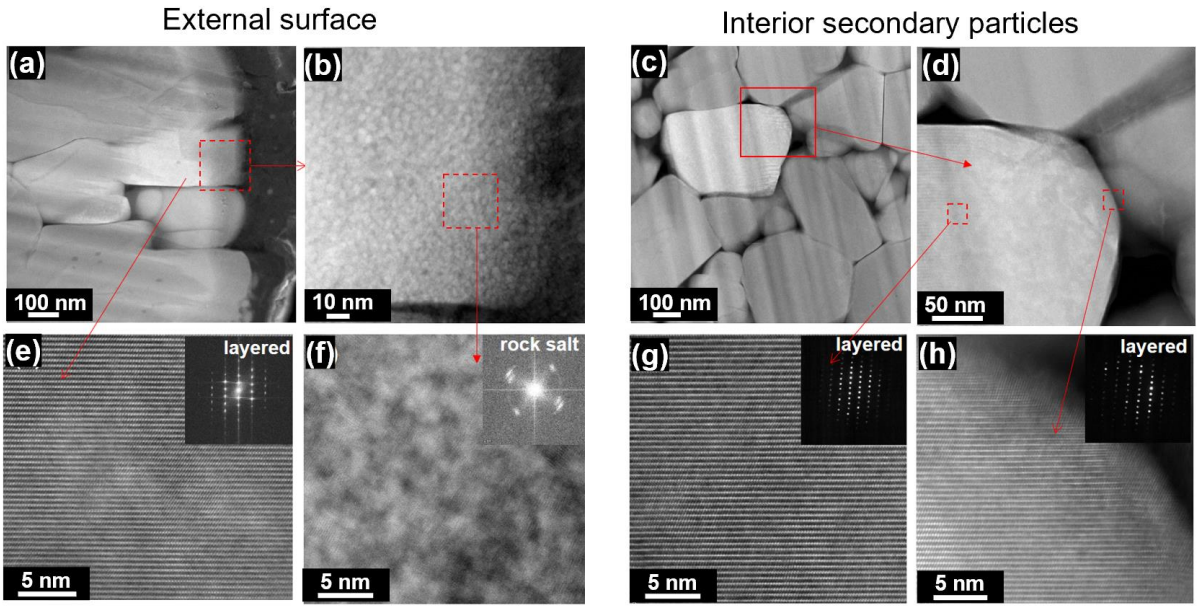

Figure 3-13: The structural degradation of HEO coated NCM851005 after 200 cycles evaluated by STEM–HAADF imaging (a–d), and atomic-level STEM–HAADF imaging (e–h) which correspond to the high magnification image of the regions in b, d marked by red boxes, respectively.

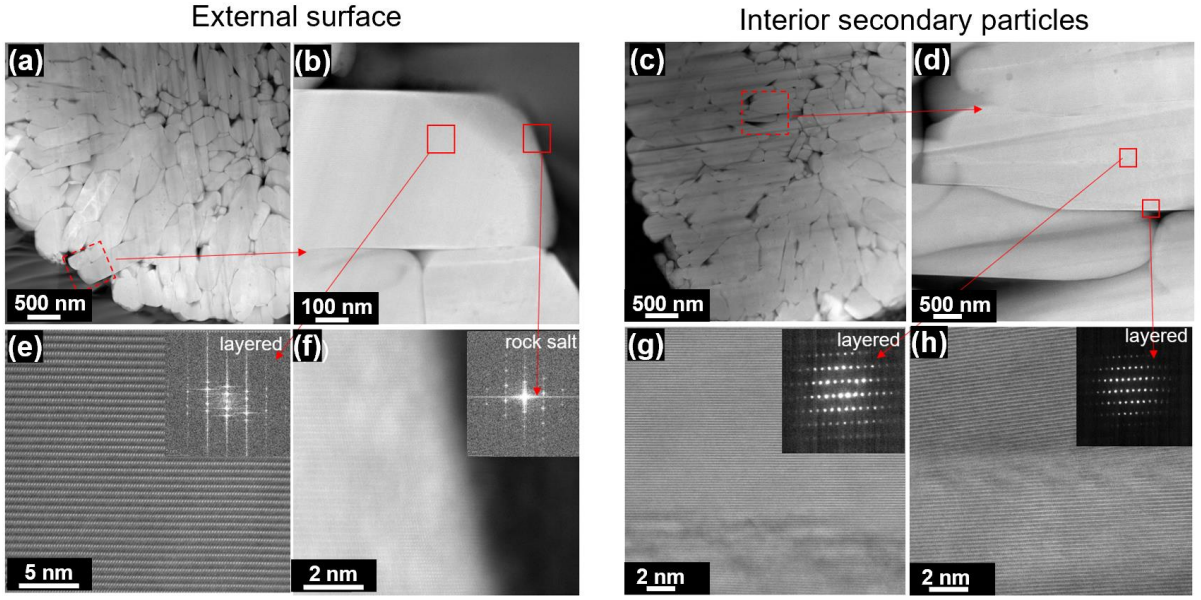

Figure 3-14: The structural degradatio of LiHEO coated NCM851005 after 200 cycle evaluated by STEM–HAADF imaging (a–d), and atomic-level STEM–HAADF imaging (e–h) which correspond to the high magnification image of the regions in b, d marked by red boxes, respectively.

3.4. Conclusion

Lithium-doped high entropy oxide (LiHEO) is a promising coating material for cathode materials due to its high ionic and electronic conductivity, but the harsh conditions for synthesis limit its application. Therefore, a photonic curing strategy is proposed for synthesizing LiHEO/HEO

coatings, and a nanoscale homogeneous coating layer was successfully formed on the NCM851005 particles. NCM851005 with LiHEO-modified surface showed excellent electrochemical cycling stability, with an increased capacity retention of 91% at 1C after 350 cycles. Excellent electrochemical performance attributed to the uniform coating on the material surface prevents structural changes caused by the reaction between the electrode material and the electrolyte. Compared to the bare NCM851005, the crack formation around the secondary particles is significantly reduced after coating, which prevents the electrolyte penetration through the primary NCM particle and further reaction with the surface of the secondary particles. This results in a stable average discharge voltage and a more stable cycling performance even in the high cut-off voltage range. In addition, by comparing the cycling performance of HEO and LiHEO coated materials, we found that good ionic and electronic conductivity also plays an important role in improving the cycling stability of the battery. Thus, this work shows that the use of Li-ion conductive films, with additional electronic conductivity, provides an opportunity to build high-performance cathode materials for Li-ion batteries. More work is needed for an in depth understanding of the mechanisms responsible for enhanced performance of LiHEO coated NCM after air calcination opposed to oxygen calcination, e.g. determining the influence of residual Li_2CO_3 on the surface and elemental diffusion from the coating layer into the NCM particles.

The successful utilization of photonic curing in coating technology provides an opportunity to open up new materials and new ideas for coating technology. Finally, the successful application of HEO coatings on high nickel NCM shows the potential of the coating for other cathode materials such as $LiMnO_4$ and other high-voltage cathode materials.

High entropy oxides have proven to be excellent conversion anodes [79,122] and within this work deliver a high potential as coatings for cathode active materials enhancing their stability. Therefore, other types of conversion materials are explored in the following, aiming to exploit the beneficial elemental interactions in high entropy materials.

Chapter 4

4. Mechanochemical synthesis of novel rutile-type high entropy fluorides

The work in the following chapter was published in Journal of Materials Chemistry A [140]

4.1. Introduction

One important class of materials are metal fluorides, due to their special properties and manifold applications. Inorganic metal fluorides find applications in catalysis, as electrode active materials, in superconducting devices, as corrosion protection etc.[141–144]. Non-binary compounds, like Co-doped MgF_2, can show additional properties, like in the mentioned case the modification of surface acidity properties whilst maintaining the rutile phase [145]. Ternary metal fluorides for instance, $AgCuF_3$,[146] $Cu_xFe_{1-x}F_2$ or Li_3MF_6 (M=V, Cr, Mn, Co, Fe) demonstrate reversible conversion reactions with Li-ions,[147–149] rendering them as potential energy storage materials. It is also found that multi-element incorporation described by the high entropy concept is beneficial for electrochemical storage in sodium-ion batteries (SIB). This includes well-designed open framework strategies and doping of conversion type materials [150] such as ReO_3-type FeF_3 [151] [152] yielding high-performance SIB cathodes. The transfer of the high entropy concept to transition metal fluorides in general, seems to be a promising approach for novel catalytic and electrochemical applications [153,154]. First reports about rare-earth-based fluorite and perovskite structured high entropy fluorides and rock-salt structured oxyfluorides have shown promising properties for energy storage, optical and catalytic properties [141,155,156]. Wang et al. reported that the existence of weak bonds between transition metal (TM)-fluoride species, intrinsic structural defects and a distortion of the HEM lattice due to different TM constituents, can provide enhanced oxygen evolution reaction (OER) activity [141]. Due to their special electronic configuration and surface complexity, HEMs are in general expected to provide desirable electrocatalytic properties [157,158].

In the present work, we described the synthesis and an in-depth characterization of multi-cationic (with 4 to 7 cations) rutile ($P42/mnm$) structured medium- (4 cations) and high-entropy (5-7 cations) fluorides (MEF and HEFs, respectively). Considering a solid solution state, the configurational entropy for a 7-cation containing compound can be calculated to be 1.95R (based on Equation 4, where R is the universal gas constant). These compounds were synthesized using a straightforward and scalable mechanochemical milling process, therefore avoiding more complex synthesis procedures as reported in previous publications about HEFs [159]. The characterization of the HEFs is demonstrated to support the assumption of a solid solution structure of the compounds, which is imperative for confirming the high configurational entropy. By using various measurement techniques, stretching of M-F bonds at the surface of the nanocrystalline particles was detected, resulting in different chemical environments, as similarly described for nanosized FeF_2 particles by Ramansamy et al. [160].

4.2. Synthesis and structural characterization of HEF based compounds

Commercially available analytical grade transition metal difluorides with purity >99 % (such as MnF_2, FeF_2, CoF_2, NiF_2, CuF_2, ZnF_2, MgF_2; Alfa Aesar) were used for this work. All the chemicals were used for the synthesis without any further purification steps. These HEF materials were prepared by long-term high energy milling process carried out at 500 rpm for 48 h in WC jar (WC ball to powder weight ratio as 20:1). Using this route, HEF samples containing 4, 5, 6 and 7 elements equimolar ratios were produced. All samples were prepared in Ar atmosphere (H_2O < 0.5 ppm, O_2 < 0.5 ppm). In this work, a novel class of high entropy materials, the rutile-type high entropy fluorides (HEFs) is presented. The $(CuNiFeZn)F_2$, $(CuNiFeCoZn)F_2$, $(CuNiFeCoMn)F_2$, $(CuNiFeCoZnMn)F_2$ and $(CuNiFeCoZnMnMg)F_2$ are synthesized and characterized, hereinafter labeled as MEF4, HEF5_Zn, HEF5_Mn, HEF6, and HEF7, respectively, based on the number of incorporated cations. Configurational entropy calculations are provided in Table 4- 1 and ranges from 1.39R for the 4-cation system to a maximum of 1.95R in case of the 7-cation system. Materials crystallizing in a rutile structure, lie in the tetragonal $P42/mnm$ space group. The rutile structure is composed of cations, which are coordinated by the anions in a distorted octahedral symmetry. The MF6 octahedrons share two opposing edges with the adjacent octahedra and therefore form a chain-like structure. These chains are connected by the corners of the octahedra, the rutile structure is commonly known from oxide and fluoride compounds, e.g. TiO_2, FeF_2, ZnF_2, etc. The respective cations for the MF_2 HEFs (M= Co, Cu, Mg, Ni, Zn, Mn, Fe) are selected by adhering to the Hume-Rothery and Pauling's rules, which propose similarity in ionic radii, coordination numbers and crystal structures to successfully achieve a solid solution [161].

Table 4- 1: Configurational entropy values (S_{config}) of the synthesized HEF according to equation 4.

Fluoride type	Compound	S_{config} value
MEF4	$(Cu_{1/4}Ni_{1/4}Fe_{1/4}Zn_{1/4})F_2$	1.39R
HEF5_Zn	$(Cu_{1/5}Ni_{1/5}Fe_{1/5}Co_{1/5}Zn_{1/5})F_2$	1.61R
HEF5_Mn	$(Cu_{1/5}Ni_{1/5}Fe_{1/5}Co_{1/5}Mn_{1/5})F_2$	1.61R
HEF6	$(Cu_{1/6}Ni_{1/6}Fe_{1/6}Co_{1/6}Zn_{1/6}Mn_{1/6})F_2$	1.79R
HEF7	$(Cu_{1/7}Ni_{1/7}Fe_{1/7}Co_{1/7}Zn_{1/7}Mn_{1/7}Mg_{1/7})F_2$	1.95R

4.3. Structural characterization of HEF based compounds

4.3.1. X-ray diffraction

A similar range of lattice constant values is exhibited by all binary fluorides, ZnF_2 (a=b= 0.4705 nm and c= 0.3134 nm, as given by ICSD#9169), which was used as the reference for refining the X-ray diffraction (XRD) patterns of the HEFs. A representative Rietveld refinement result of the most complex HEF7 is presented in Figure 4- 1b. single phase rutile structure is confirmed with lattice parameters values, a = b = 0.47134(0) nm, c = 0.31725(9) nm and average crystallite sizes of 8.7(5) nm [162,163]. Table 4- 2 and Table 4- 3 present the structural parameters of all binary fluorides and all HEF samples obtained from Rietveld analysis. For more understanding of the phase purity of HEF based materials, logarithmic intensity vs. 2 θ patterns are given in Figure 4- 1. Figure 4- 1 c indicates that all materials show a single-phase rutile structure, the Miller indices hkl are labeled at the top diffractogram of HEF7. Since differently sized ions are incorporated into one lattice site, the shift of the (110) reflection, as shown in Figure 4- 1d, can be explained as follows. In MEF4 an average metal ion radius of 0.74 Å is calculated based on the assumption of equimolar proportions of the metal ions and the ionic radius values given by Shannon [164]. Additionally, the high-spin configuration of the metal ions (where applicable) was assumed, since F^- as ligand leads to only a small splitting (weak ligand in the spectrochemical series for octahedrally coordinated ions) of the d-orbitals into t_{2g} and e_g states, therefore favoring high-spin configuration of the ions. Incorporating Mn^{2+} (HEF5_Mn, Mn^{2+} ion radius 0.83 Å) leads to the expansion of the MEF4 unit cell, indicated by the reduced 2θ value. For MEF4, the average metal ion radius is 0.74 Å, and adding another metal ion such as Zn^{2+} which also has similar ionic radius of 0.74 Å, no significant shifts were observed for the XRD patterns. When Mn^{2+} is replaced by Zn^{2+} (HEF5_Zn, radius Zn^{2+} 0.74 Å), a larger unit cell of HEF5_Zn than MEF4 but a smaller unit cell than HEF5_Mn is expected, but the XRD reflections show similar unit cell sizes as for HEF5_Mn. Zn^{2+} seem to widen the unit cell more than expected, since adding both Mn^{2+} and Zn^{2+} in HEF6 leads to

a further increased unit cell volume compared to the HEF5 compounds. Adding the smaller Mg^{2+} (HEF7, radius Mg^{2+} 0.72 Å) reduces the size of the unit cell again, as shown in the respective pattern.

Table 4- 2: Crystal structure, cation coordination number and cation radius of the precursor binary fluorides

Binary Fluorides	**Crystal structure**	**Lattice constant (nm)**	**Ionic radius, with/without spin config. (Å)**	**References**
CuF_2	Monoclinic	a=0.32973; b=0.45624; c=0.46157	0.77	ICSD#71833
NiF_2	Rutile	a=b=0.46498 c=0.30838	0.63	ICSD#9168
FeF_2	Rutile	a=b=0.46945; c=0.33097	0.78(H), 0.61(L)	ICSD#9166
CoF_2	Rutile	a=b=0.46941; c=0.31698	0.745(H), 0.65(L)	ICSD#9167
ZnF_2	Rutile	a=b=0.47048; c=0.31338	0.74	ICSD#9169
MnF_2	Rutile	a= b= 0.4877; c=0.3311	0.83(H), 0.67(L)	ICSD#9165
MgF_2	Rutile	a=b=0.4621; c=0.30519	0.72	ICSD#397
HEF7	Rutile	a=b=0.47134; c=0.31726	-	Calculated (TOPAS)

*L= low spin, H= high spin, adapted from [164]

Table 4- 3: Refined structural parameters a, b, c, and V for HEF compounds from Rietveld analysis. The quality of refinements Rwp, Rp and GOF are also listed. Rietveld analysis was carried out using reference reflexes from ZnF_2 (ICSD#9169) thereby modifying the type of elements present in refined system and it indicated that all HEF samples possess rutile structure. This finding signified that the complex HEF system followed ideal rule of mixing, wherein equal probability of occupation was found in a random solid solution enviroment.

Parameters	**HEF7**	**HEF6**	**HEF5_Mn**	**HEF5_Zn**	**MEF4**
a [Å]	4.71342	4.7288	4.6826	4.7173	4.6911
b [Å]	4.71342	4.7288	4.6826	4.7173	4.6911
c [Å]	3.17260	3.1823	3.1708	3.2089	3.1699
V [Å3]	70.4834	71.1571	69.5261	71.4082	69.7580
Rwp	0.78	1.10	0.73	0.79	1.19
Rp	0.73	0.87	0.63	0.63	0.92
GOF	1.25	1.23	1.14	1.14	1.59

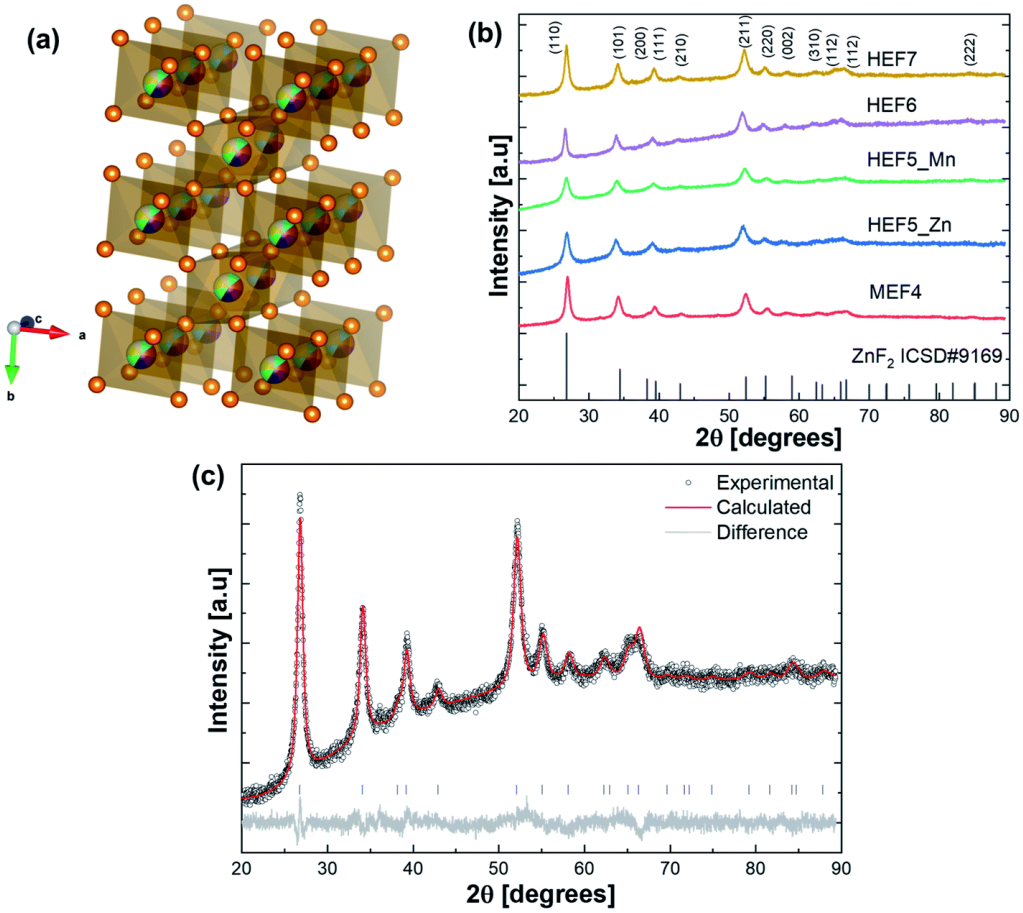

Figure 4- 1: (a) Representative structural model of pristine HEF7 nanoparticles. The colored balls are corresponding to the positions of the different metals, the orange balls correspond to F, (b) Rietveld refinement of the XRD pattern of HEF7 confirming its phase purity, (c) XRD patterns of 4, 5, 6, 7 cations containing MEF and HEF samples and d) magnified XRD pattern with a dotted line denoting the shift due to multiple cation incorporation in the crystal lattice.

4.3.2. Transmission electron microscopy

Transmission electron microscopy (TEM) analysis was carried out using HEF7 as an example, since it contains the highest number of different cations. The morphology of the as-synthesized HEF7 indicated very fine polycrystalline nanoparticles with crystallite sizes around 10 nm. This is in accordance with the Rietveld results. The sizes of the particles, composed of many crystallites, range up to hundreds of nm. The inset in Figure 4- 2a shows the results of selected-area electron diffraction (SAED) taken on a small area at the edge of a HEF7 nanoparticle. The nanoparticles possess high crystallinity with rutile-structure and the SAED annular pattern confirms that the material is obtained without any secondary phases or impurities. Figure 4- 2b illustrates a high-resolution TEM micrograph of the lattice planes from HEF7, with a d-spacing corresponding to the 110 planes (as confirmed from the XRD pattern).

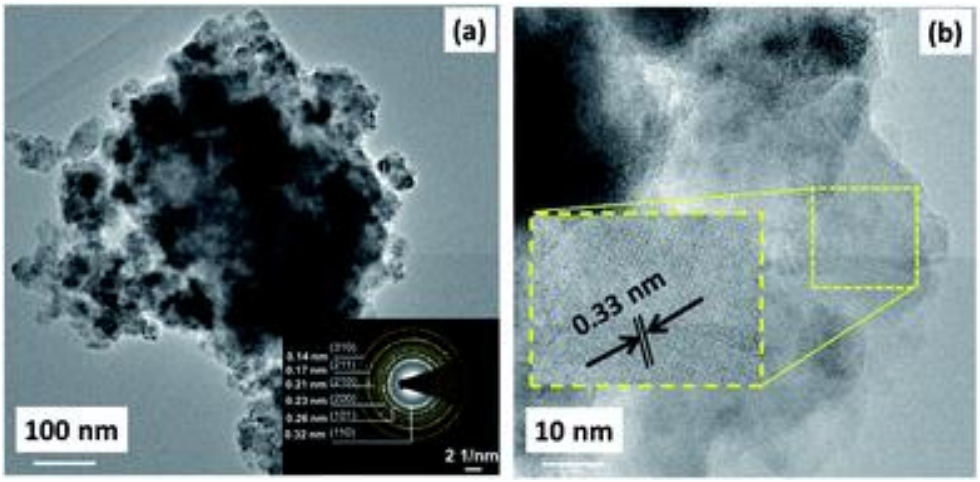

Figure 4- 2: (a) TEM micrograph of HEF7 and as inset the corresponding SAED pattern. These SAED indices comply with ZnF_2 ($P42/mnm$, 136) (b) HR-TEM image showing lattice planes (with inset depicting a magnified area) with a d-spacing value corresponding to the (110) plane.

Figure 4- 3 shows the results from energy-dispersive X-ray spectroscopy (EDX) analysis of HEF7 nano-powders. The mapping indicates a solid solution with all 7 metallic cations and fluorine being homogeneously distributed at the nanometer scale. The homogeneous elemental distribution in EDX mapping, the TEM and the XRD results indicate that the synthesized powders were single-phase solid solution materials. The stoichiometry of all the fluoride based compounds with chemical formula MF_2 were calculated based on ICP-OES results (Figure 4- 4). The elemental mapping spectrum of HEF7 showing the uniform distribution of metals is given in Figure 4- 5.

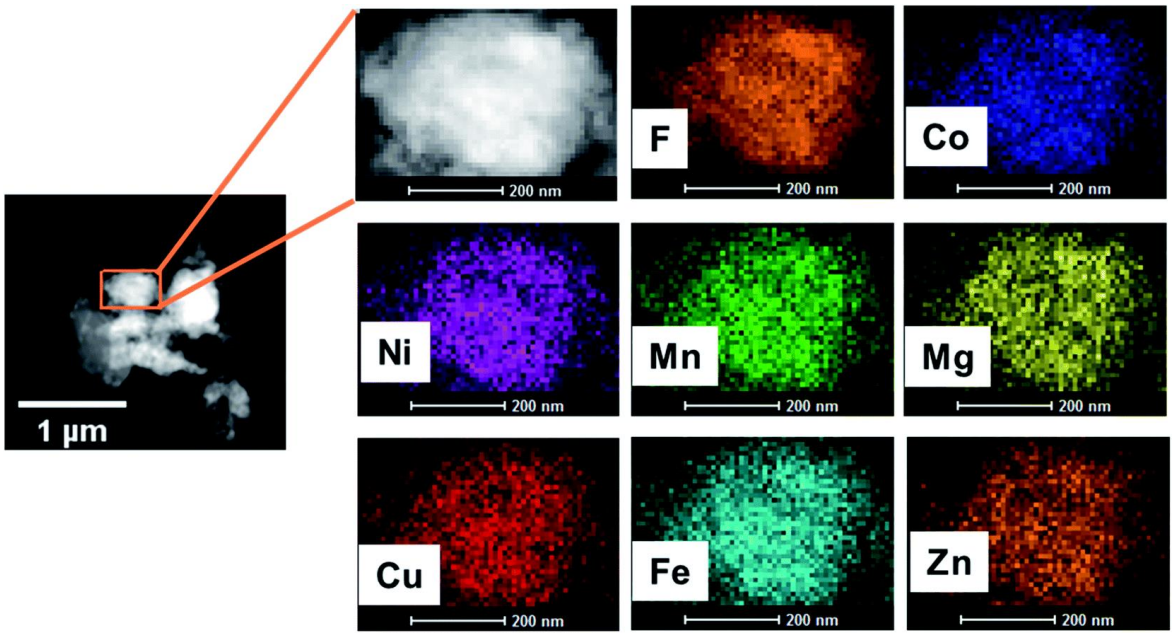

Figure 4- 3: STEM-based elemental maps of HEF7, showing homogenous distribution.

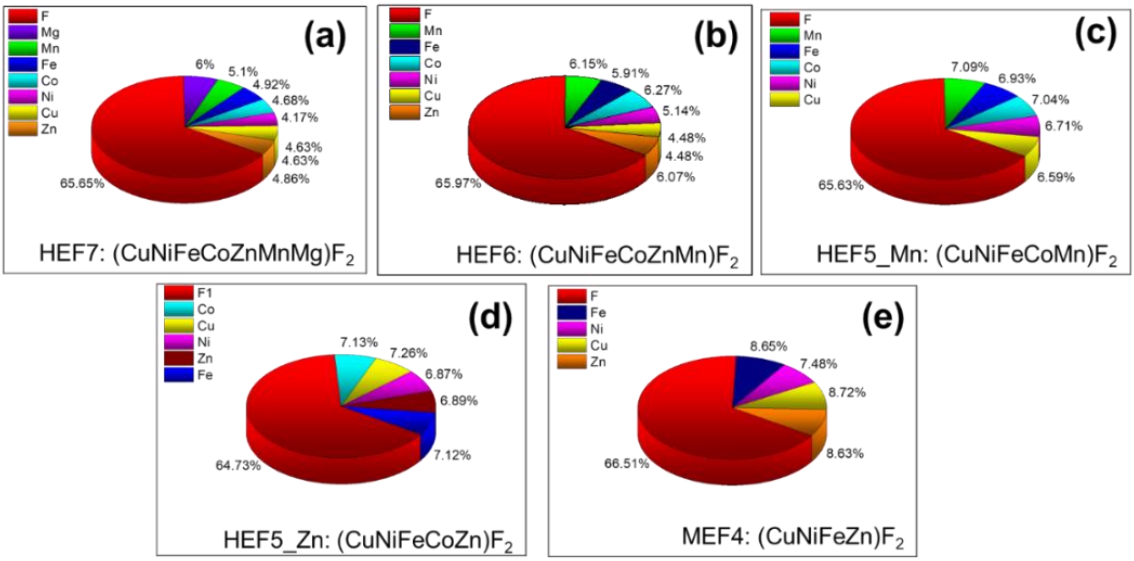

Figure 4- 4: (a) to (e) Inductively coupled plasma-optical emission spectroscopy (ICP-OES) results of MEF and HEF.

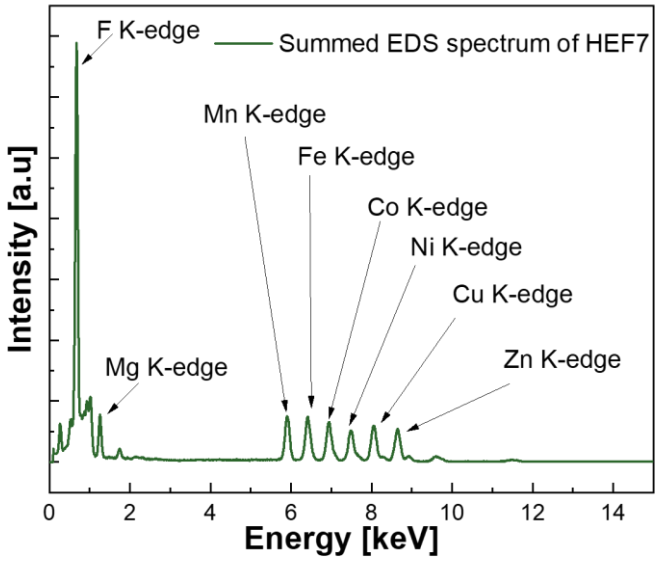

Figure 4- 5: STEM based EDX spectrum of the as-prepared HEF7 sample. All the constituent elements in HEF7 sample are detected.

4.3.3. Mössbauer spectroscopy

In order to further confirm the solid solution state of HEF7, ^{57}Fe Mössbauer Spectroscopy (MS) investigation was carried out to identify the chemical environment and the oxidation state of Fe in HEF7. Figure 4- 6 shows the Mössbauer spectrum of HEF7. The spectrum was fitted using two quadrupole doublets sub-spectra, both corresponding to Fe^{2+} environments (doublet I and II) with nearly identical isomer shifts (IS, I = 1.34 mm/s, II = 1.30 mm/s) but distinct quadrupole splits (QS, I = 2.67 mm/s, II = 1.96 mm/s). In addition, a small fraction of Fe^{3+} was evident (IS = 0.40

mm/s, QS = 0.48 mm/s). The quantification, based on the relative area fraction, yielded the values of Fe^{3+}, Fe^{2+} (doublet I) and Fe^{2+} (doublet II) as 19 %, 50 % and 31 %, respectively. However, this result is in contrast to the other obtained results from SAED, XRD, TEM elemental mapping, since it suggests a different chemical environment and even a mixed-valence state of the incorporated Fe. Nevertheless, this seemingly contrasting finding is coherent with the conclusions drawn from the Mössbauer studies of FeF_2 nanoparticles, reported by Ramasamy S. et al. They reported a similar finding, wherein MS peak splitting arose from local defects due to a large amount of grain boundaries [160]. Additionally, they referred to a slightly different Fe-F bond stretching at the surface (due to minor topological hydration), which could lead to a different chemical environment and therefore requires different fitting parameters than bulk FeF_2. Hence, we presume that the origin of broadening in MS spectrum HEF7 might be due to the ball milling procedure and the vast amount of local defects and grain boundaries formed during this procedure [165].

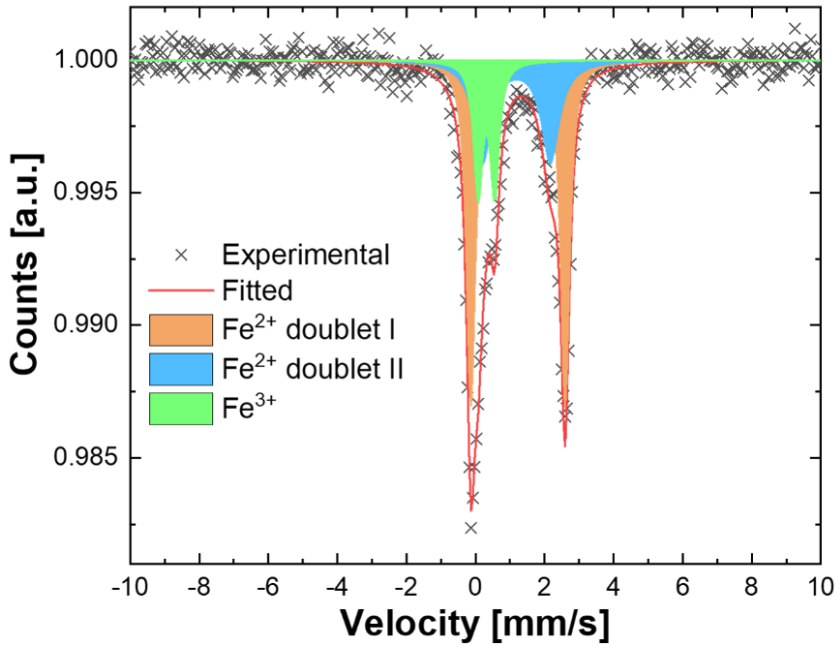

Figure 4- 6: Mössbauer spectra of pristine HEF7 nanoparticles showing two different oxidation states and two different chemical environments.

4.3.4. Electron energy loss spectroscopy

To elucidate the presence of $Fe^{2+/3+}$ at the surface of the particles, electron energy loss spectroscopy (EELS) mapping was performed on the particle edges to identify the oxidation states of Fe, Co, Ni, Cu and Mn. Zn and Mg were assumed to be in the 2+ oxidation state. The sample was transported in a vacuum transfer TEM holder to exclude oxidation. Figure 4- 7 shows the EELS investigation of HEF7 with five different areas on the edges of different particles being measured.

Co, Cu, and Ni could only be found in the 2+ state and did not show any indications that point towards a mixture of different valence states. Figure 4- 7a shows the L3 and L2 edges of Mn, exhibiting a maximum peak shift between the different areas of about 0.6 eV. The L3/L2 ratio shows some minor differences between the areas, but the ratios for Mn^{3+} and Mn^{4+} would be much lower, so Mn in 3+ and 4+ state can be excluded (see Figure 4- 8)). Therefore, the Mn state in all areas is measured to be around 2+. The Fe L3 and L2 edge positions are displayed in Figure 4- 7. Two different L3 edges are detected, which can be indexed into Fe^{2+} and Fe^{3+} as indicated by Mössbauer spectroscopy results (more details in Figure 4- 8b). Different measured areas show different valence states, which implies that an inhomogeneous change in the oxidation state takes place. We attribute this to the local defects resulting from ball-milling, as explained in the Mössbauer section of this article. Figure 4- 7c shows one of the measured areas and an EELS mapping, depicting that Fe^{2+} and Fe^{3+} appear mixed, and not separated into areas with only Fe^{2+} or Fe^{3+}. However, it should be noted that no secondary phases were observed, either from XRD or HR-TEM, which indicates that these differences in the charge states are intrinsic features of single phase HEF7.

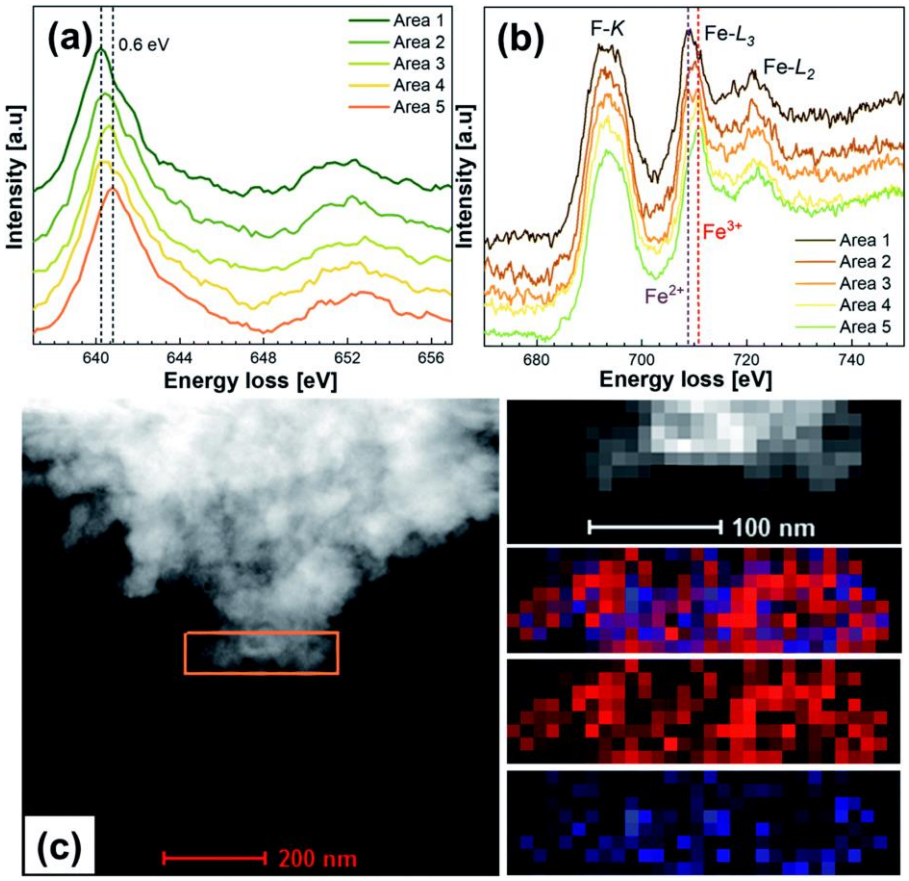

Figure 4- 7: Valence state characterization of HEF7. EELS spectra of (a) Mn L2,3 edge (b) Fe L2,3 edge (c) EELS mapping results on the marked area denoting the presence of Fe^{2+} (red) and Fe^{3+} (blue).

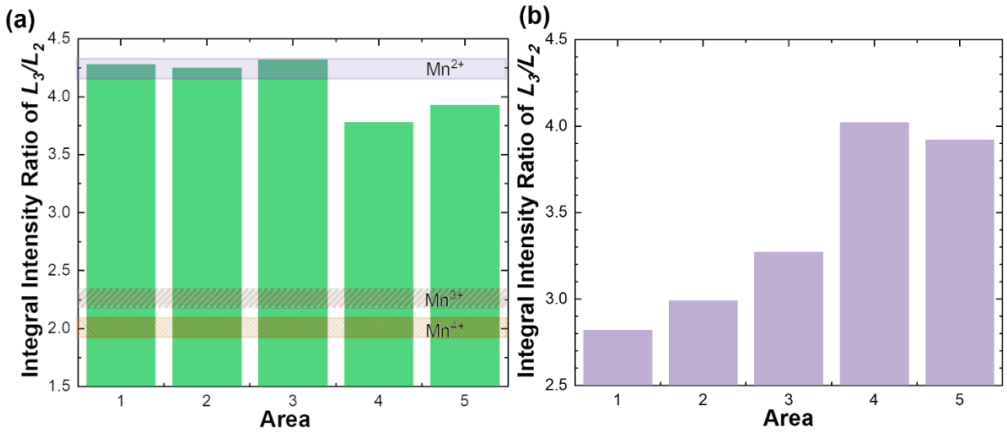

Figure 4- 8: Plots of the intensity ratios of L3/L2 values of (a) Mn (values in green colour) and (b) Fe (values in purple colour) calculated from the spectra obtained from HEF7 nanoparticleas a function of the areal mapping values acquired at different points.

4.3.5. X-ray photoelectron spectroscopy

Further, the surface chemical state of the HEF7 sample was probed with X-ray photoelectron spectroscopy (XPS). The relevant spectra of the constituent elements are shown in Figure 4- 9 and the corresponding reference spectra in Figure 4- 10, Figure 4- 11, Figure 4- 12, Figure 4- 13, Figure 4- 14, Figure 4- 15, Figure 4- 16, Figure 4- 17 and Figure 4- 18. The survey spectrum showing the overview of constituents in HEF7 (binding energy range of 0–1100 eV) is given in Figure 4- 19.

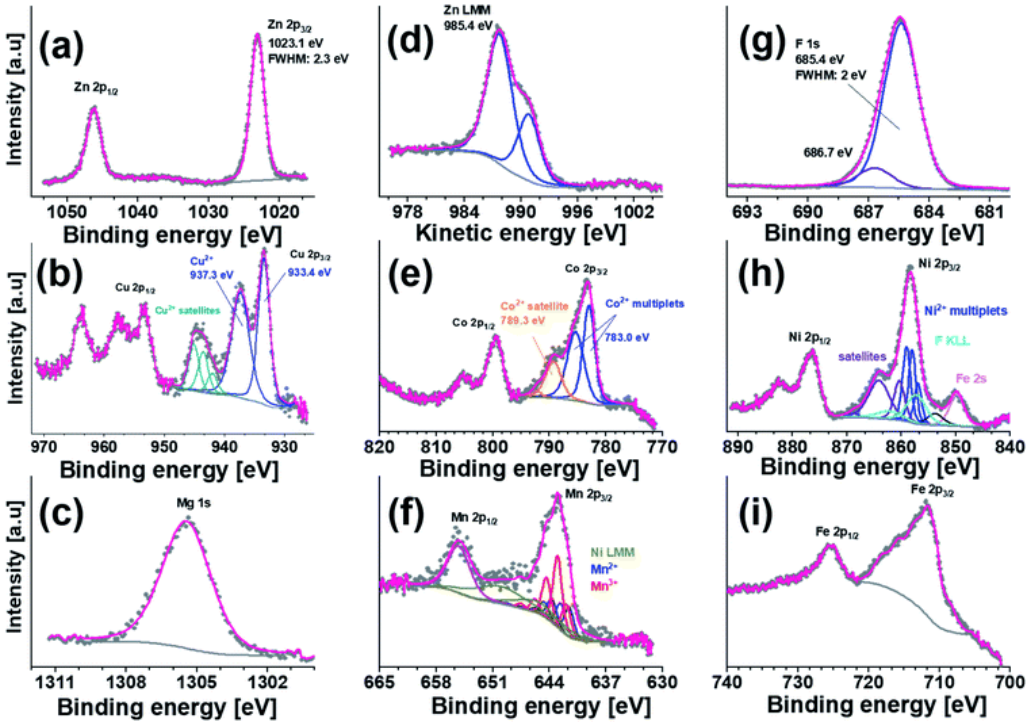

Figure 4- 9: XPS spectra of (a) Zn 2*p*, (b) Cu 2*p*, (c) Mg 1*s* (d) Zn Auger LMM kinetic energy spectra, (e) Co 2*p*, (f) Mn 2*p*, (g) F 1*s*, (h) Ni 2*p* and (i) Fe 2*p* of HEF7 nanoparticles.

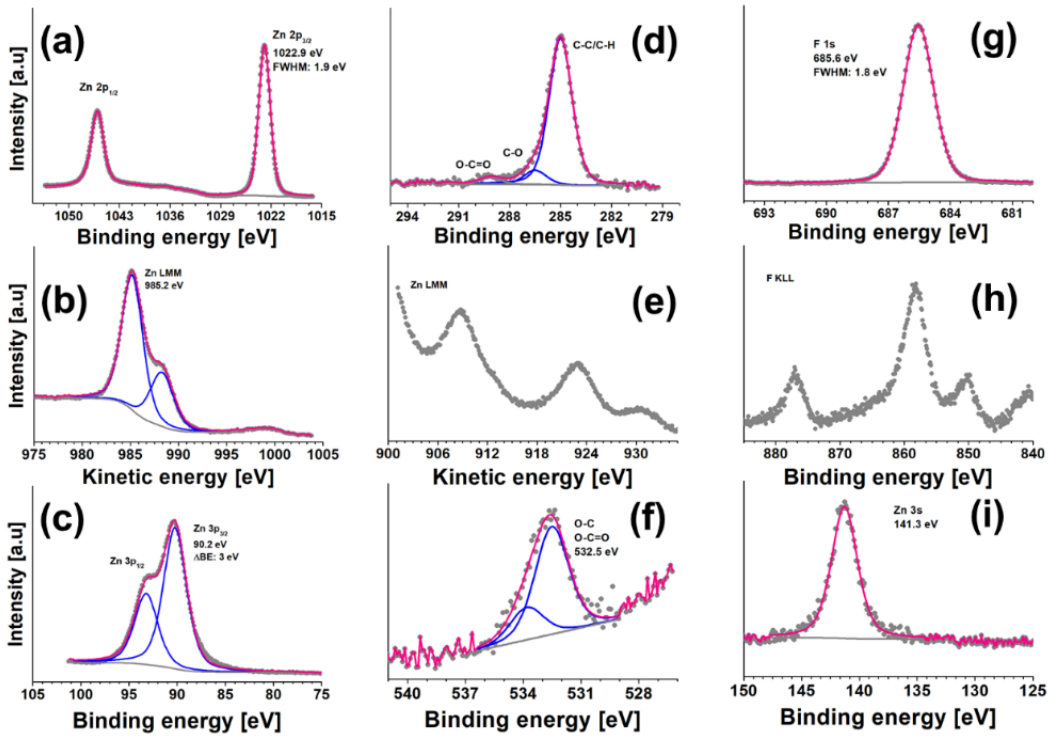

Figure 4- 10: (a) Zn 2*p*, (b) Zn LMM, (c) Zn 3*p*, (d) C 1*s*, (e) Zn LMM, (f) O 1*s*, (g) F 1*s*, (h) F KLL, and (i) Zn 3*s* XPS spectra of ZnF_2 powder.

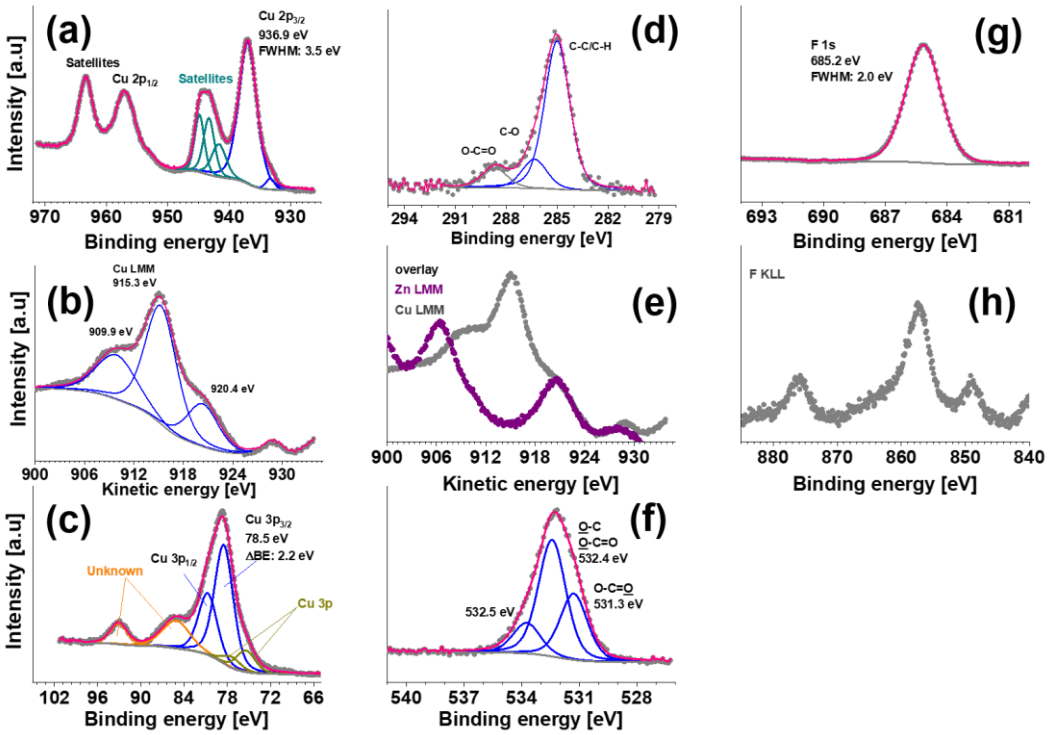

Figure 4- 11: (a) Cu 2*p*, (b) Cu Auger LMM kinetic energy spectra, (c) Cu 3*p*, (d) C 1*s*, (e) overlay plot of Zn LMM and Cu LMM kinetic energy spectra (f) O 1*s* (g) F 1s and (h) F KLL, XPS spectra of CuF_2 powder (In pure CuF_2 powder, the Cu 2*p*3/2 spectrum has a pronounced peak at 936.9 eV with FWHM of 3.5 eV).

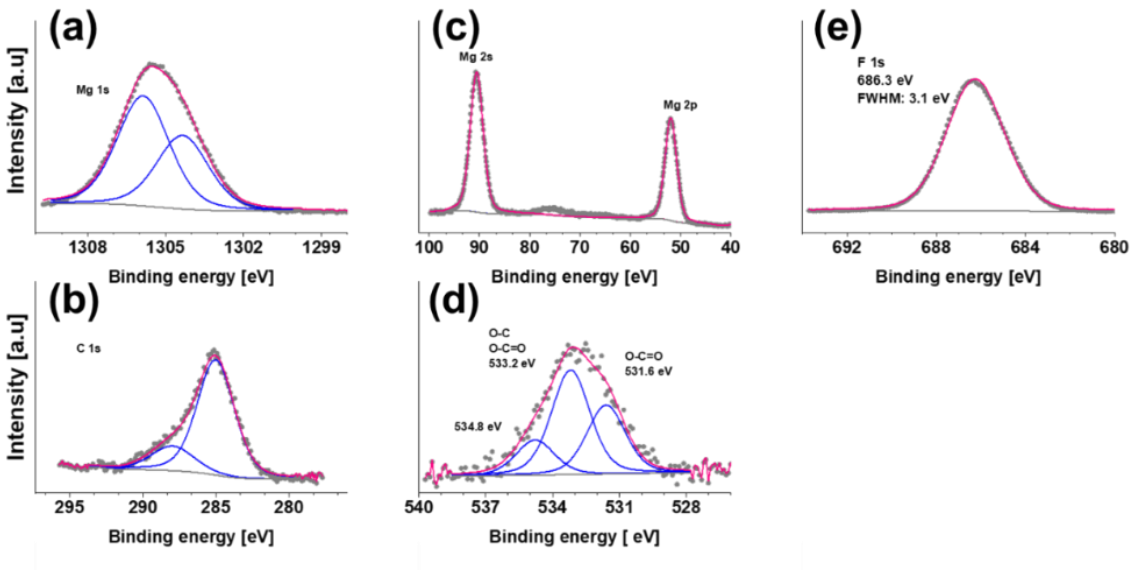

Figure 4- 12: (a) Mg 1*s*, (b) C 1*s*, (c) Mg 2*p*, Mg 2*s*, (d) O 1*s* and (e) F 1s, spectra of MgF_2. The broadening of C 1*s* and Mg 1*s* spectra is because of difficulties of charge compensation.

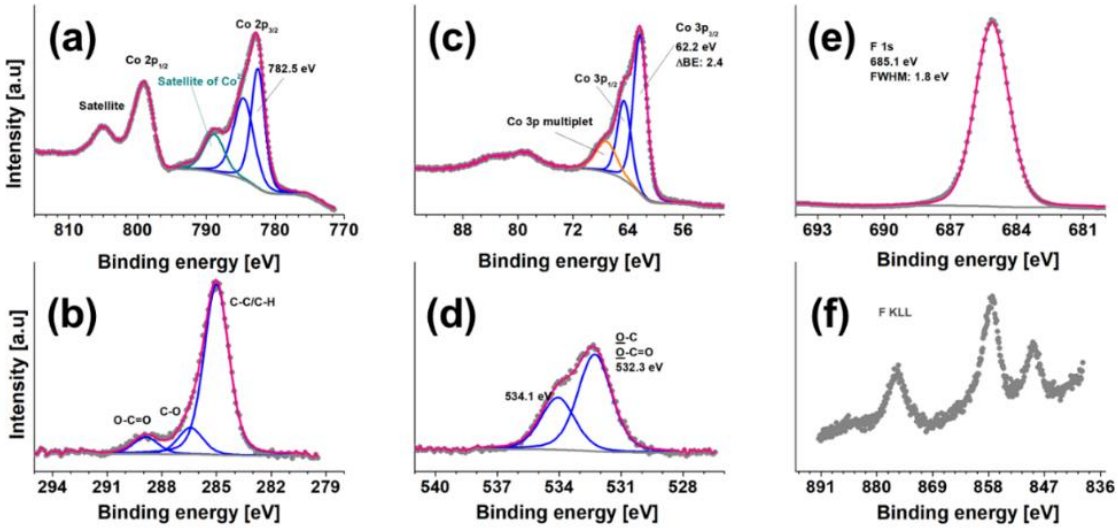

Figure 4- 13: (a) Co 2*p*, (b) C 1*s*, (c) Co 3*p*, (d) O 1*s* (e) F 1*s*, and (f) F KLL XPS spectra of CoF_2 powder.

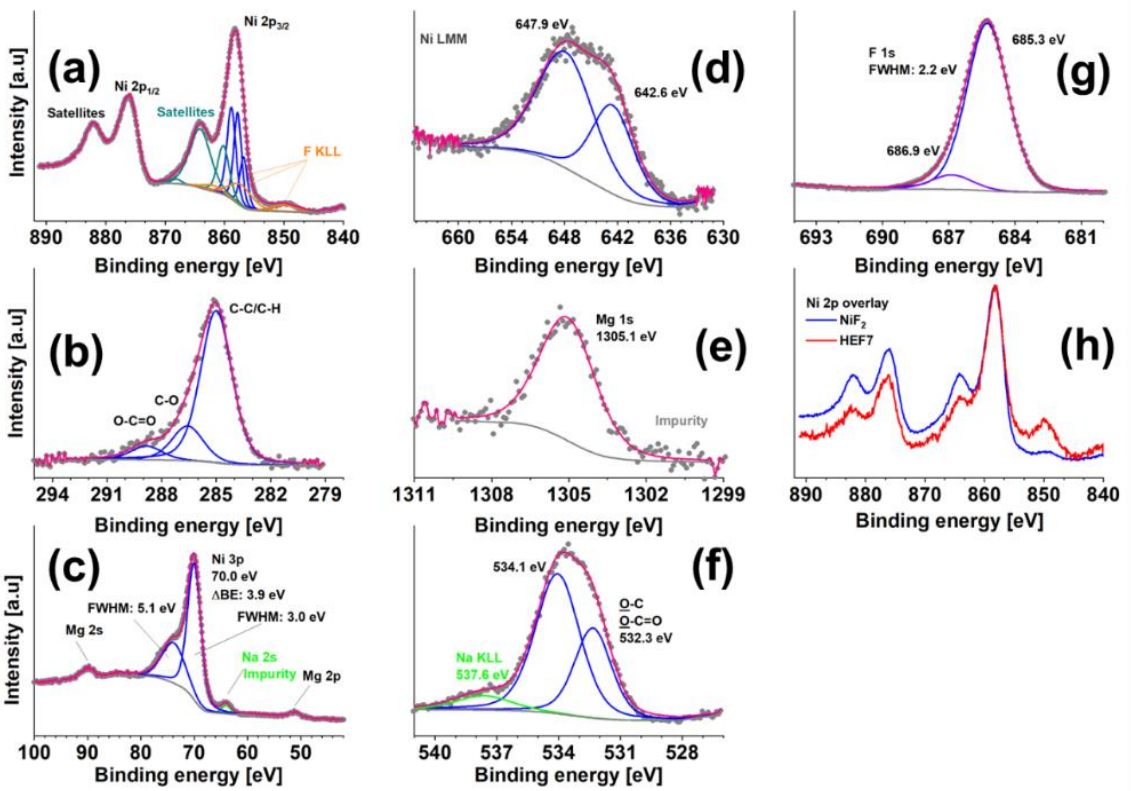

Figure 4- 14: (a) Ni 2*p*, (b) C 1*s*, (c) Ni 3*p* (Mg 1*s*, Na 2*s* as impurity), (d) Ni LMM, (e) Mg 1*s*, (f) O 1*s*, (g) F 1*s* XPS spectra of NiF_2 powder and (h) overlay data of NiF_2 power (with HEF7)

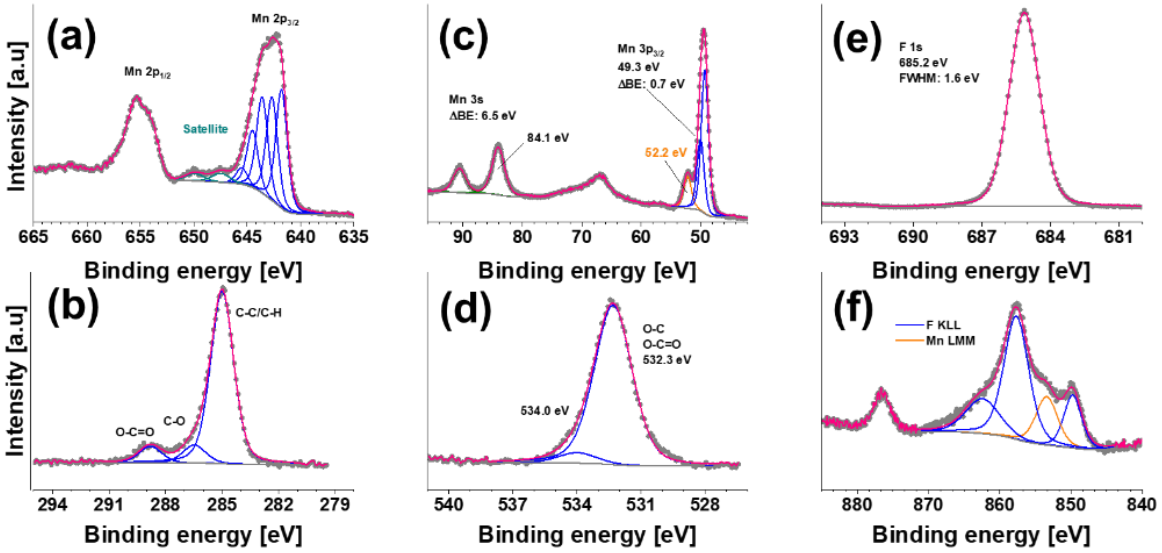

Figure 4- 15: (a) Mn 2*p*, (b) C 1*s* (c) Mn 3*p*, Mn 3*s*, (d) O 1*s* (e) F 1*s* and (f) F KLL XPS spectra of MnF_2 powder.

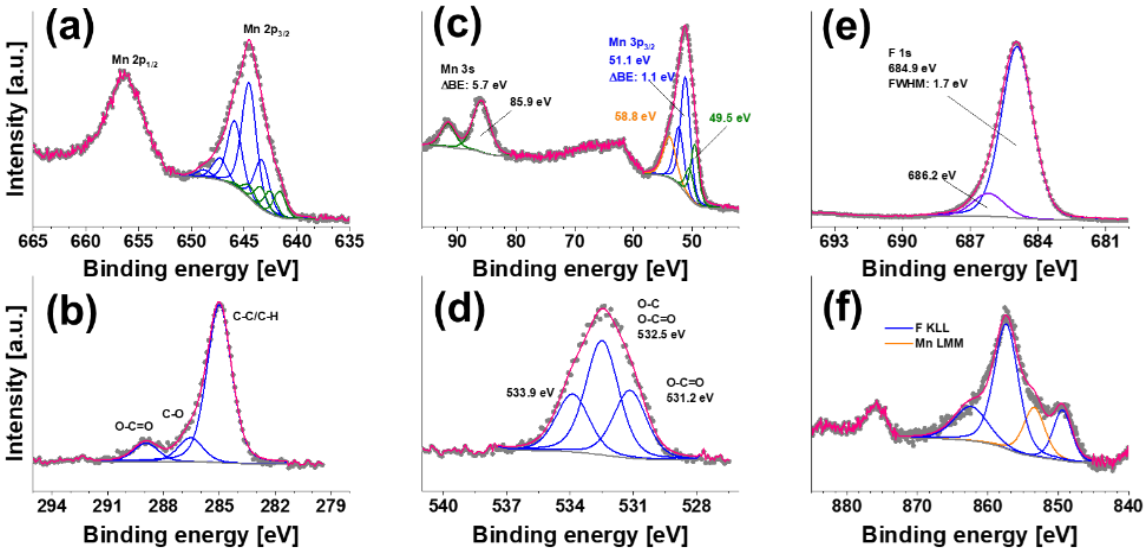

Figure 4- 16: (a) Mn 2*p*, (b) C 1*s* (c) Mn 3*p*, Mn 3*s*, (d) O 1*s* (e) F 1*s* and (f) F KLL XPS spectra of MnF_3 powder.

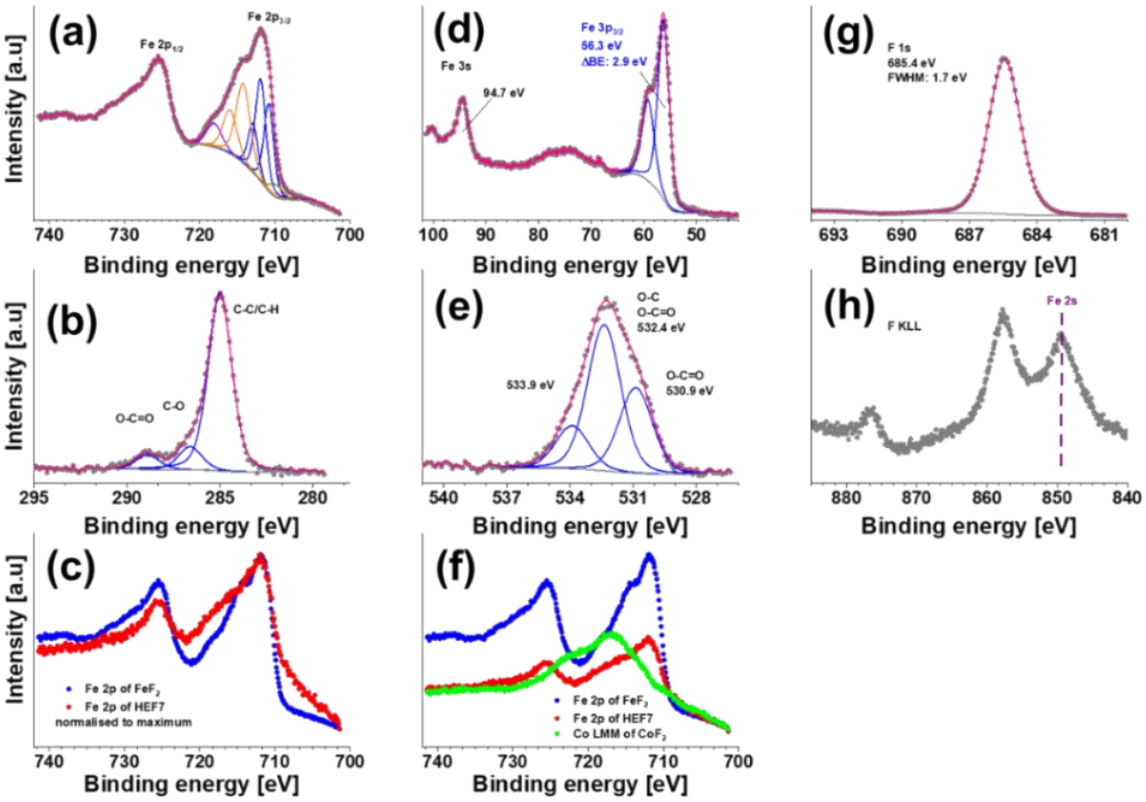

Figure 4- 17: (a) Fe 2*p*, (b) C 1*s*, (c) overlay comparison of FeF_2, HEF7 (d) Fe 3*p*, Fe 3*s* (e) O 1*s*, (f) overlay comparison of FeF_2, HEF7, Co LMM of CoF_2 , (g) F 1*s* and h) F KLL XPS spectra of FeF_2 powder.

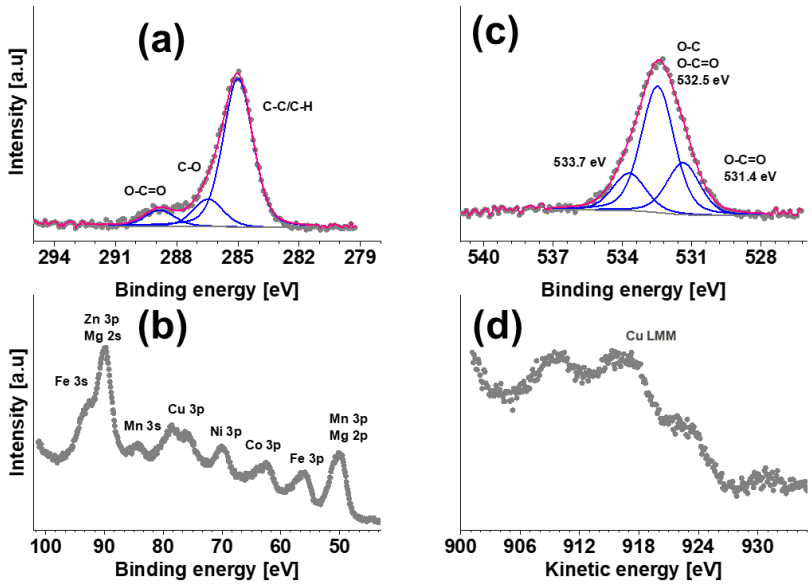

Figure 4- 18: (a) C 1*s*, (b) overlapping spectra hamper evaluation of Mn 3p and Mn 3s for elucidation of Mn oxidation state (c) O 1*s* and d) Cu LMM XPS spectra of HEF7 nanoparticles.

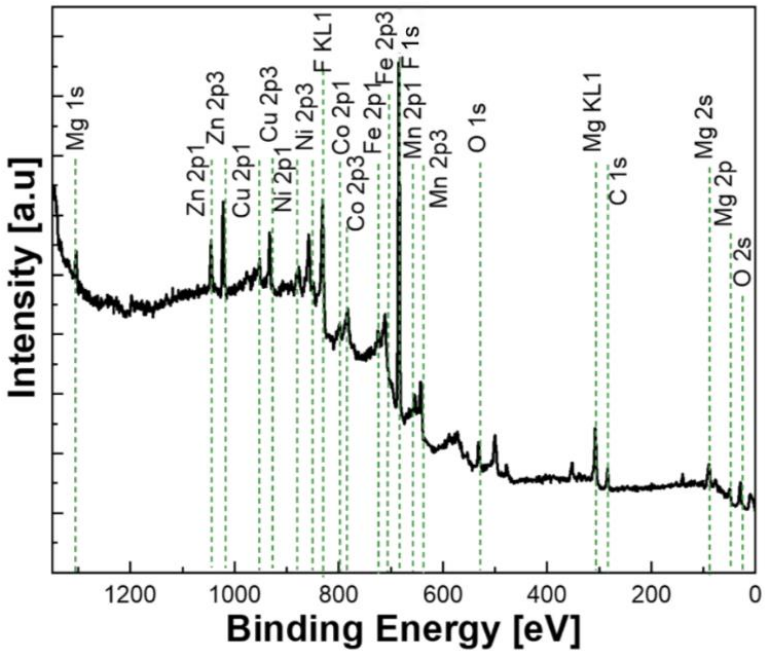

Figure 4- 19: Survey scan spectra of HEF7 nanoparticles.

In the Zn 2*p* spectrum (Figure 4- 9a), a single doublet with the 2*p*3/2 component at 1023.1 eV binding energy and the full width at half maximum (FWHM) intensity of 2.3 eV is observed. As determining the Zn oxidation state purely from the Zn 2*p* peak is difficult, the Zn LMM Auger line is also considered (see Figure 4- 9). The Zn LMM Auger line is observed at a kinetic energy of 985.4 eV and thus Zn can be attributed to the Zn^{2+} state [166]. This agrees with our measurements on pure ZnF_2 (see Figure 4- 10) as a reference that shows similar values as Zn 2*p*3/2 is identified at

1022.9 eV with a FWHM intensity of 1.9 eV and a Zn LMM line at 985.2 eV. In the Cu 2*p* region (Figure 4- 9b), Cu ions in HEF7 show very interesting spectra with 2 main peaks at 933.4 and 937.3 eV. The peak at 937.3 eV with FWHM intensity of 3.5 eV is analogous to Cu 2*p*3/2 of pure CuF_2 measurements shown in Figure 4- 11. Additionally, satellites of the Cu^{2+} state appear at 942.0-945 eV in the spectrum. However, the additional peak at 933.4 eV (FWHM: 2.3 eV) in the Cu 2*p*3/2 spectrum of HEF7 could be attributed to a reduced state of Cu ions or possibly CuO or $Cu(OH)_2$ state. [167]. According to this peak assignment, the majority of Cu ions at the surface of HEF7 (64% of total Cu ions) are attributed to Cu^{2+} [167]. In Figure 4- 9c, Mg 1s peak in the HEF7 sample is successfully assigned to Mg^{2+} ions in Mg-F bonding at 1305.4 eV with FWHM intensity of 2.5 eV [168][169] (pure MgF_2 XPS spectrum is given in Figure 4- 12). The Co 2*p* spectrum Figure 4- 9e) of HEF7 shows one doublet with multiplet structure and a characteristic satellite. The main peak position at 783 eV as well as the satellites at 6.3 eV higher than the main peak indicate that the Co ions in HEF7 appear as Co^{2+} in a Co-F bonding situation. Additionally, the fitting parameters of the HEF7 match with the pure CoF_2 as presented in Figure 4- 13. In the Mn 2*p* spectra of Figure 4- 9, a broad doublet can be observed. The Mn 2*p*3/2 peak can be fitted with two sets of multiplets and including the overlapping Ni LMM Auger peaks that indicates approximately 60% Mn^{3+} and 40% Mn^{2+} on the surface of HEF7. The multiple sets of Mn^{2+} and Mn^{3+} are taken from the MnF_2 and MnF_3 reference measurements shown in Figure 4- 15 and Figure 4- 16, respectively. The majority of F ions (Figure 4- 9g) at 685.4 eV with a FWHM of 2 eV are attributed to the F ions in the crystal structure and have a binding energy similar to the binary fluorides. The low-intensity peak 686.7 eV might probably occur through the ball milling process by forming C-F contaminations on the surface [170]. To interpret the Ni 2*p*3/2 spectrum (Figure 4- 9h) in HEF7, it is compared to the Ni 2*p*3/2 spectrum of pure NiF_2 powder sample. The overlap of the Ni LMM and Fe LMM line on Co 2*p* spectra is ignored, because of the low intensity of the Auger peaks. The peak overlay in Figure 4- 14 shows a similar binding energy and FWHM intensity of the main peak. Therefore, the Ni 2*p*3/2 spectrum of HEF7 was fitted with the multiplet parameters of Ni 2*p*3/2 in NiF_2 and can be attributed to Ni^{2+} state. However with this method the existence of a minor contribution of Ni^{3+} ions cannot be fully excluded, since the binding energies of Ni^{2+} and Ni^{3+} ions are very close to each other, at least in oxide samples [171–175]. In the peak fitting of the Ni spectrum, overlapping F KLL, Mn LMM, and Fe 2*s* peaks are taken into consideration. Identification of the chemical state of Fe ions in HEF7 using XPS is challenging. In the HEF7, the Fe 2*p* Figure 4- 9i) overlaps with low intensity F plasmons and the Co LMM Auger line. Both aspects increase the background intensity and hamper reliable peak and background positioning. Furthermore, the overlapping Co Auger line hinders direct comparison to the FeF_2 reference. Therefore, oxidation state analysis of the Fe ions in HEF7 from XPS was not possible. In summary, XPS confirms that Mg, Zn, and Co ions are

present in the 2+ state, even at the outmost surface of the HEF particles. For Cu and Mn, mixed valence states were found at the surface, including around 64% of Cu ions and 40% of Mn ions in the 2+ state. Also, the majority of Ni ions can be considered as Ni^{2+}. The Fe oxidation state could not be analyzed from XPS because of intense peak overlap. We assume that the discrepancy between XPS and EELS results regarding the oxidation state of Cu and Mn, is surface related, since EELS pertains to the bulk material while XPS only to the surface. The indications that a different surface state compared to the bulk material is apparent, was as well indicated by MS measurements and most probably an effect of the ball milling procedure.

4.4 Conclusion

Multicomponent rutile (*P*42/*mnm*) structured fluorides, containing 4 to 7 transition metals (Co, Cu, Mg, Ni, Zn, Mn, Fe) in equiatomic ratios, were synthesized using a simple mechanochemical approach. Based on the combined investigations from XRD, ICP-OES, TEM, and EDX-EELS studies, it is shown that all pristine HEF samples crystallized in a phase-pure rutile structure with the presence of agglomerated fine nanoparticles. The local structure of the HEF compounds was probed by XPS. The local structural disorder of the HEF compounds arose due to the synthesis process and the resulting variation in the oxidation states of Fe was detected utilizing Mössbauer spectroscopy. These high entropy fluorides represent an additional class of high entropy ceramics, which have recently attracted attention especially due to the development of high entropy oxides. With the introduction of the novel high entropy fluorides, similar interest could be generated due to the variety of different applications for fluoride materials and the improvements the high entropy concept might bring.

Chapter 5

5. High entropy fluorides as conversion cathodes with tailorable electrochemical performance

The work in the following chapter was published in Journal of Energy Chemistry [180].

5.1. Introduction

With rapidly increasing demands for portable electronics and electric vehicles, the development of secondary lithium-ion batteries (LIBs) with high energy densities is necessary. In current LIB technology, the cell voltage and capacity are largely determined by the cathode material, which also dominates the battery cost. Therefore, it is important to explore alternative cathode materials and to investigate their structure/composition/performance relationships for further development [181]. As an example, conversion-based electrode materials, which serve a potentially higher specific capacity than conventional intercalation-based electrode materials, have drawn great attention in recent years [61]. Since in a conversion reaction, multiple electrons ($n \geq 2$) can be transferred per formula unit during the redox reaction, conversion materials can deliver capacities three to five times larger compared to intercalation materials [17]. Among the different conversion material types, metal fluorides (MFs) show a relatively high lithiation potential due to the large formation enthalpy [182–184]. Additionally, MFs show high volumetric and gravimetric capacities, which enable them to be attractive candidates for high energy density cathode materials [66,185].

Unfortunately, conversion materials suffer from large volume changes upon cycling and unfavorable interactions between the active material and the electrolyte [68]. The former can lead to cracking of individual particles, structural disintegration, swelling of the electrode, and disconnection of the active material. The latter is accompanied by a loss of active material, re-precipitation of cathode components which can lead to blockage of the ion pathways, and migration of soluble species to the anode side which can negatively affect the SEI (blockage of the

anode) [186,187]. In addition, electrolyte decomposition can also occur (gas evolution), which is a relevant factor from a safety point of view. Overall, these interrelated processes may lead to an increase in cell resistance, poor cycling performance, and poor Coulombic efficiency [61,188,189]. In order to circumvent these issues and to realize the application of MFs in rechargeable batteries, cation or anion doping is an important strategy to improve the electrochemical properties of MFs, and promising progress has been achieved [185,190–193]. Wang et al. proposed the incorporation of Cu into the FeF_2 crystal lattice by preparing a ternary fluoride of $Cu_{0.5}Fe_{0.5}F_2$. This material exhibits a voltage hysteresis of less than 150 mV with a low cycling rate, achieving high capacity [17]. Following the concept of "ternary fluorides", Gordon et al. successfully synthesized solid solution fluorides including $Ni_yFe_{1-y}F_2$, $Co_yFe_{1-y}F_2$, and $Mn_yFe_{1-y}F_2$, demonstrating that the metal composition determines the formation and growth of the cathode solid electrolyte interphase (CEI) affecting the cathode stability [194]. Later, Villa et al. found that with the substitution of Cu into NiF_2, both, the volumetric expansion during the first lithiation and the fluorine loss during delithiation, are reduced, and thus the cycling performance was improved [195]. These reports show the synergistic effect of metals in the ternary fluorides, which is beneficial for the electrochemical performance of MFs-based cathode materials. In general, the synergistic effect of metals can be found more pronounced and is further investigated in high entropy materials (HEMs).

Recently, the use of the high entropy concept to develop materials with tailorable properties is gaining great attention [101,102,196]. Considering the potential of MFs as high capacity cathodes, it is of great interest to explore the conversion mechanism based on high entropy fluorides (HEFs) that can be used as cathode materials for LIBs. As previously reported, HEFs were successfully synthesized and investigated for their electrocatalytic properties [197]. In the present work, we report a series of HEFs based materials namely: $(Cu_{1/5}Ni_{1/5}Fe_{1/5}Zn_{1/5}Co_{1/5})F_2$, $(Cu_{1/6}Ni_{1/6}Fe_{1/6}Zn_{1/6}Co_{1/6}Mn_{1/6})F_2$, and $(Cu_{1/7}Ni_{1/7}Fe_{1/7}Zn_{1/7}Co_{1/7}Mn_{1/7}Mg_{1/7})F_2$ as electrode materials for battery applications, in an attempt to exploit their high theoretical specific capacities. It is observed that instead of a step-by-step reduction to each individual metal, HEFs exhibit a single-step reaction process. Moreover, the addition or elimination of an element has a significant effect on the redox potentials while simultaneously reducing the voltage hysteresis during cycling. The electrochemical properties of HEFs show reversible lithium storage with high capacities. These findings offer new guidelines for material design and tailoring of electrochemical properties by deliberate selection of elements for high performance LIB cathode materials.

5.2. Materials synthesis and cell fabrication

HEF/ Multi-walled carbon nanotubes (MWCNT) was obtained by mechanochemical milling (6 h) with 15 wt.% MWCNT (Sigma Aldrich, 7.5% MWCNT basis, outer diameter of 7 to 15 nm, length 0.5 to 10 μm) and 85 wt.% HEF powder (active material). After the milling, HEF/MWCNT nanocomposites were collected in an Ar-filled glovebox. Electrodes were prepared by slurry coating of 80 wt.% cathode active material (HEF/MWCNT), 10 wt.% carbon black (C65), and 10 wt.% polyvinylidene fluoride (PVDF, Solef 5130, Solvay) in *N*-methyl-2-pyrrolidone onto aluminium foil. The electrodes were dried over night at 100 °C. All electrode tapes with an areal loading of around 0.5–1 mg/cm^2 were prepared in an Ar-filled glovebox to avoid exposure to air.

Electrochemical testing was done with CR2032 type coin cells. All cells were assembled inside an Ar-filled glovebox and comprised an HEF7 composite cathode, a GF/D glass microfiber separator (GE Healthcare Life Science, Whatman), and a lithium anode (China Energy Lithium Co., Ltd) of diameters 13 mm, respectively. LP57 [1 M $LiPF_6$ in 3:7 (w/w) mixture of ethylene carbonate (EC) and ethyl methyl carbonate (EMC)] was used as electrolyte.

5.3. Results and discussion

HEFs were synthesized by a mechanochemical method as in Chapter 4 [197], $(Cu_{1/5}Ni_{1/5}Fe_{1/5}Zn_{1/5}Co_{1/5})F_2$, $(Cu_{1/6}Ni_{1/6}Fe_{1/6}Zn_{1/6}Co_{1/6}Mn_{1/6})F_2$, and $(Cu_{1/7}Ni_{1/7}Fe_{1/7}Zn_{1/7}Co_{1/7}Mn_{1/7}Mg_{1/7})F_2$, marked as HEF5, HEF6, and HEF7, respectively, in the following sections. For comparison, medium entropy materials of $(Cu_{1/4}Ni_{1/4}Fe_{1/4}Zn_{1/4})F_2$ and $(Cu_{1/3}Ni_{1/3}Fe_{1/3})F_2$ (named as MEF4 and MEF3, respectively) were also synthesized. Figure 5- 1(a) shows the schematic illustration of the synthesis process utilized (further details are given in the Experimental Section). The S_{config} for each MEF and HEF is calculated according to Eq. 4 and presented in Table 4- 1. Typically, materials with S_{config} of greater than 1.5R can be considered as HEMs, lower than 1R as low entropy materials, and with S_{config} between 1R and 1.5R as medium entropy materials [114]. Due to the intrinsic low electronic conductivity of fluorides, the HEFs were further mixed with multi-walled carbon nano-tubes (MWCNT) and ball milled at 500 rpm for 3 h to obtain the HEF/MWCNT composites. Scanning electron microscopy (SEM) images of HEF powder and HEF/MWCNT composite are presented in Figure 5- 1. Figure 5- 1 (c) showing that powders are in nano to micrometer size range and intertwined with MWCNTs. As reference materials, all metal fluorides (MFs) were ball milled separately for 24 h and then mixed with MWCNT.

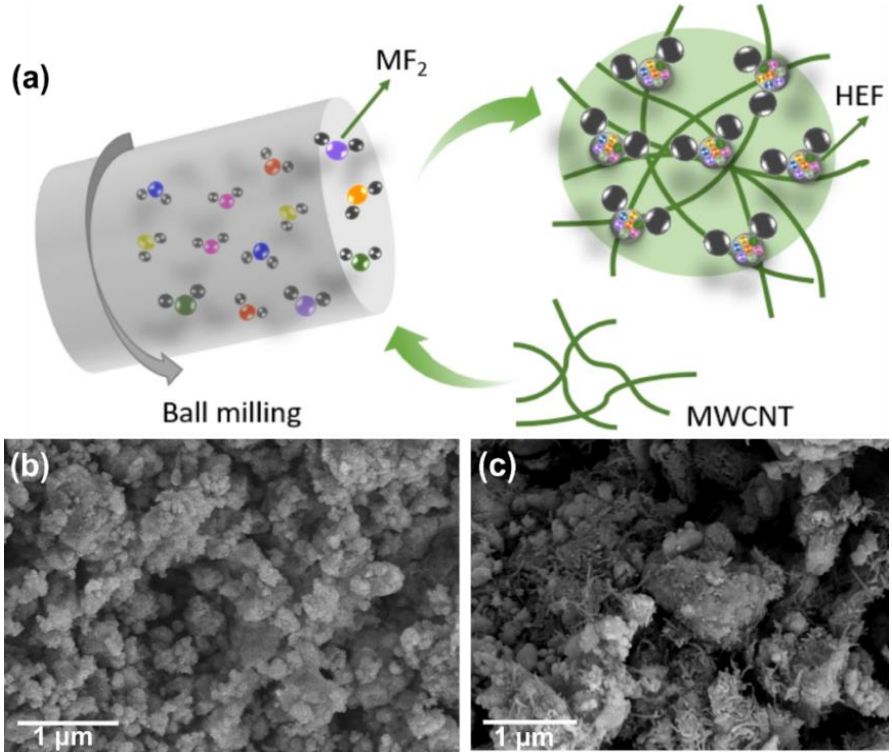

Figure 5- 1: (a) Schematic diagram of the synthesis processes for the HEF/MWCNT composites, where MF represents the binary fluorides of CuF_2, NiF_2, FeF_2, CoF_2, ZnF_2, MnF_2, and MgF_2 in equimolar ratio. Typical SEM images of (b) HEF powder and (c) HEF/MWCNT composite after 3 h of ball milling.

5.3.1. Electrochemical performance in lithium battery cells

To investigate the electrochemical redox potentials, cyclic voltammetry (CV) measurements were performed. In order to evaluate the electrochemical differences of high entropy compounds, where all elements are on the same lattice, to simple mixtures of MF compounds, a series of experiments were conducted. CV profiles of the HEF, MEF, mixture of all MFs, and each individual MF are given in Figure 5- 2 and Figure 5- 3. In the mixed fluorides system (Figure 5- 2f), several redox peaks were observed during the de/lithiation process, which indicates that the reactions for each fluoride compound tend to occur independently. However, the lithiation/delithiation processes for HEFs and MEFs show significant differences from that of mixed fluorides. Comparable lithiation behavior was observed in all HEFs and MEFs. For instance, during the first lithiation process, two reduction peaks at ~1.9 and 1.5 V could be observed for all materials (Figure 5- 2 a–e). The small peak at 1.5 V is probably related to the decomposition of electrolyte with the formation of the solid electrolyte interphase (SEI) layer [198]. In the subsequent lithiation processes, only one reduction peak was observed. In contrast to the lithiation process, there were significant differences in the delithiation process between the HEFs and MEFs. For the HEFs, only one oxidation peak was observed at 3.5, 3.25, and 3.05 V for HEF5, HEF6, and HEF7,

respectively. In the case of the MEF4 and MEF3, two distinct peaks occurred around 2.9 and 3.5 V during delithiation (see Figure 5- 2d and e). A similar behavior as for MEF4 and MEF3 has already been observed by Wang et al. for a two-metal-based fluoride system ($Fe_{0.5}Cu_{0.5}F_2$), where the two lithiation and delithiation reaction steps correspond to the transition of Cu^{2+}/Cu^0 and Fe^{2+}/Fe^0 [185]. Accordingly, it can be assumed that in the case of MEF3 and MEF4 similar conditions exist and that firstly one of the metal species reacts with Li, while the others are not yet or not at all involved in the reaction. This will be investigated in more detail below using X-ray photoelectron spectroscopy (XPS). As mentioned above, in the case of HEFs, it is evident that the lithiation/delithiation process is a simple one-step reaction. This will be discussed in the X-ray diffraction (XRD) and transmission electron microscope (TEM) sections. However, we would like to point out that it cannot be excluded that within the broad oxidation peak of the HEFs, several individual reactions belonging to the transition metals may occur separately, and that due to the low concentration of the individual elements this may only be represented in a broad peak. Nevertheless, a continuous shift of the maximum of the oxidation peak from 3.5 (HEF5) to 3.25 (HEF6) to 3.05 V (HEF7) can be observed. It can therefore be assumed that the addition or elimination of an element influences the redox potentials. This paves the way for tailoring the reaction potential and adjusting the electrochemical behavior by changing the elemental composition of the electrode active material.

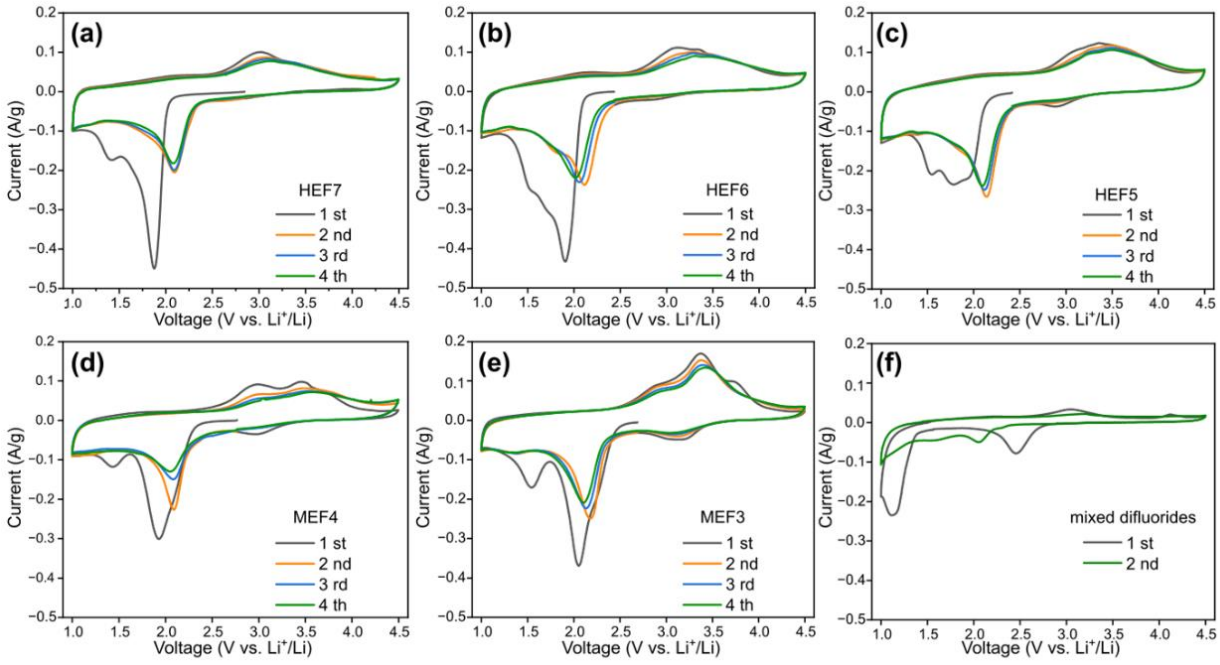

Figure 5- 2: Cyclic voltammograms of (a) HEF7, (b) HEF6, (c) HEF5, (d) MEF4, (e) MEF3, and (f) mixture of all binary fluorides (CuF_2, NiF_2, FeF_2, CoF_2, ZnF_2, MnF_2, and MgF_2) measured in the voltage range of 1.0–4.5 V vs. Li^+/Li with a scan speed of 0.1 mV/s.

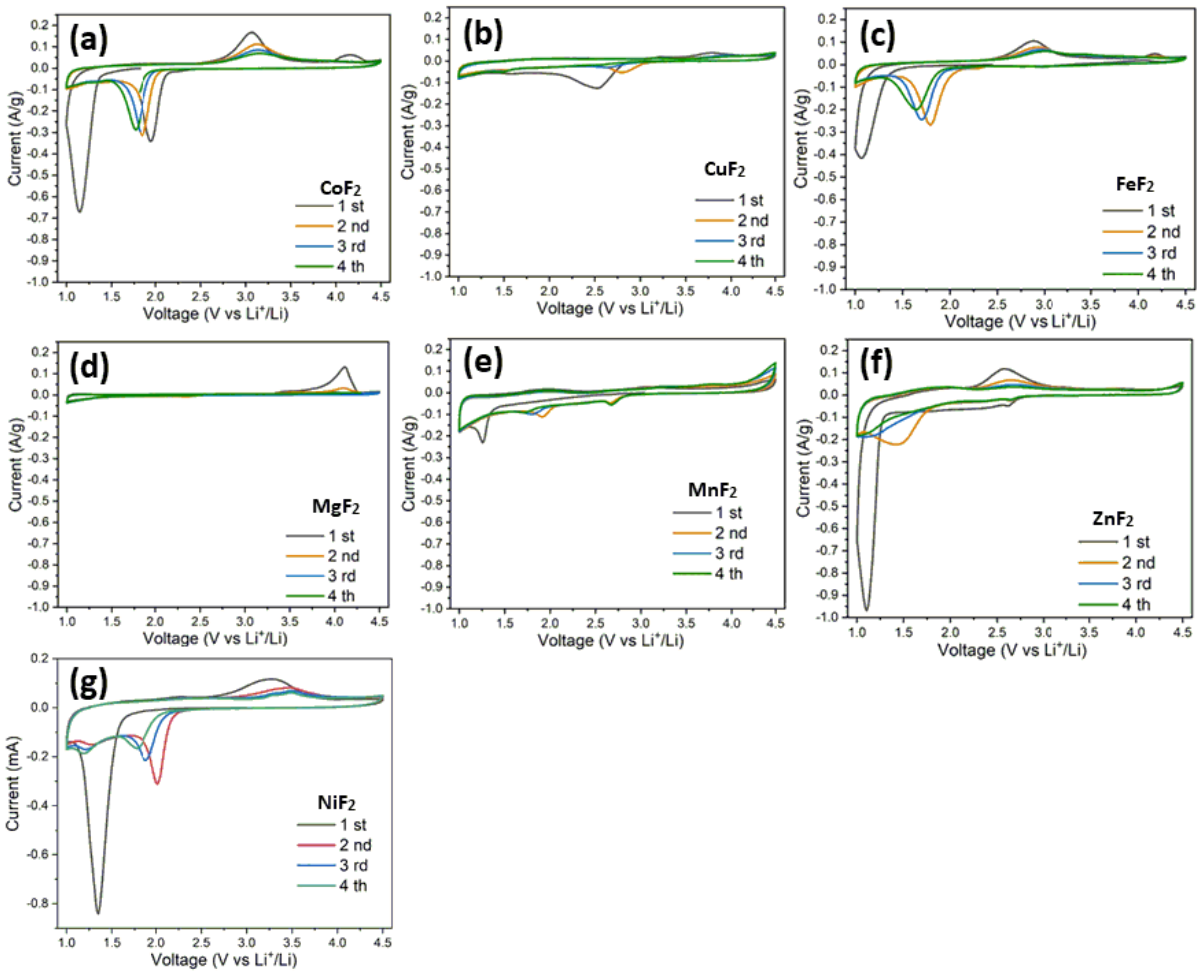

Figure 5- 3: Cycling voltammograms of individual binary fluorides/MWCNT composite.

The galvanostatic rate performance of MEF4, HEF5, HEF6, and HEF7 at different currents is given in Figure 5- 4(a). During the rate performance test, HEF7, HEF5, and MEF4 initially show comparable discharge capacities, while HEF6 shows higher capacities at currents of 25 and 50 mA/g. However, as the current increases (100 mA/g), HEF7 shows increasingly better performance and even after returning to 50 mA/g, it exhibits the highest discharge capacity (~300 mAh/g). The same was also observed for the long term cycling performance at 50 mA/g (Figure 5- 4b). Each HEF sample could yield a discharge capacity of more than 400 mAh/g for the first five cycles at 25 mA/g and then retain more than 100 mAh/g after 80 cycles at 50 mA/g. Whereas the metal fluorides (CoF_2, NiF_2, CuF_2, MgF_2, MnF_2, and ZnF_2) as well as the MEF4 shows a capacity of <100 mAh/g after 80 cycles Figure 5- 5and Figure 5- 4b). MEF4 shows a strong capacity decay compared to HEFs, which also indicates the cycling stability of the HEFs. Although HEF7 had the lowest initial capacity, it showed the highest specific capacity of ~190 mAh/g after 80 cycles. In addition, it is noted that HEF7 showed improved performance compared to HEF6, even though Mg is inactive in the given potential range, which will be discussed in more detail in the XPS part.

In order to investigate the better performance of HEF7 in more detail, the total electron density of the states (DOS) was calculated using density functional theory (DFT). The DOS calculated by DFT for the HEF systems showed a band gap of ~2.2 eV for all three systems (Figure 5- 6), with no significant deviation. A gap state between 0 to 0.8 eV is observed for the systems, which is related to the d band of Cu (see the projected DOS in the Figure 5- 6). This shows a strong tendency of Cu to be reduced from 2+ to 1+. Although the major contribution of valence band maximum (VBM) is from the Fe-d states in the HEF5 system, it is dominated by Mn-d in the HFE6 and HEF7 systems (Figure 5- 6). This clearly shows that Mn has the highest tendency, compared to the other elements, to be oxidized to 3+ and perhaps 4+. This is in line with the previous studies showing a large charge state of 4+ for Mn in the fully-discharged NCM cathodes [199,200]. As expected, no significant change in the DOS is observed after adding Mg to the HEF6 compound. This is because Mg has only strongly localized p states that are located far away from the Fermi level. According to previous reports, increasing the number of metal species improves the lithium transport properties [102], so we speculate that the increase in the disorder in the high entropy fluoride may improve the lithium conductivity of this system. Thus, the electrochemical properties of this system were improved with the increase in the number of metals. Moreover, the HEF7 electrode maintains a discharge capacity of 125 mAh/g after 100 cycles and a high Coulombic efficiency of ~99% even under fast cycling conditions (Figure 5- 4c). It can be seen that in the voltage profiles of HEF7 and FeF_2 (Figure 5- 4d). HEF7 exhibits the lower overpotential between charge and discharge process. Moreover, HEF7 shows a higher discharge voltage than FeF_2, which would benefit the energy density of the battery. The high specific capacity suggests that the HEF-based electrodes presumably undergo conversion mechanisms as the binary fluorides [201]. Since HEF7 shows the best capacity retention/stability, it will be discussed in more detail in the following.

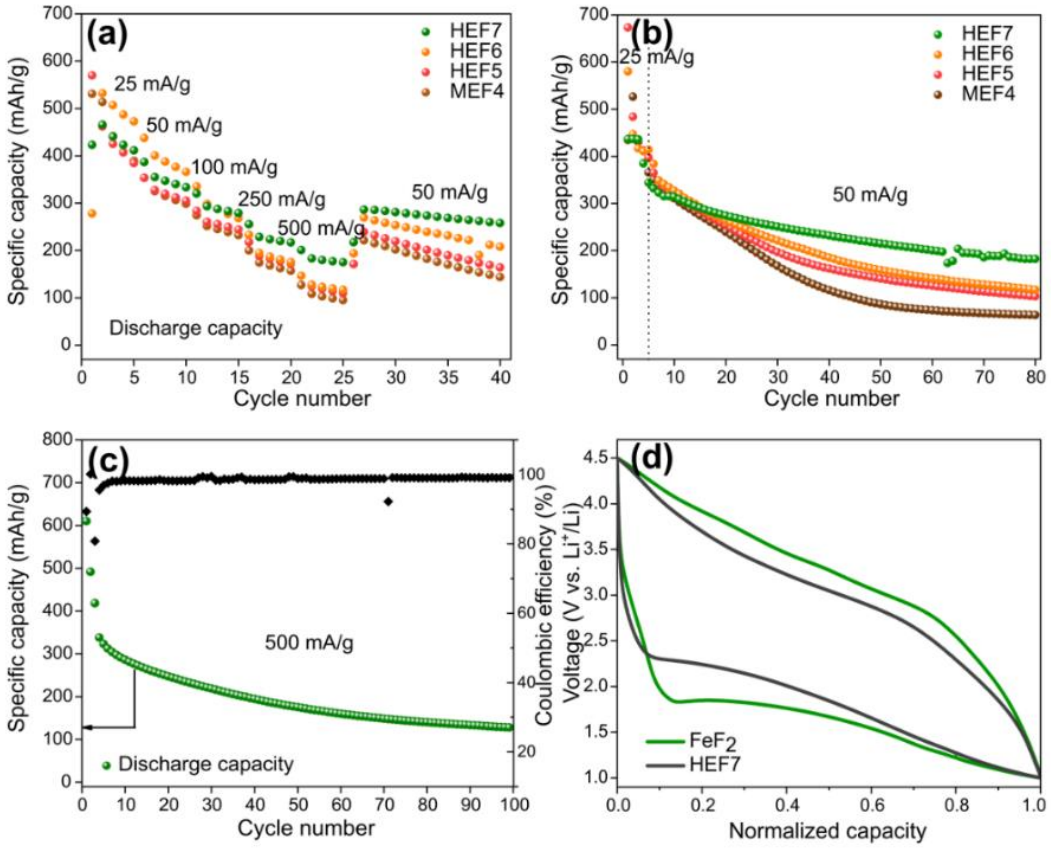

Figure 5- 4: (a) Galvanostatic rate capability performance of MEF4, HEF5, HEF6, and HEF7 at different currents and (b) Cycling capacity at 25 and 50 mA/g measured in the voltage range of 1.0–4.5 V. (c) Cycling performance of HEF7 at 500 mA/g. (d) Comparison of normalized capacities of HEF7 and FeF_2 in the voltage range 1.0–4.5 V at 50 mA/g.

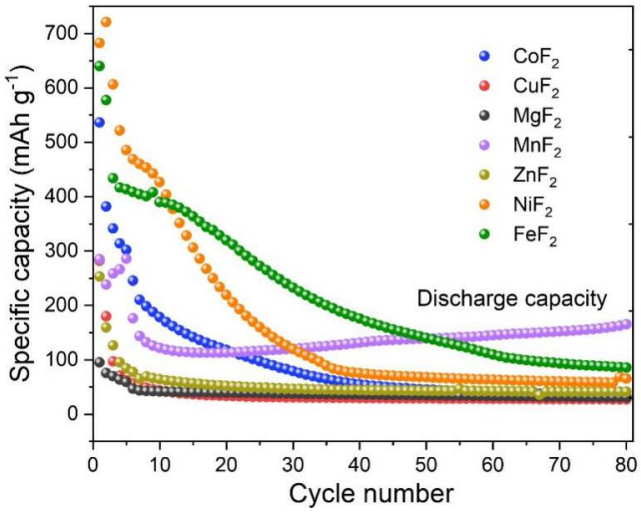

Figure 5- 5: Galvanostatic cycling performance of individual binary fluorides/MWCNT composite. The current implemented during the first 2 cycles accounts to 25 mA/g and the subsequent 50 mA/g.

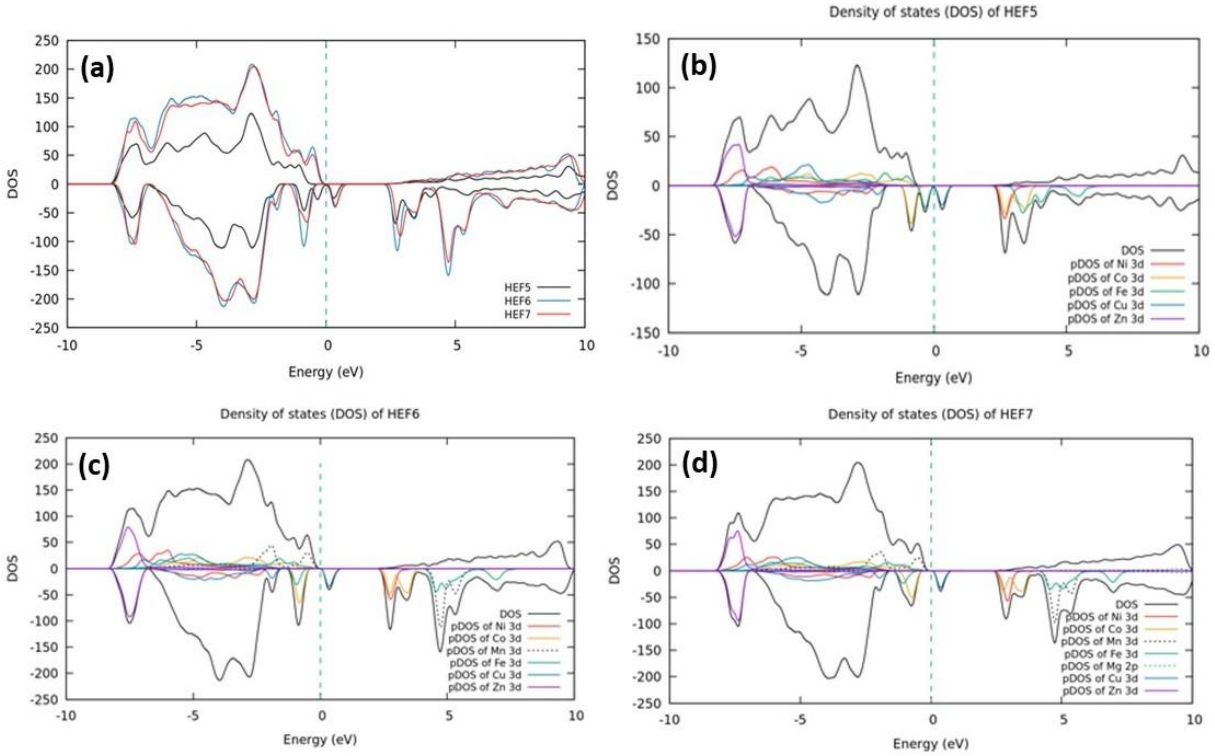

Figure 5- 6: (a) Calculated total density of states (DOS) for three HEF systems. The Fermi level is set to zero. The corresponding projected DOS, (b-c) Projected density of states (pDOS) on d orbital of each element in HEF systems. The Fermi level is set to zero. The corresponding total DOS of each HEF compound is also presented.

5.3.2. Electrochemical impedance spectroscopy

Electrochemical impedance spectroscopy (EIS) is a fundamental technique to define the diffusion process, the charge transfer kinetics, and the electrolyte-electrode resistance [202]. To gain more information about the conductivity of the HEF7 electrodes, EIS measurements were performed. To recognize the individual processes contributing to the EIS response, first, two-electrode cells in symmetric cell configuration (identical HEF7/MWCNT composite electrodes) were prepared. Standard electrolyte (LP57) was utilized for all the EIS tests. Additionally, reasons responsible for capacity fading have been drawn from the EIS results of the cycled cells.

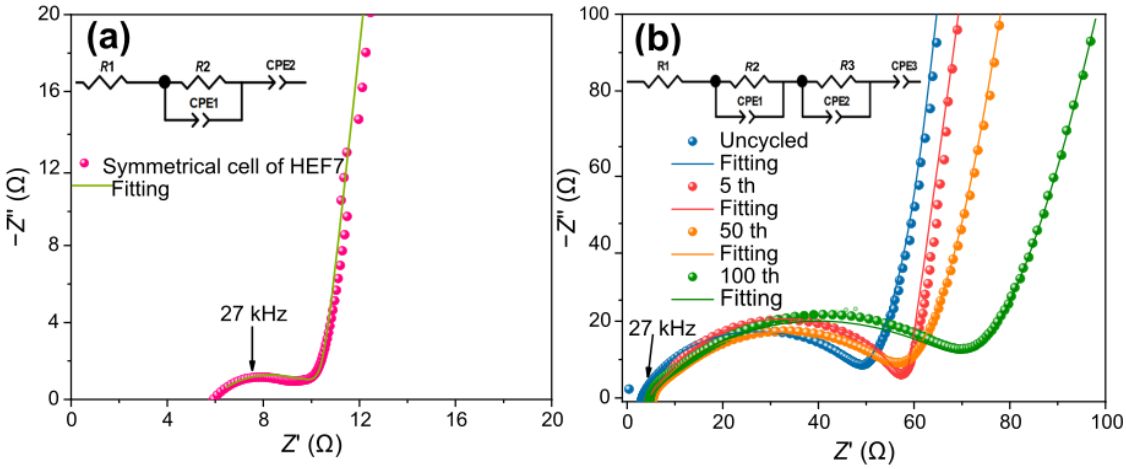

Figure 5- 7: (a) Electrochemical impedance spectra of symmetrical cells with HEF7 electrodes, inset equivalent circuit for fitting the experimental data (where R1 and R2 denote the resistances, CPE1 and CPE2 denote the constant phase elements). (b) Nyquist plots for the HEF7 at pristine state, after 5 cycles, 50 cycles, and 100 cycles, inset is equivalent circuit model used for fitting the experimental data (where R1, R2, and R3 denote the resistances, CPE1, CPE2, and CPE3 denote the constant phase elements). Table 5- 1shows the equivalent circuit values of the fitting components obtained from the equivalent circuit models.

Table 5- 1: Numerical values of the equivalent circuit components obtained by fitting the impedance data from symmetrical configuration cells and cycled HEF7 electrodes in half cells.

Electrodes	**R1** (Ω)	**CPE1** ($F.s^{(n-1)}$)	**n1**	**R2** (Ω)	**CPE2** ($F.s^{(n-1)}$)	**n2**	**R3** (Ω)	**CPE3** ($F.s^{(n-1)}$)	**n3**
Symmetrical cell of HEF7	5.89	0.2742×10^{-3}	0.62	4.63	0.9515×10^{-3}	0.95	-	-	-
HEF7 at OCV	2.90	9.488×10^{-3}	0.79	9.70	3.4048×10^{-5}	0.79	47.26	2.1189×10^{-3}	0.9572
HEF7 after 5 cycles	4.94	5.6641×10^{-6}	1	2.05	1.8422×10^{-5}	0.85	51.4	3.899×10^{-3}	0.9306
HEF7 after 50 cycles	5.14	0.01291	0.64	14.40	4.7575×10^{-5}	0.72	52.35	0.002921	0.9355
HEF7 after 100 cycles	4.33	0.011145	0.64	18.98	5.362×10^{-5}	0.69	68.17	2.3481×10^{-5}	0.9107

Figure 5- 7 shows the Nyquist plots of the HEF7 electrode in a symmetric cell (Figure 5- 7a) and in a half-cell configuration (Figure 5- 7b) along with the respective equivalent circuits used to analyze the EIS data. The continuous lines in Figure 5- 7 show the fitting curves and dots represent the recorded experimental data. In general, the EIS of a half-cell provides information about the

working electrode and the counter electrode, and it is difficult to separate the respective contributions to the spectrum, e.g., charge transfer between each electrode and the electrolyte. The EIS information of a symmetric cell consisting of two identical electrodes can eliminate the influence of the counter electrode and thus allow a more direct investigation of the electrode material and interfacial properties against the electrolyte [203]. The EIS spectrum of the symmetrical cell of HEF7 (Figure 5- 7a) is composed of a depressed semicircle in the high frequency region and a sloping straight line feature in the low frequency region. The real part of the impedance is denoted as *R*1 in the equivalent circuit, which may arise from the electrolyte resistances. The first semicircle in the high frequency region may be attributed to the charge transfer resistance between the cathode-electrolyte (*R*2) [204]. The straight line shown in the low-frequency region can be represented by constant phase element (CPE2), which shows the blocking nature of Li^+ diffusion on the cathode side.

Figure 5- 7(b) shows the EIS data from HEF7/MWCNT composite electrode with Li counter electrode in a half-cell configuration. From these EIS spectra, the experimental data of electrodes show a prominent blocking feature (at low frequencies) and two flattened high and medium frequency semicircles. The changes in the first high-frequency semicircles in the cycled EIS electrode can be caused by the SEI layer formation at the cathode surface. These semicircles of the half-cell configuration in Figure 5- 7(b) are similar to the counterpart presented in symmetrical cell spectrum (f_{max} = 27 kHz) with an additional influence from the SEI formation during cycling. The second semicircle in the medium frequency region can be ascribed to the charge transfer resistance caused at the anode/electrolyte interface (*R*2). In the composite structure, better interfacial contact between the active material and MWCNT could be anticipated due to the porous structure of MWCNT. The derived parameters from the equivalent circuit model fitting performed with the *Z*-view software can be found in Figure 5- 1. Due to the overlapping of the high and medium frequency semicircles of the half-cell measured at open circuit voltage, the absolute quantification of the equivalent circuit components was quite cumbersome. Nevertheless, with progressing cycle number from 5 up to 50 cycles it is evident that the SEI formation plays a significant role in increasing the charge transfer resistance on the cathode side, while further cycling results in a decrease in resistance. In addition, the slope of the straight line in the low frequency region decreases with the increase of the cycle number, indicating the decrease in the capacitive nature of the electrode and increased resistive component. This may be due to the volume change of the active material during cycling and the resulting poor contact between the particles, causing higher resistance for both Li^+ and electron transport. A more notable resistance increase is observed for the medium frequency semicircle attributed to the charge transfer to the Li anode. This increase might even play a more significant role in the observed capacity fading.

The degradation of the anode surface might be due to the elemental dissolution of Fe, Mn, Ni from the active material through the electrolyte and their presence at the electrolyte/anode interface, which was detected by means of energy dispersive X-ray spectroscopy (EDX) (Figure 5- 8).

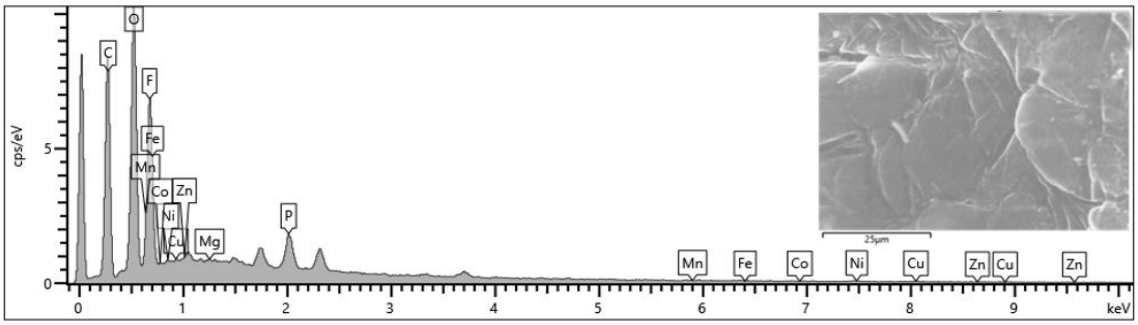

Figure 5- 8: SEM of lithium (inserted) after 100 cycles and corresponding EDX analysis.

5.3.3. Structural evolution during cycling

In order to have a better understanding of the reaction mechanism observed in HEF based materials and structural changes in the reversible lithiation/delithiation processes, a comprehensive characterization implementing XPS, XRD, and TEM was performed.

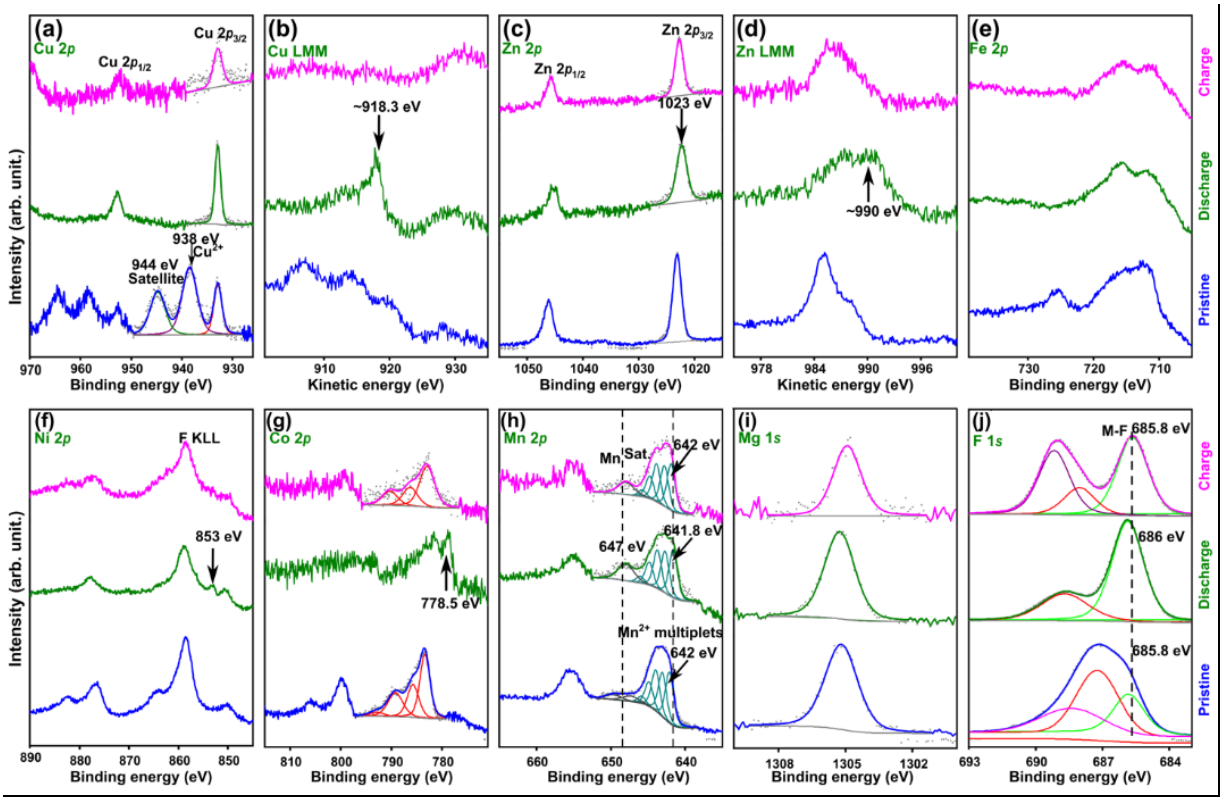

Figure 5- 9: XPS spectra of (a) Cu 2*p*, (b) Cu LMM (c) Zn 2*p*, (d) Zn LMM, (e) Fe 2*p*, (f) Ni 2*p*, (g) Co 2*p*, (h) Mn 2*p*, (i) Mg 1*s* and (j) F 1*s* of pristine electrode (blue), first lithiation electrode (green), and first delithiation electrode (pink).

XPS analyses were performed on HEF material in the initial, discharged, and charged states (Figure 5- 9). Cu ions in the pristine electrode show two peaks at around 944 and 937 eV, which could be attributed to the Cu^{2+} main peak and satellite of Cu $2p_{2/3}$, respectively (Figure 5- 9a). The third peak at lower binding energy (~933 eV) can be attributed to either Cu^{1+} or Cu^{0}. The Cu peak is no longer Cu^{2+} and stays in the reduced state at the binding energy of around 933 eV after discharge. The Cu LMM peak of HEF7 is overlapped with Zn LMM with low intensity. Nevertheless, it can be inferred from the spectra of charged and discharged electrodes (Figure 5- 9a and b) that Cu is involved in the reaction. Narrow Zn $2p_{3/2}$ peak consistently appears at around 1023 eV; however, the binding energies of Zn^{2+} and Zn^{0} are very close to each other and the analysis of Zn LMM auger peak (Figure 5- 9d) is required. The Zn LMM peak at 990 eV at the lithiated electrode indicates the emergence of metallic Zn; then the peak shifts mainly back to 985 eV at the delithiated electrode and can be attributed to the Zn^{2+} regenerate. The analysis of Fe 2*p* ions (Figure 5- 9e) is hampered due to the overlap of Ni and Co auger peaks resulting in high background intensity of Fe 2*p* region. The Ni ions also overlap intensively with F KLL auger peaks, which makes their analyses difficult. However, the comparison of the spectra in Ni 2*p* region (Figure 5- 9f) shows the emergence of a small shoulder at around 853 eV in the discharged (lithiated) electrode that could probably be attributed to the metallic Ni. This small shoulder is indicated by an arrow and disappears again after delithiation (charged state), therefore potentially suggesting reversibility for Ni^{2+} formation by delithiation [205,206]. The Mn ions in the pristine electrode can be attributed to the Mn^{2+} ions, according to the provided peak deconvolution in Figure 5- 9h that shows the multiplet splitting of Mn^{2+}. The metallic Mn $2p_{3/2}$ and Mn $2p_{1/2}$ peaks appear normally at low binding energies at around 639 and 648 eV [207]. The peak positions show some slight negative shifts for the discharged states in comparison with the pristine electrode with the appearance of a peak at 647 eV and a small shoulder at 660 eV, indicating the reduction of Mn^{2+} into Mn metal phases during the discharging processes [208,209]. The spectra of Co ions in pristine and charged electrodes (Figure 5- 9g) show the characteristic satellite of Co^{2+} ions is around 6 eV higher than the main peak (indicated by an arrow in Figure 5- 9g); however, their low intensity, mainly in the cycled electrodes, makes peak assignment difficult. The emergence of a small shoulder at around 778.5 eV in the discharged (lithiated) Co $2p_{3/2}$ spectra might indicate the reduction of Co ions to metallic Co upon lithiation [210]. Mg 1*s* peak (Figure 5- 9i) appears at around 1305 eV and remains consistent in all of the electrodes. Its binding energy can be attributed to Mg^{2+} ions, whereas the metallic Mg normally appears at around 1303 eV. Therefore, Mg is not involved in the reduction or oxidation process. Fluoride ions in the structure of HEF7 appear at around 685.5 eV (Figure 5- 9j), whereas the PVDF peak appears at around 688 eV. In F 1*s* spectra, also the contribution of electrolyte degradation products can be

found. However, the binding energy difference between Li-F and M-F is too miniscule to distinguish. Therefore, the peak in F 1*s* between discharged and charged sample is observed to slightly change. Nevertheless, we can infer that Li-F and M-F are generated after discharge and charge, respectively. In summary, with the exception of Mg, differences between the oxidation states in the different states (pristine, discharged, and charged) can be identified for all elements, suggesting a redox reaction during cycling. In the case of Mg, it can be assumed that it may have a stabilizing effect on the system due to the non-reaction. A similar behavior has already been observed for HEO [(CoCuMgNiZn)O], in which a stabilization matrix structure was formed by the species that were not involved in the conversion reaction [79]. Possibly, the better stability for HEF7 can be explained by a comparable mechanism. Further structural investigations by means of XRD and TEM should provide more information.

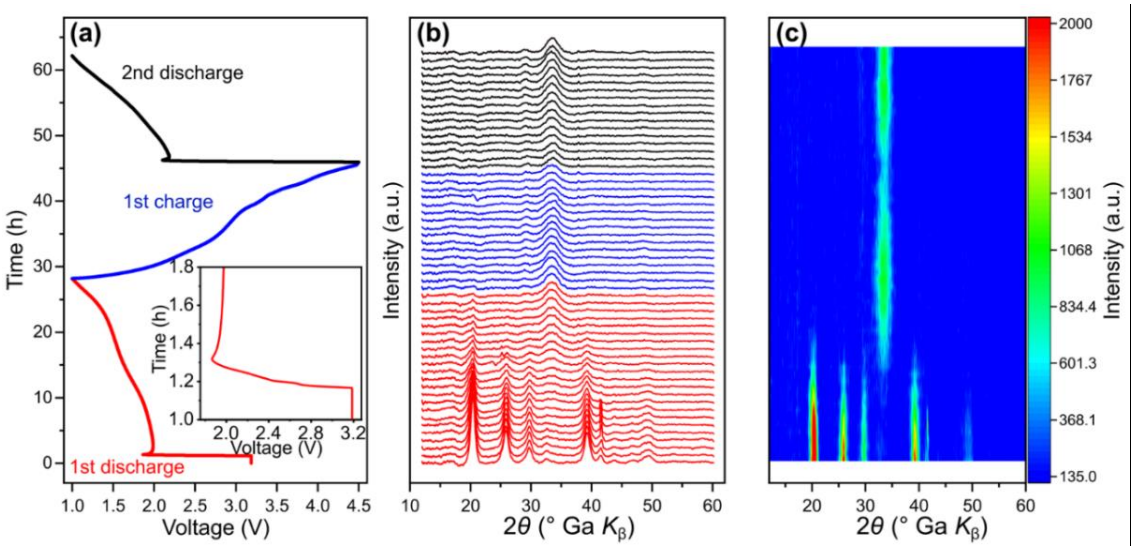

Figure 5- 10: Operando XRD collected during the first discharge and charge process at a current density of 50 mA/g between 1 and 4.5 V vs. Li^+/Li (a), diffraction patterns (b) and corresponding contour map (c).

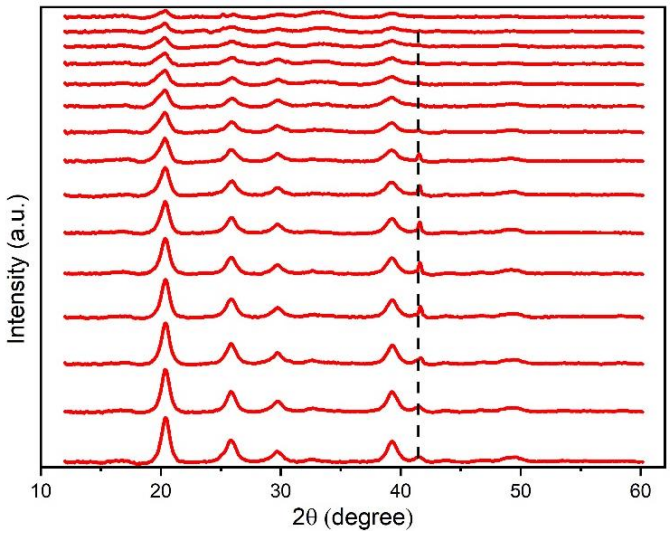

Figure 5- 11: XRD patterns and the evolution of reflection of (220).

Operando XRD was performed to shed light on the possible conversion mechanism occurring during cycling. Ga-jet K_β X-ray source with adjusted optics was used to achieve high intensities with limited sample volume. Figure 5- 10 shows voltage profiles (1st discharge/charge and 2nd discharge) together with the evolution of the reflection position and the contour plot for HEF7. As shown in Figure 5- 10(a), the discharge reaction begins at an open circuit voltage of 3.1 V, a rapid voltage drop to 1.86 V (inset image of Figure 5- 10a) follows. As reported by Xiao et al., this drop could be ascribed to the pseudo-intercalation of Li^+ into the structure and possible disproportionation of metal compounds to form Li_xHEF7, which remains its initial rutile structure [211–213]. Afterwards, a significant recovery of the voltage occurs before the flat operating voltage at ~1.95 V, indicating the onset of the conversion reaction [213]. The intensity of the HEF7 reflection at 41° is observed to increase and then shift to 41.3° (Figure 5- 11) during lithiation. Moreover, the intensity of the reflections associated with the initial rutile-type structure becomes weaker as the lithiation progresses, while a new broad reflection at 34° is observed. This new reflection (34°) could belong to a rock-salt structure arising from the formation of nano-sized metal species and possibly metal-substituted LiF as reported for FeF_2. Further, the formation of an undetectable amorphous phase during lithiation might be possible [41]. With ongoing lithiation, the reflections from the initial rutile structure disappear and do not reappear after delithiation. This behavior is typical for conversion materials and might result from the formation of small crystallites below the detection limit of XRD [17,214]. Therefore, TEM is used for further characterization.

Figure 5- 12 shows the ex-situ TEM images of electrochemically lithiated (Figure 5- 12a) and delithiated (Figure 5- 12c) HEF7 (1.0 and 4.5 V, respectively), and their corresponding selected area electron diffraction (SAED) patterns (Figure 5- 12b and d). At this point we would like to mention that the crystallinity of the discharged sample is very low, so we have only a few diffraction rings to index the structure. On the other hand, we have too many possible candidates, which means that a reflection can be indexed also by many candidates. Nevertheless, SAED reveals that the initial HEF7 electrode material was electrochemically reduced to a solid solution of transition metals with LiF after lithiation (discharged to 1.0 V) (Figure 5- 12b). EDX-mapping shows a homogeneous distribution of the elements in the nanoscale after lithiation, with no agglomeration or segregation present (Figure 5- 12e). Besides, the Mg is also uniformly distributed in the discharged sample, suggesting that unreacted Mg containing compound (Mg^{2+}), possibly within the dominant amorphous phase, is uniformly distributed in the mixture of metal alloy and LiF, possibly metal-substituted. After delithiation of the HEF7 electrode to 4.5 V, the majority of areas in the HR-TEM image (marked in Figure 5- 12c) show lattice spacing of ~0.33 nm. This is a clear indication that *d*-spacing corresponds to the (110) plane of the parent rutile

phase. Following the SAED after delithiation (Figure 5- 12d), the rutile structure is partially reformed. However, the ring of (120) is observed to be broadened and a small diffraction signal appeared at 4.05 1/nm in the corresponding profile of the SAED pattern (Figure 5- 13) which could be caused by the overlap with (111) of fcc metal and (110) of bcc metal, indicating that unreacted metal solid solution remained in the charged sample.

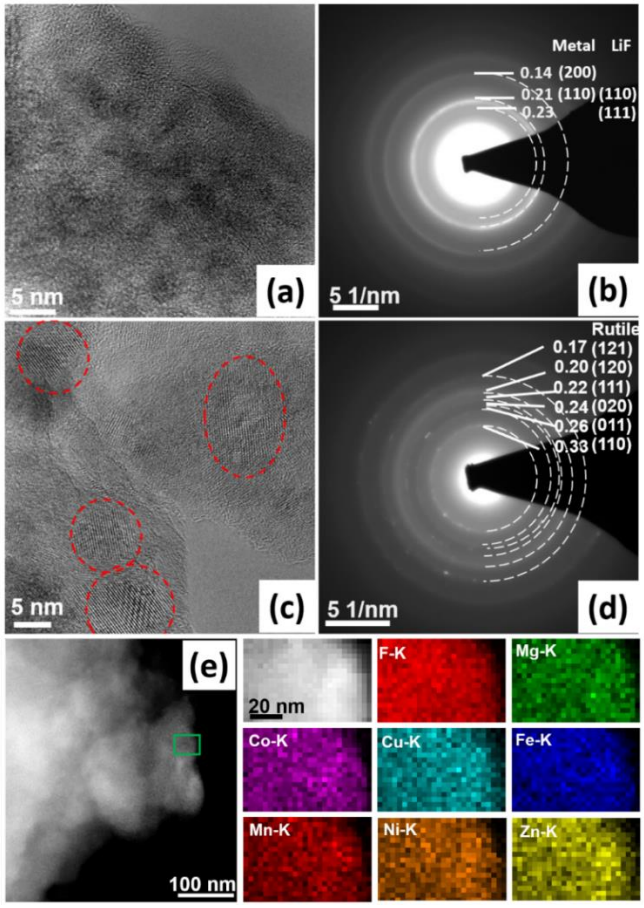

Figure 5- 12: HR-TEM images of various cycled HEF7 electrodes after lithiation to 1.0 V (a), delithiation to 4.5 V (c), and their corresponding SAED patterns in panels (b) and (d), respectively (all values of d spacing illustrated in SAED are given in nm). (e) EDX-mapping after 1st discharge.

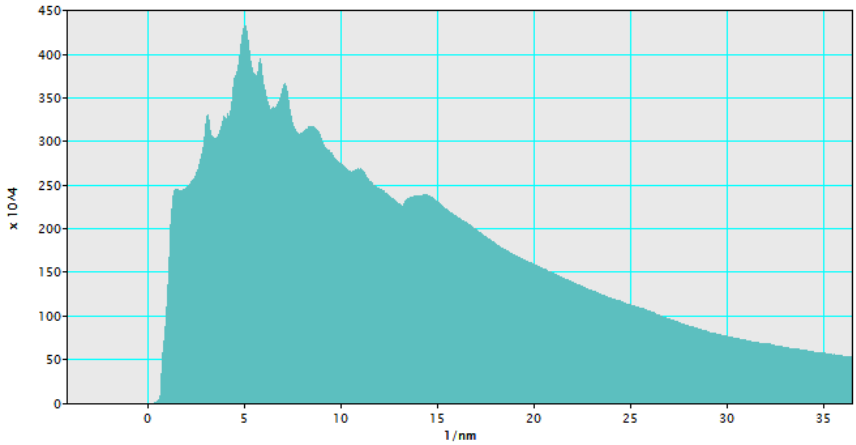

Figure 5- 13: SAED profiles of delithiated HEF7 electrodes.

It was also observed in XRD that the intensity of the peak appearing at 34° did not disappear completely after delithiation process was completed, thus also indicating the presence of unreacted metal particles in the material. This indicates that the metal does not fully convert to fluoride during delithiation, which could be ascribed to the poor contact resulting from the volumetric change during the conversion process. During the delithiation process, the reformation of high entropy compounds breaks the conductive network formed by metals, which impedes the reaction leading to capacity fading. It can be inferred from CV and XPS results that HEFs solid-solution phase has been reformed after F^- transfer from LiF to the solid solution of transition metals. This evidence combined with the operando XRD pattern (Figure 5- 12), confirm a conversion reaction mechanism present in the HEF based materials. The occurrence of the continuous network of metallic nano domains can be beneficial as an internal conductive network. This can facilitate the conversion kinetics and voltage polarization, thereby improving the overall electrode cycling performance. The continuity of this network however needs to be maintained throughout lithiation and delithiation to achieve its maximum effect.

5.4. Conclusion

In summary, HEFs have shown to be high-capacity cathode materials for lithium-ion batteries. It is proposed from the lithiation/delithiation process that the electrochemical activity of HEFs based materials could be tailored by simply changing the constituent elements. With in-depth characterization of the electrodes by ex-situ XPS, operando XRD, and ex-situ HR-TEM techniques, it has been revealed that the solid solution of transition metals is present in the lithiated phase together with a substantial amount of amorphous phase and possibly metal-substituted LiF. The rutile HEFs phase could be partially regenerated after delithiation. HEF with seven metal elements exhibited high capacity at the beginning of cycling process. More importantly, HEF7 maintained a moderate cycling performance with a capacity of more than 125 mAh/g after 100 cycles at a high specific current of 0.5 A/g. The conversion mechanism of HEF7 needs to be further investigated to determine the underlying reactions contributing to the enhanced electrochemical performance. As a future perspective, the potential advantages of HEFs can be further improved. One approach is constructing a composite electrode consisting of nanostructured HEFs particles whose size must be comparable to the length scale of the conversion reaction and directly connected to electronically conductive scaffolds. The other approach is coating the material to preserve metal ions dissolution into the liquid electrolyte and onto the lithium anode to benefit the cycling stability.

Chapter 6

6. Photonic curing synthesis of high entropy oxide for coating on high entropy fluorides

6.1. Introduction

High entropy fluoride has potential applications as a potential cathode material for lithium batteries. However, the electronic conductivity of fluoride is poor due to the large band gap caused by the property of F [215]. In addition, MFs also suffer from the problem of dissolution of transition metal ions, which exacerbates the ions transfer to the surface due to the separation of the metal phase to the particle surface [216]. It was found that in situ coating of conductive additives is essential for the synthesis of fluoride composites with good electrochemical properties. In addition, Al_2O_3-coated FeF_2 can also prevent side reactions by limiting the direct electrode-electrolyte contact, which improves the cycle life [217]. The electrochemical performance of FeF_3 with Fe_2O_3 coating also showed a significant improvement [218]. As shown in Chapter 3, the performance of NCM cathode materials was significantly improved by coating of with HEOs. Therefore, in this work, HEO ((MgCoNiCuZn)O) coating on (HEF ($Cu_{1/7}Ni_{1/7}Fe_{1/7}Zn_{1/7}Co_{1/7}Mn_{1/7}Mg_{1/7}$)$F_2$) active material was attempted to improve its cycling performance by minimizing elemental dissolution into the electrolyte.

6.2. Experiment

Preparation of HEO coated HEF

HEF is synthesized by mixing MnF_2, FeF_2, CoF_2, NiF_2, CuF_2, ZnF_2, MgF_2 in equimolar ratio by long-term high energy milling process carried out at 500 rpm for 48 h in WC jar (WC ball to powder weight ratio as 20:1).

A nitrate precursor solution with 7.31 mg $Mg(NO_3)_2 \cdot 6H2O$, 88.295 mg $Co(NO_3)_2 \cdot 6H_2O$, 88.29 mg $Ni(NO_3)_2 \cdot 6H_2O$, 6.63 mg $Cu(NO_3)_2 \cdot 2.5H_2O$ and 88.48 mg $Zn(NO_3)_2 \cdot 6H_2O$ dissolved in 0.224 mL ethanol was prepared, then 0.5 g HEF was added and constantly stirred at ambient temperature for 60 minutes, then heated at 60 °C to enable solvent evaporation. The prepared powder is evenly dispersed on a 5*5 cm silicon wafer and exposed to photonic curing at 3 kV for 75 s, shaking each time evenly and cooling to room temperature. Irradiation was repeated 6 times.

6.3. Results and discussion

6.3.1. Characterization of HEO coated HEF

As shown in Figure 6- 1, the XRD patterns of as-prepared HEF and HEO coated HEF are compared. The diffraction peaks in the XRD patterns of HEF7 are indexed based on a rutile structure. However, in the HEO coated HEF, impurity peaks appeared, which can be indexed by the spinel structure. To further confirm the structure of HEO coated HEF, TEM was performed.

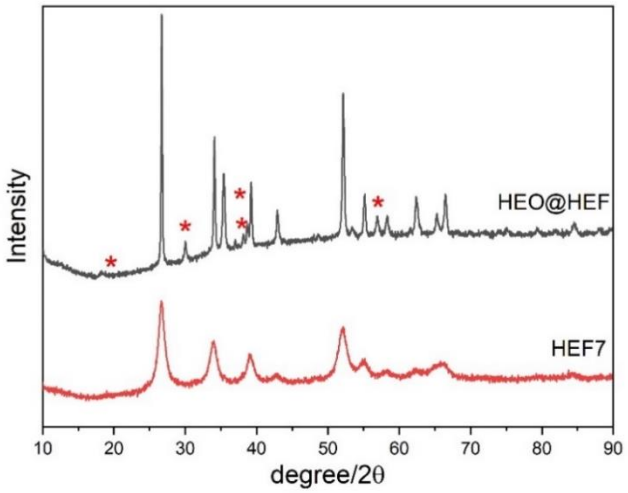

Figure 6- 1: XRD patterns of HEF7 based nanoparticles and HEO coated HEF7.

The surface morphology of the material particles cut by FIB is shown in Figure 6- 2. From Figure 6- 2a, it can be seen that the material consist of porous particles and the pore size within the material is not uniform, with a diameter of about 100 nm. However, it is observed from the EDX mapping that the distribution of elements after the coating is not homogeneous. It can be noted that the F, Mn, Co, Ni, and Zn are uniformly distributed. Still, the O is not expected to appear on the surface of the material particles but tends to appear on the surface of the internal pores. In addition, Fe also tends to appear on the surface of the internal pores, while Cu and Mg appear in non-uniform aggregates. This may be due to the migration of elements during instantaneous temperature increase during the photonic curing process.

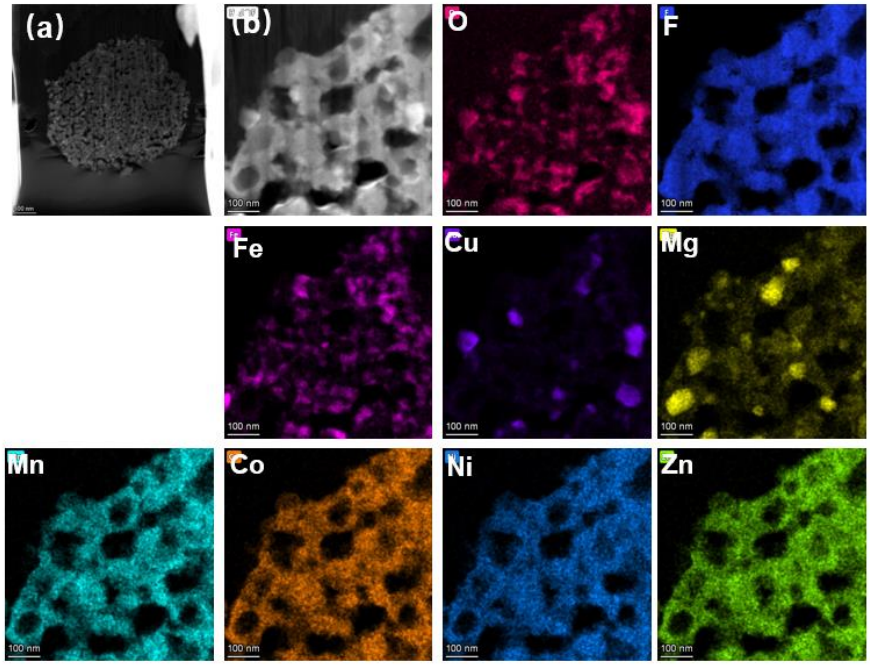

Figure 6- 2: STEM-HAADF imaging of HEO coated HEF (a, b) and EDX mapping

In order to further confirm the formation and structure of HEO and HEF, as well as the oxide on the inner pore surface and the fluoride inside the material, TEM measurements were performed on the HEO coated HEF samples at different selected areas, and the results are shown in Figure 6- 3, Figure 6- 4, and Figure 6- 5. As shown in Figure 6- 3, the surface of the enclosed pores is enriched with Fe elements, and the FFT shows that the material exhibits a spinel-type structure with a HR-TEM crystal plane spacing of 0.25 nm.

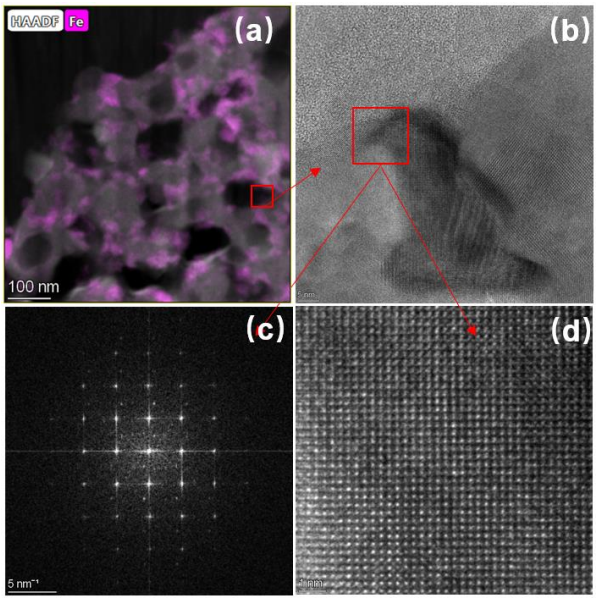

Figure 6- 3: TEM (a), HR-TEM (b, d)FFT (c) imaging of the HEO coated HEF for the selected area.

Additionally, the presence of a monoclinic phase was detected in the Cu aggregates indicating the generation of CuO (Figure 6- 4). This indicates that due to the migration of elements, the rock salt-type structure is not formed, but spinel-type and monoclinic oxides are formed instead. In addition, some rutile structures are still present in the material, which may be the unmigrated elements Mn, Co, Ni, Zn still remaining in solid solution forming the metal fluoride host. Therefore, it might be possible to try to coat HEO on monomeric metal fluorides of materials in which the elements do not migrate, e.g., MnF_2, CoF_2.

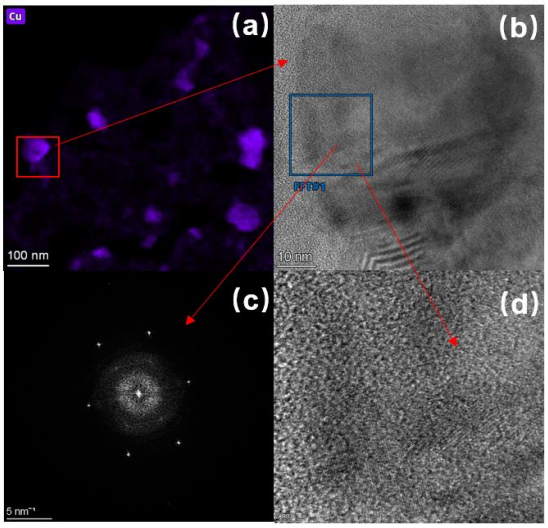

Figure 6- 4: TEM (a), HR-TEM (b, d)FFT (c) imaging of the HEO coated HEF for the selected area.

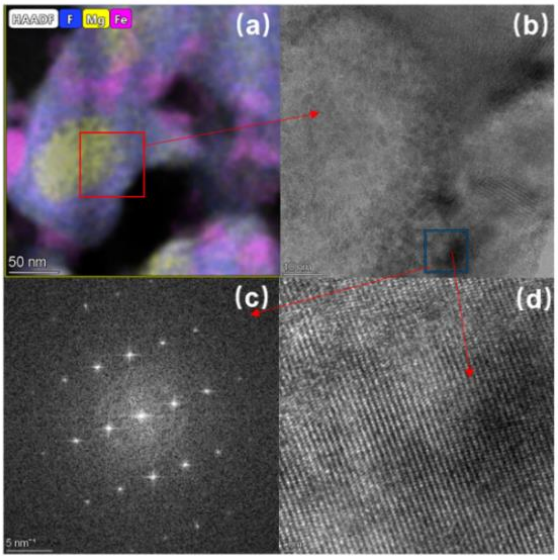

Figure 6- 5: TEM (a), HR-TEM (b, d)FFT (c) imaging of the HEO coated HEF for the selected area.

6.3.1. Electrochemical performance of HEO coated HEF

Photonic curing partially destroyed the structure of HEF and the rock salt-type high entropy oxide was not formed, nevertheless, the electrochemical properties were tested. According to Chapter

5 in Figure 5- 2, only one major reduction peak appears in the CV of the high entropy fluoride (HEF7) at 1.99 V vs. Li^+/Li. However, in this material, as seen in Figure 6-6a, the lithiation process begins from 2.1 V and the reaction is not completed until 1.0 V. This broader peak may originate from the reduction of the spinel oxide in addition to the HEF. Therefore, two distinct peaks appear during the delithiation process, so the presence of solid solution reaction in HEF7 is not present in HEO coated HEF. One of the reasons for the disruption of the solid solution reaction present in HEF7 could be that the high entropy fluoride compound became a medium entropy fluoride containing only four transition metals Mn, Ni, Co and Zn, due to elemental diffusion during photonic curing process. Another possibility is that the spinel-type oxides are also contributing to the redox reaction. As seen in the first cycle of the battery cell shown in Figure 6-6b, the coated material exhibits a lower capacity than pure HEF7, which may be due to the reaction of elements such as Fe and Cu with oxygen, resulting in a low reduction potential and therefore not contributing to the capacity.

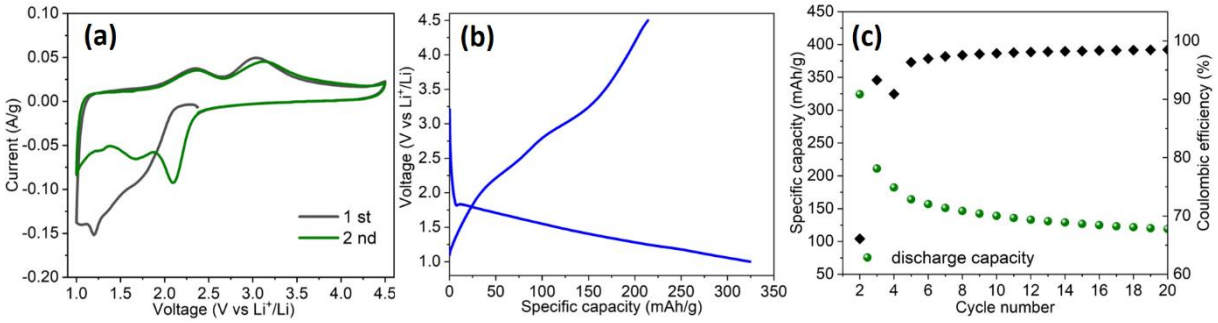

Figure 6- 6 Cyclic voltammograms of (a) HEO coated HEF measured in the voltage range of 1.0–4.5 V vs. Li^+/Li with a scan speed of 0.1 mV/s, (b) Voltage profiles at 50 mA/g, (c) Galvanostatic cycling performance at 50 mA/g for the 1st cycle followed by 500 mA/g.

6.4. Conclusion

Coating of HEF by photonic curing causes migration of Fe, Mg, Cu, etc., and HEO cannot be formed on the surface of HEF. However, Mn, Zn, Ni, Co can still maintain the rutile structure, so HEO may not be suitable for coating HEF, but may be used for coating materials such as MnF_2 and CoF_2. The particle shape and size of the active materials also needs to be considered. Especially its size in relation to the particle size of the coating material. It is recommended for the application of photonic curing to coat active materials with micro-meter sized particles that are structurally stable up to approximately 600 °C. Here the synthesis method of the active material would play a crucial role in optimizing powder morphology and stability before coating.

7. Conclusion and outlook

HEMs, as a new class of materials, have attracted a lot of attention in recent years due to their potential applications in energy storage systems. The synthesis of high entropy materials, their characterization and the study of their electrochemical applications are an attractive class of future research fields. Therefore, this thesis starts with HEOs, a new synthesis method of HEOs was introduced and their application in batteries was developed. The successful synthesis and processing of new HEFs is achieved based on their electrochemical behavior, and the performance of HEFs in lithium batteries was explored.

In Chapter 2, two high-entropy oxides, rock salt-type high-entropy oxide and spinel-type high-entropy oxide, were synthesized by photonic curing, which is a simple and fast method that does not require as much energy and time as conventional methods such as sintering. Based on the advantages of this synthesis method, we have tried to apply this synthesis method to the preparation of binder-free electrode materials, and successfully applied it to lithium batteries.

In addition, due to the good electronic conductivity and lithium ion conductivity of HEO, in Chapter 3, HEO and LiHEO are attempted to be applied to clad NCMs with high nickel, and the mechanism of the improved cycling stability of NCMs after the coating is investigated. In this study, uniform thin layers of LiHEO and HEO were successfully coated on NCM851005 by an ultra-fast photonic curing method. The LiHEO and HEO coatings significantly improved the cycling stability of NCM851005 due to the fact that the coatings prevented the reaction between the electrolyte and the electrode material, which led to the improved stability of the NCM particles, resulting in a stable average discharge voltage and a more stable cycling performance even in the high cut-off voltage range. The successful utilization of photonic curing in synthesis of HEOs provides an opportunity to open up new materials and new ideas.

Inspired by the fact that HEOs, a conversion electrode material, has excellent cycling stability compared to conventional conversion materials, and that fluorides are promising conversion cathode materials with high energy density, we attempted to synthesize high entropy fluorides for conversion cathode materials.

In Chapter 4, multicomponent rutile ($P42/mnm$) structured fluorides, containing 4 to 7 transition metals (Co, Cu, Mg, Ni, Zn, Mn, Fe) in equiatomic ratios, were synthesized using a simple mechanochemical approach. Based on the combined investigations from XRD, ICP-OES, TEM, EDX and EELS studies, it is shown that all pristine HEF samples crystallized in a phase-pure rutile structure with the presence of agglomerated fine nanoparticles. The identification of the local

structure of the HEF compounds was probed by and XPS. The local structural disorder of the HEF compounds arose due to the synthesis process and the resulting variation in the oxidation states of Fe was detected utilizing Mössbauer spectroscopy. These high entropy fluorides represent an additional class of high entropy ceramics, which have recently attracted attention especially due to the development of high entropy oxides.

In Chapter 5, HEFs are successfully used as battery cathode materials combined with MWCNTs, and demonstrated as high-capacity cathode material for lithium-ion batteries. It is proposed from the lithiation/delithiation process that the electrochemical activity of HEFs based materials could be tailored by simply changing the constituent elements. With in-depth characterization of the electrodes by ex-situ XPS, operando XRD, and ex-situ HR-TEM techniques, it has revealed that the solid solution of transition metals is present in the lithiated phase together with a substantial amount of amorphous phase and possibly metal-substituted LiF. High entropy fluorides as a conversion material and its electrochemical properties can be tailored, in the future, more synthesis methods of HEMs and electrochemical applications should be discovered.

The novel coating method introduced throughout this work by means of photonic curing opens new possibilities for coating temperature sensitive active materials and delivers uniform thin coatings. Nevertheless, many prerequisites need to be provided to avoid a formation of material composites instead of coatings, as shown in Chapter 6. The particle size of the respective materials has to be adjusted as well as the thermal stability of the active material up to moderate temperatures.

Acknowledgements

This work has been accomplished through fruitful collaboration, the support of colleagues, friends and family. And I am grateful to all those who supported me in completing my PhD during this period.

First, I would like to express my sincere gratitude to my PhD supervisor Prof. Dr.-Ing. Horst Hahn. I would like to thank Prof. Dr. Horst Hahn for providing me with the opportunity to pursue my PhD at the Institute of Nanotechnology (INT), for providing me with the best conditions for scientific research and a good international research environment. Next, I would like to thank my thesis supervisor, Dr. Miriam Botros for her patient guidance and detailed scientific discussions throughout the process, as well as for her revision of the thesis. I would like to thank Dr. Ben Breitung for his scientific guidance and constant inspiration, especially for the support at the beginning of my PhD. I would like to thank Dr. Qingsong Wang for discussions on my thesis and experimental design. I would like to thank Dr. Simon Schweidler for his constructive discussions with me. Their constant support, motivation and guidance enabled me to complete my PhD thesis.

I would like to thank Prof. Christian Kübel's group for their TEM support, especially Dr. Kai Wang and Dr. Yushu Tang, for their characterization of the material with TEM measurements, contributing a very important part of my thesis. I would like to thank Dr. Raheleh Azmi for carrying out the XPS measurements. I would like to express my sincere thanks to my partner and colleague Dr. Parvathy Anitha Sukkurji, who has provided us with excellent opportunities to work together. Thanks to Dr. Abhishek Sarkar for his guidance in the use and maintenance of the NSP. Thanks to Dr. Surya Abhishek Singaraju for training in photonic curing and instrument maintenance. I would also like to thank Martin Limbach for his endless support during the set-up and maintenance of many instruments. In addition, thanks to Dr. Ibrahim Issac, Dr. Yanjiao Ma, Dr. Junbo Wang, David Stenzel and Lin Ling, whose technical support helped solve many problems in the experimental work and enriched my PhD experience. I would like to thank Mohana Veerraju Kante for saying good morning to me every day and accompanying me home from work. I would like to thank all the members form both Dr. Miriam Botros and Dr. Ben Breitung's groups for their great support and help with my work.

I would also like to thank CSC for the financial support that made it possible for me to come to Germany to study and pursue my PhD. In addition, I am very grateful to the teachers I have met in my life, Prof. Guanglei Cui and Prof. Zhihong Liu, who guided me along my research and were role models of my research.

I would like to give a special thanks to my boyfriend, Han Wei, who has always been there for me. We have not been able to see each other over the years, but he always encouraged me. We are separated by miles, but inseparable by our hearts connection. I am also grateful to my mother—Chunzhi Gao, father—Kaixian Cui, my brother—Zongjian Cui and sister—Yanfang Cui, who have always loved me unconditionally and supported me quietly.

And of course I have myself to thank for not giving up at every moment of the suffering. I am also thankful for being lucky enough to have so many people in my life who have helped me.

List of Figures

List of Tables

List of Abbreviations and Symbols

LIBs	Lithium-ion batteries
HEAs	High entropy alloys
HEOs	High-entropy oxides
HEO	High entropy oxide
EC–DMC	Ethylene carbonate–dimethyl carbonate
HEFs	High-entropy fluorides
TEM	Transmission electron microscopy
MS	Mössbauer spectroscopy
EELS	Electron energy loss spectroscopy
XPS	X-ray Photoelectron Spectroscopy
PEO	Polyethylene oxide
PC	Propylene carbonate
EC	Mixture of ethylene carbonate
DMC	Dimethyl carbonate
DEC	Diethyl carbonate
EMC	Ethyl methyl carbonate
SEI	Solid electrolyte interphase
TM	Transition metal
LCO	$LiCoO_2$
OSSE	Octahedral site stabilization energy
SOC	Stability in a high state of charge
NCM	$LiNi_xCo_yMn_{1-x-y}O_2$
NMC-111	$LiNi_{1/3}Mn_{1/3}Co_{1/3}O_2$
HEVs	Hybrid electric vehicles
LATP	$Li_{1.3}Al_{0.3}Ti_{1.7}(PO_4)_3$
LFP	$LiFePO_4$
LCO	$LiCoO_2$
NMC	$LiNiMnCoO_2$
TMOs	Transition metal oxides
HEMs	High entropy materials
MEA	Medium entropy alloy
DRX	Cation-disordered rock salt
SEM	Scanning electron microscopy

SE	Secondary electrons
BSE	Backscattered electrons
CR	Characteristic X-ray radiation
CCD	Charge-coupled device
EELS	Electron energy loss spectroscopy
XRD	X-ray diffraction
XPS	X-ray Photoelectron Spectroscopy
BE	Binding energy of the electron
SEI	Solid electrolyte interphase
EIS	Electrochemical impedance spectroscopy
TM-HEO	Transition metal-based high entropy oxides
RE-HEO	Rare-earth-based high entropy oxides
SPS	Spark plasma sintering methods
HR-TEM	High-resolution TEM
EDX	Energy-dispersive X-ray spectroscopy
ALD	Atomic layer deposition
LiHEO	Lithium-doped high-entropy oxide
OER	Oxygen evolution reaction
ICP-OES	Inductively coupled plasma-optical emission spectroscopy
FWHM	Full width at half maximum
MFs	Metal fluorides
CEI	Cathode solid electrolyte interphase
CV	Cyclic voltammetry
DOS	Total electron density of the states
DFT	Density functional theory
VBM	Valence band maximum
CPE2	Constant phase element
EDX	Energy dispersive X-ray spectroscopy
SAED	Selected area electron diffraction

Curriculum Vitea

Education:

05/2019 – present, Karlsruhe, Germany
PhD candidate at the Institute of Nanotechnology
Technische Universität Darmstadt, TUD and Karlsruhe Institute of Technology, KIT
Supervisor: Prof. Dr.-Ing. Horst Hahn

09/2014 - 06/2017, Qingdao, China
Master in Materials Engineering
Qingdao University of Science and Qingdao Institute of Bioenergy & Bioprocess Technology, CAS
Supervisor: Prof. Guanglei Cui, Prof. Zhihong Liu, Prof. Guangwen Xie

2010. 09-2014. 06, Shandong, China
Bachelor in Materials Physics and Chemistry
Qufu Normal University

Work Experience:

05/2019 - present
Synthesis and Processing of High Entropy Materials and their Integration into Lithium Batteries
Supervisor: Prof. Dr.-Ing. Horst Hahn
Department:Institute of Nanotechnology (INT)
Karlsruhe Institute of Technology, Karlsruhe, Germany

2017. 06-2018. 10
Polymer/ inorganic composite electrolytes for lithium batteries
Department: Solid state energy systems technology center
Qingdao Institute of Bioenergy & Bioprocess Technology, CAS. Qingdao, China

Publications:

Yanyan Cui, Parvathy Anitha Sukkurji, Kai Wang, Raheleh Azmi, Alexandra M. Nunn, Horst Hahn, Ben Breitung, Qingsong Wang, Simon Schweidler, and Miriam Botros, High Entropy Fluorides as Conversion Cathodes with Tailorable Electrochemical Performance. J. Energy Chem. *72 (2022) 342–351.*

Jiangwei Ju, Shanmu Dond, **Yanyan Cui** (Co-first author), Yanfen Zhang, Ben Tang, Feng Jiang, Zili Cui, Huanrui Zhang, Xiaofan Du, Tao Lu, Lang Huang, Guanglei Cui,* and Liquan Chen, Leakage-Proof Electrolyte Chemistry for a High-Performance Lithium-Sulfur Battery. *Angew. Chem. Int. Ed. 2021, 60, 16487–16491.*

Parvathy Anitha Sukkurji, **Yanyan Cui** (Co-first author), Seunghwa Lee, Kai Wang, Raheleh Azmi, Abhishek Sarkara, Sylvio Indris, Subramshu S. Bhattacharya, Robert Kruk, Horst Hahn, Qingsong Wang, Miriam Botros, and Ben Breitung, Mechanochemical Synthesis of Novel Rutile-Type High Entropy Fluorides for Electrocatalysis. *J. Mater. Chem. A,* 2021, 9, 8998–9009.

Zhidong Liu, Huiping Du, **Yanyan Cui,** Li Du, Zhiming Zhao, Xiaohang Wang, Zichuan Lv, Mengjia Sun, Zhiyuan Liu, Kaiming Li, Guoxin Zhang, Meng-Chang Lin, Guanglei Cui, A reliable gel polymer electrolyte enables stable cycling of rechargeable aluminum batteries in a wide-temperature range, J. Power Sources*, 2021, 497, 229839.*

Junbo Wang, **Yanyan Cui**, Qingsong Wang, Kai Wang, Xiaohui Huang, David Stenzel1,Abhishek Sarkar, Raheleh Azmi, Thomas Bergfeldt, Subramshu S. Bhattacharya,Robert Kruk, Horst Hahn, Simon Schweidler, Torsten Brezesinski and Ben Breitung, Lithium containing layered high entropy oxide structures. *Sci Rep 2020, 10, 18430.*

Yanyan Cui, Jingchao Chai, Huiping Du, Yulong Duan, Guangwen Xie, Zhihong Liu, and Guanglei Cui, Facile and Reliable in Situ Polymerization of Poly(Ethyl Cyanoacrylate)-Based Polymer Electrolytes toward Flexible Lithium Batteries. ACS Appl. Mater. Interfaces 2017, 9, 8737-8741.

Yanyan Cui, Xinmiao Liang, Jingchao Chai, Zili Cui, Qinglei Wang, Weisheng He, Xiaochen Liu, Zhihong Liu, Guanglei Cui, and Jiwen Feng, High Performance Solid Polymer Electrolytes for Rechargeable Batteries: A Self-Catalyzed Strategy toward Facile Synthesis. *Adv. Sci. 2017, 4, 1700174.*

Yanyan Cui, Yushu Tang, Tongtong Fu, Horst Hahn, Ben Breitung, Simon Schweidler, and Miriam Botros, Photonic curing assistant for coating high entropy oxide on NCM851005. (in submission)

Patents:

Guanglei Cui, Zili Cui, Lixin Qiao, Sha Yu, **Yanyan Cui**, et.al., A solid-state lithium battery polymer electrolyte: preparation and application, CN201710206478.3A.

Guanglei Cui, Jiangwei Ju, Hongxia Xu, Bingbing Chen, Yantao Wang, **Yanyan Cui,** A polymer conductive fiber toughened sulfide composite electrolyte, CN201711198632.3.

Guanglei Cui, Zhihong Liu, **Yanyan Cui**, et.al, A method for preparing all-solid-state polymer electrolytes via a in situ ring-opening polymerization of epoxy compounds for all-solid-state lithium batteries, CN201610249783.6.

References

[1] M. v. Reddy, A. Mauger, C.M. Julien, A. Paolella, K. Zaghib, Brief history of early lithium-battery development, Materials. 13 (2020).

[2] D. Larcher, J.M. Tarascon, Towards greener and more sustainable batteries for electrical energy storage, Nature Chemistry. 7 (2015) 19–29.

[3] L. Lu, X. Han, J. Li, J. Hua, M. Ouyang, A review on the key issues for lithium-ion battery management in electric vehicles, Journal of Power Sources. 226 (2013) 272–288.

[4] G.G. Eshetu, H. Zhang, X. Judez, H. Adenusi, M. Armand, S. Passerini, E. Figgemeier, Production of high-energy Li-ion batteries comprising silicon-containing anodes and insertion-type cathodes, Nature Communications. 12 (2021) 1–14.

[5] B. Scrosati, J. Garche, Lithium batteries: Status, prospects and future, Journal of Power Sources. 195 (2010) 2419–2430.

[6] Batteries Europe ETIP, Batteries Europe: Strategic Research Agenda for 2020, European Technology and Inovation Platform. ENER-2018- (2015) 9–75.

[7] M.S. Whittingham, Lithium batteries and cathode materials, Chemical Reviews. 104 (2004) 4271–4301.

[8] S. Goriparti, E. Miele, F. De Angelis, E. Di Fabrizio, R. Proietti Zaccaria, C. Capiglia, Review on recent progress of nanostructured anode materials for Li-ion batteries, Journal of Power Sources. 257 (2014) 421–443.

[9] Z. Xue, D. He, X. Xie, Poly(ethylene oxide)-based electrolytes for lithium-ion batteries, Journal of Materials Chemistry A. 3 (2015) 19218–19253.

[10] J.L. Schaefer, Y. Lu, S.S. Moganty, P. Agarwal, N. Jayaprakash, L.A. Archer, Electrolytes for high-energy lithium batteries, Applied Nanoscience (Switzerland). 2 (2012) 91–109.

[11] J. Xie, Y.C. Lu, A retrospective on lithium-ion batteries, Nature Communications. 11 (2020).

[12] M.M. Thackeray, C. Wolverton, E.D. Isaacs, Electrical energy storage for transportation - Approaching the limits of, and going beyond, lithium-ion batteries, Energy and Environmental Science. 5 (2012) 7854–7863.

[13] M.R. Palacín, Recent advances in rechargeable battery materials: A chemist's perspective, Chemical Society Reviews. 38 (2009) 2565–2575.

[14] Y. Yuan, K. Amine, J. Lu, R. Shahbazian-Yassar, Understanding materials challenges for rechargeable ion batteries with in situ transmission electron microscopy, Nature Communications. 8 (2017) 1–14.

[15] N. Nitta, F. Wu, J.T. Lee, G. Yushin, Li-ion battery materials: Present and future, Materials Today. 18 (2015) 252–264.

[16] S. Imtiaz, I.S. Amiinu, Y. Xu, T. Kennedy, C. Blackman, K.M. Ryan, Progress and perspectives on alloying-type anode materials for advanced potassium-ion batteries, Materials Today. 48 (2021) 241–269.

[17] F. Wang, R. Robert, N.A. Chernova, N. Pereira, F. Omenya, F. Badway, X. Hua, M. Ruotolo, R. Zhang, L. Wu, V. Volkov, D. Su, B. Key, M. Stanley Whittingham, C.P. Grey, G.G. Amatucci, Y. Zhu, J. Graetz, Conversion reaction mechanisms in lithium ion batteries: Study of the binary metal fluoride electrodes, J Am Chem Soc. 133 (2011) 18828–18836.

[18] N. Nitta, F. Wu, J.T. Lee, G. Yushin, Li-ion battery materials: Present and future, Materials Today. 18 (2015) 252–264.

[19] N. Tolganbek, Y. Yerkinbekova, S. Kalybekkyzy, Z. Bakenov, A. Mentbayeva, Current state of high voltage olivine structured $LiMPO_4$ cathode materials for energy storage applications: A review, Journal of Alloys and Compounds. 882 (2021).

[20] N. Nitta, F. Wu, J.T. Lee, G. Yushin, Li-ion battery materials: Present and future, Materials Today. 18 (2015) 252–264.

[21] J.M. Kim, X. Zhang, J.G. Zhang, A. Manthiram, Y.S. Meng, W. Xu, A review on the stability and surface modification of layered transition-metal oxide cathodes, Materials Today. 46 (2021) 155–182.

[22] K. Mizushima, P.C. Jones, P.J. Wiseman, J.B. Goodenough, $LixCoO_2$ (0<x~l): A NEW cathode MATERIAL FOR BATTERIES OF HIGH ENERGY DENSITY, 1980.

[23] J.B. Goodenough, Y. Kim, Challenges for rechargeable Li batteries, Chemistry of Materials. 22 (2010) 587–603.

[24] M. Li, J. Lu, Z. Chen, K. Amine, 30 Years of Lithium-Ion Batteries, Advanced Materials. 30 (2018).
[25] N. Taguchi, T. Akita, K. Tatsumi, H. Sakaebe, Characterization of MgO-coated-$LiCoO_2$ particles by analytical transmission electron microscopy, Journal of Power Sources. 328 (2016) 161–166.
[26] J. Qian, L. Liu, J. Yang, S. Li, X. Wang, H.L. Zhuang, Y. Lu, Electrochemical surface passivation of $LiCoO_2$ particles at ultrahigh voltage and its applications in lithium-based batteries, Nature Communications. 9 (2018).
[27] J.N. Zhang, Q. Li, C. Ouyang, X. Yu, M. Ge, X. Huang, E. Hu, C. Ma, S. Li, R. Xiao, W. Yang, Y. Chu, Y. Liu, H. Yu, X.Q. Yang, X. Huang, L. Chen, H. Li, Trace doping of multiple elements enables stable battery cycling of $LiCoO_2$ at 4.6 V, Nature Energy. 4 (2019) 594–603.
[28] Y. Huang, Y. Zhu, H. Fu, M. Ou, C. Hu, S. Yu, Z. Hu, C. Chen, G. Jiang, H. Gu, H. Lin, W. Luo, Y. Huang, Mg-Pillared $LiCoO_2$: Towards Stable Cycling at 4.6 V, Angewandte Chemie - International Edition. 60 (2021) 4682–4688.
[29] Y. Deng, T. Kang, Z. Ma, X. Tan, X. Song, Z. Wang, P. Pang, D. Shu, X. Zuo, J. Nan, Safety influences of the Al and Ti elements modified $LiCoO_2$ materials on $LiCoO_2$/graphite batteries under the abusive conditions, Electrochimica Acta. 295 (2019) 703–709.
[30] L. Liu, Z. Wang, H. Li, L. Chen, X. Huang, Al_2O_3-coated $LiCoO_2$ as cathode material for lithium ion batteries, n.d.
[31] Y.K. Sun, J.M. Han, S.T. Myung, S.W. Lee, K. Amine, Significant improvement of high voltage cycling behavior AlF_3-coated $LiCoO_2$ cathode, Electrochemistry Communications. 8 (2006) 821–826.
[32] G.Q. Liu, H.T. Kuo, R.S. Liu, C.H. Shen, D.S. Shy, X.K. Xing, J.M. Chen, Study of electrochemical properties of coating ZrO_2 on $LiCoO_2$, Journal of Alloys and Compounds. 496 (2010) 512–516.
[33] Y. Lyu, X. Wu, K. Wang, Z. Feng, T. Cheng, Y. Liu, M. Wang, R. Chen, L. Xu, J. Zhou, Y. Lu, B. Guo, An Overview on the Advances of $LiCoO_2$ Cathodes for Lithium-Ion Batteries, Advanced Energy Materials. 11 (2021).
[34] B. Ammundsen, J. Paulsen, Novel Lithium-Ion Cathode Materials Based on Layered Manganese Oxides, n.d.
[35] X. Ma, H. Chen, G. Ceder, Electrochemical Properties of Monoclinic $NaMnO_2$, Journal of The Electrochemical Society. 158 (2011) A1307.
[36] S. Liu, B. Wang, X. Zhang, S. Zhao, Z. Zhang, H. Yu, Reviving the lithium-manganese-based layered oxide cathodes for lithium-ion batteries, Matter. 4 (2021) 1511–1527.
[37] X. Zhu, F. Meng, Q. Zhang, L. Xue, H. Zhu, S. Lan, Q. Liu, J. Zhao, Y. Zhuang, Q. Guo, B. Liu, L. Gu, X. Lu, Y. Ren, H. Xia, $LiMnO_2$ cathode stabilized by interfacial orbital ordering for sustainable lithium-ion batteries, Nature Sustainability. 4 (2021) 392–401.
[38] X.M. Wu, X. Li, S. Chen, Z.E. Qiang, M. Fei Xu, Comparative study of Co, Cr and Al-doped $LiMnO_2$ prepared by ion exchange, 2008.
[39] J. Cho, Y.J. Kim, T.-J. Kim, B. Park, Effect of Al_2O_3 -Coated o-$LiMnO_2$ Cathodes Prepared at Various Temperatures on the 55°C Cycling Behavior, Journal of The Electrochemical Society. 149 (2002) A127.
[40] P. Kalyani, N. Kalaiselvi, Various aspects of $LiNiO_2$ chemistry: A review, Science and Technology of Advanced Materials. 6 (2005) 689–703.
[41] D. Larcher, J.M. Tarascon, Towards greener and more sustainable batteries for electrical energy storage, Nature Chemistry. 7 (2015) 19–29.
[42] J. Zheng, Y. Ye, T. Liu, Y. Xiao, C. Wang, F. Wang, F. Pan, Ni/Li Disordering in Layered Transition Metal Oxide: Electrochemical Impact, Origin, and Control, Accounts of Chemical Research. 52 (2019) 2201–2209.
[43] L. de Biasi, A. Schiele, M. Roca-Ayats, G. Garcia, T. Brezesinski, P. Hartmann, J. Janek, Phase Transformation Behavior and Stability of $LiNiO_2$ Cathode Material for Li-Ion Batteries Obtained from In Situ Gas Analysis and Operando X-Ray Diffraction, ChemSusChem. 12 (2019) 2240–2250.
[44] M. Akhilash, P.S. Salini, B. John, T.D. Mercy, A journey through layered cathode materials for lithium ion cells – From lithium cobalt oxide to lithium-rich transition metal oxides, Journal of Alloys and Compounds. 869 (2021).

[45] C. Zhang, W. Jiang, W. He, W. Wei, Heteroepitaxial interface of layered cathode materials for lithium ion batteries, Energy Storage Materials. 37 (2021) 161–189.
[46] C. Liu, Z.G. Neale, G. Cao, Understanding electrochemical potentials of cathode materials in rechargeable batteries, Materials Today. 19 (2016) 109–123.
[47] H. Zhou, Y. Li, J. Zhang, W. Kang, D.Y.W. Yu, Low-temperature direct synthesis of layered m-$LiMnO_2$ for lithium-ion battery applications, Journal of Alloys and Compounds. 659 (2016) 248–254.
[48] M. Bianchini, M. Roca-Ayats, P. Hartmann, T. Brezesinski, J. Janek, There and Back Again—The Journey of $LiNiO_2$ as aCathode ActiveMaterial, Angewandte Chemie. 131 (2019) 10542–10569.
[49] J. Zhu, G. Chen, Single-crystal based studies for correlating the properties and high-voltage performance of $LiNi_xCo_yMn_{1-x-y}O_2$ cathodes, Journal of Materials Chemistry A. 7 (2019) 5463–5474.
[50] L. Song, J. Du, Z. Xiao, P. Jiang, Z. Cao, H. Zhu, Research Progress on the Surface of High-Nickel Nickel–Cobalt–Manganese Ternary Cathode Materials: A Mini Review, Frontiers in Chemistry. 8 (2020).
[51] T. Ohzuku, Y. Makimura, Layered lithium insertion material of $LiCo_{1/3}Ni_{1/3}Mn_{1/3}O_2$ for lithium-ion batteries, Chemistry Letters. (2001) 642–643.
[52] S.T. Myung, F. Maglia, K.J. Park, C.S. Yoon, P. Lamp, S.J. Kim, Y.K. Sun, Nickel-Rich Layered Cathode Materials for Automotive Lithium-Ion Batteries: Achievements and Perspectives, ACS Energy Letters. 2 (2017) 196–223.
[53] H.J. Noh, S. Youn, C.S. Yoon, Y.K. Sun, Comparison of the structural and electrochemical properties of layered $Li[Ni_xCo_yMn_z]O_2$ (x = 1/3, 0.5, 0.6, 0.7, 0.8 and 0.85) cathode material for lithium-ion batteries, Journal of Power Sources. 233 (2013) 121–130.
[54] W. Li, E.M. Erickson, A. Manthiram, High-nickel layered oxide cathodes for lithium-based automotive batteries, Nature Energy. 5 (2020) 26–34.
[55] L. de Biasi, B. Schwarz, T. Brezesinski, P. Hartmann, J. Janek, H. Ehrenberg, Chemical, Structural, and Electronic Aspects of Formation and Degradation Behavior on Different Length Scales of Ni-Rich NCM and Li-Rich HE-NCM Cathode Materials in Li-Ion Batteries, Advanced Materials. 31 (2019).
[56] J. Kim, H. Cha, H. Lee, P. Oh, J. Cho, Surface and Interfacial Chemistry in the Nickel-Rich Cathode Materials, Batteries and Supercaps. 3 (2020) 309–322.
[57] H. Lv, C. Li, Z. Zhao, B. Wu, D. Mu, A review: Modification strategies of nickel-rich layer structure cathode (Ni ≥ 0.8) materials for lithium ion power batteries, Journal of Energy Chemistry. 60 (2021) 435–450.
[58] J. Zhou, Z. Han, Y. Zhang, A. Zhu, X. He, H. Wu, X. Chen, Q. Wang, Y. Zhang, Design and host-involvedin situfabrication of La_4NiLiO_8coating on Ni-rich cathode materials towards superior structural stability, Journal of Materials Chemistry A. 9 (2021) 3427–3440.
[59] X. Qu, Z. Yu, D. Ruan, A. Dou, M. Su, Y. Zhou, Y. Liu, D. Chu, Enhanced Electrochemical Performance of Ni-Rich Cathode Materials with $Li_{1.3}Al_{0.3}Ti_{1.7}(PO_4)_3$ Coating, ACS Sustainable Chemistry and Engineering. 8 (2020) 5819–5830.
[60] M. Armand, Nature Lithium Battery, Nature. 414 (2001) 359–367.
[61] F. Wu, G. Yushin, Conversion cathodes for rechargeable lithium and lithium-ion batteries, Energy and Environmental Science. 10 (2017) 435–459.
[62] J. Cabana, L. Monconduit, D. Larcher, M.R. Palacín, Beyond intercalation-based Li-ion batteries: The state of the art and challenges of electrode materials reacting through conversion reactions, Advanced Materials. 22 (2010) 170–192.
[63] M. Armand, J.-M. Tarascon, Building better batteries, Nature. 451 (2008) 652–657.
[64] F. Wu, O. Borodin, G. Yushin, In situ surface protection for enhancing stability and performance of conversion-type cathodes, MRS Energy & Sustainability. 4 (2017).
[65] J. Kim, H. Kim, K. Kang, Conversion-Based Cathode Materials for Rechargeable Sodium Batteries, Advanced Energy Materials. 8 (2018) 1–20.
[66] F. Wu, J. Maier, Y. Yu, Guidelines and trends for next-generation rechargeable lithium and lithium-ion batteries, Chemical Society Reviews. 49 (2020) 1569–1614.
[67] N. Zhang, X. Xiao, H. Pang, Transition metal (Fe, Co, Ni) fluoride-based materials for electrochemical energy storage, Nanoscale Horiz. 4 (2019) 99–116.

[68] C. Li, K. Chen, X. Zhou, J. Maier, Electrochemically driven conversion reaction in fluoride electrodes for energy storage devices, Npj Computational Materials. 4 (2018) 22.
[69] M.A. Reddy, B. Breitung, V.S.K. Chakravadhanula, C. Wall, M. Engel, C. Kübel, A.K. Powell, H. Hahn, M. Fichtner, CF_x derived carbon-FeF_2nanocomposites for reversible lithium storage, Advanced Energy Materials. 3 (2013) 308–313.
[70] X. Fan, Y. Zhu, C. Luo, T. Gao, L. Suo, S.C. Liou, K. Xu, C. Wang, In situ lithiated FeF_3/C nanocomposite as high energy conversion-reaction cathode for lithium-ion batteries, Journal of Power Sources. 307 (2016) 435–442.
[71] Q. Chang, Z. Luo, L. Fu, J. Zhu, W. Yang, D. Li, L. Zhou, A new cathode material of NiF_2 for thermal batteries with high specific power, Electrochimica Acta. 361 (2020).
[72] Q. Guan, J. Cheng, X. Li, W. Ni, B. Wang, Porous CoF_2 Spheres Synthesized by a One-Pot Solvothermal Method as High Capacity Cathode Materials for Lithium-Ion Batteries, Chinese Journal of Chemistry. 35 (2017) 48–54.
[73] M. Valvo, C. Floraki, E. Paillard, K. Edström, D. Vernardou, Perspectives on Iron Oxide-Based Materials with Carbon as Anodes for Li- and K-Ion Batteries, Nanomaterials. 12 (2022) 1436.
[74] B. Li, J. Feng, Y. Qian, S. Xiong, Mesoporous quasi-single-crystalline $NiCo_2O_4$ superlattice nanoribbons with optimizable lithium storage properties, Journal of Materials Chemistry A. 3 (2015) 10336–10344.
[75] Y. Kang, C. Deng, Y. Chen, X. Liu, Z. Liang, T. Li, Q. Hu, Y. Zhao, Binder-Free Electrodes and Their Application for Li-Ion Batteries, Nanoscale Research Letters. 15 (2020).
[76] R. Liu, H. Chen, K. Zhao, Y. Qin, B. Jiang, T. Zhang, G. Sha, X. Shi, C. Uher, W. Zhang, L. Chen, Entropy as a Gene-Like Performance Indicator Promoting Thermoelectric Materials, Advanced Materials. 29 (2017).
[77] D. Bérardan, S. Franger, D. Dragoe, A.K. Meena, N. Dragoe, Colossal dielectric constant in high entropy oxides, Physica Status Solidi - Rapid Research Letters. 10 (2016) 328–333.
[78] C.M. Rost, E. Sachet, T. Borman, A. Moballegh, E.C. Dickey, D. Hou, J.L. Jones, S. Curtarolo, J.P. Maria, Entropy-stabilized oxides, Nature Communications. 6 (2015) 1–8.
[79] A. Sarkar, L. Velasco, D. Wang, Q. Wang, G. Talasila, L. de Biasi, C. Kübel, T. Brezesinski, S.S. Bhattacharya, H. Hahn, B. Breitung, High entropy oxides for reversible energy storage, Nature Communications. 9 (2018) 3400.
[80] E. Lökçü, Ç. Toparli, M. Anik, Electrochemical performance of $(MgCoNiZn)_{1-x}Li_xO$ high-entropy oxides in lithium-ion batteries, ACS Applied Materials and Interfaces. 12 (2020) 23860–23866.
[81] J.W. Yeh, S.K. Chen, S.J. Lin, J.Y. Gan, T.S. Chin, T.T. Shun, C.H. Tsau, S.Y. Chang, Nanostructured high-entropy alloys with multiple principal elements: Novel alloy design concepts and outcomes, Advanced Engineering Materials. 6 (2004) 299–303.
[82] B. Cantor, I.T.H. Chang, P. Knight, A.J.B. Vincent, Microstructural development in equiatomic multicomponent alloys, Materials Science and Engineering A. 375–377 (2004) 213–218.
[83] C.M. Rost, E. Sachet, T. Borman, A. Moballegh, E.C. Dickey, D. Hou, J.L. Jones, S. Curtarolo, J.P. Maria, Entropy-stabilized oxides, Nature Communications. 6 (2015) 8485.
[84] J.W. Yeh, Alloy design strategies and future trends in high-entropy alloys, JOM. 65 (2013) 1759–1771.
[85] Y.F. Ye, Q. Wang, J. Lu, C.T. Liu, Y. Yang, High-entropy alloy: challenges and prospects, Materials Today. 19 (2016) 349–362.
[86] J. Liu, X. Wang, A.P. Singh, H. Xu, F. Kong, F. Yang, The evolution of intermetallic compounds in high-entropy alloys: From the secondary phase to the main phase, Metals (Basel). 11 (2021).
[87] E.J. Pickering, N.G. Jones, High-entropy alloys: a critical assessment of their founding principles and future prospects, International Materials Reviews. 61 (2016) 183–202.
[88] R.S. Mishra, R.S. Haridas, P. Agrawal, High entropy alloys – Tunability of deformation mechanisms through integration of compositional and microstructural domains, Materials Science and Engineering A. 812 (2021).
[89] D.B. Miracle, O.N. Senkov, A critical review of high entropy alloys and related concepts, Acta Materialia. 122 (2017) 448–511.
[90] S. v. Divinski, A. v. Pokoev, N. Esakkiraja, A. Paul, A Mystery of "Sluggish Diffusion" in High-Entropy Alloys: The Truth or a Myth?, Diffusion Foundations. 17 (2018) 69–104.

[91] Z. Wang, Q. Fang, J. Li, B. Liu, Y. Liu, Effect of lattice distortion on solid solution strengthening of BCC high-entropy alloys, Journal of Materials Science & Technology. 34 (2018) 349–354.
[92] H.P. Chou, Y.S. Chang, S.K. Chen, J.W. Yeh, Microstructure, thermophysical and electrical properties in $Al_xCoCrFeNi$ ($0 \le x \le 2$) high-entropy alloys, Materials Science and Engineering B: Solid-State Materials for Advanced Technology. 163 (2009) 184–189.
[93] S. Ranganathan, Alloyed pleasures: Multimetallic cocktails, 2003.
[94] D. Bérardan, S. Franger, A.K. Meena, N. Dragoe, Room temperature lithium superionic conductivity in high entropy oxides, Journal of Materials Chemistry A. 4 (2016) 9536–9541.
[95] M. Moździerz, J. Dąbrowa, A. Stępień, M. Zajusz, M. Stygar, W. Zając, M. Danielewski, K. Świerczek, Mixed ionic-electronic transport in the high-entropy $(Co,Cu,Mg,Ni,Zn)_{1-x}Li_xO$ oxides, Acta Materialia. 208 (2021).
[96] Q. Wang, A. Sarkar, Z. Li, Y. Lu, L. Velasco, S.S. Bhattacharya, T. Brezesinski, H. Hahn, B. Breitung, High entropy oxides as anode material for Li-ion battery applications: A practical approach, Electrochemistry Communications. 100 (2019) 121–125.
[97] H. Chen, N. Qiu, B. Wu, Z. Yang, S. Sun, Y. Wang, A new spinel high-entropy oxide $(Mg_{0.2}Ti_{0.2}Zn_{0.2}Cu_{0.2}Fe_{0.2})_3O_4$ with fast reaction kinetics and excellent stability as an anode material for lithium ion batteries, RSC Advances. 10 (2020) 9736–9744.
[98] L. Lin, K. Wang, A. Sarkar, C. Njel, G. Karkera, Q. Wang, R. Azmi, M. Fichtner, H. Hahn, S. Schweidler, B. Breitung, High-Entropy Sulfides as Electrode Materials for Li-Ion Batteries, Advanced Energy Materials. 12 (2022).
[99] J. Yan, D. Wang, X. Zhang, J. Li, Q. Du, X. Liu, J. Zhang, X. Qi, A high-entropy perovskite titanate lithium-ion battery anode, Journal of Materials Science. 55 (2020) 6942–6951.
[100] Q. Wang, A. Sarkar, D. Wang, L. Velasco, R. Azmi, S.S. Bhattacharya, T. Bergfeldt, A. Düvel, P. Heitjans, T. Brezesinski, H. Hahn, B. Breitung, Multi-anionic and -cationic compounds: New high entropy materials for advanced Li-ion batteries, Energy and Environmental Science. 12 (2019) 2433–2442.
[101] C. Zhao, F. Ding, Y. Lu, L. Chen, Y.S. Hu, High-entropy layered oxide cathodes for sodium-ion batteries, Angew. Chem. Int. Ed. 59 (2020) 264–269.
[102] Z. Lun, B. Ouyang, D.H. Kwon, Y. Ha, E.E. Foley, T.Y. Huang, Z. Cai, H. Kim, M. Balasubramanian, Y. Sun, J. Huang, Y. Tian, H. Kim, B.D. McCloskey, W. Yang, R.J. Clément, H. Ji, G. Ceder, Cation-disordered rocksalt-type high-entropy cathodes for Li-ion batteries, Nature Materials. 20 (2021) 214–221.
[103] J. Wang, Y. Cui, Q. Wang, K. Wang, X. Huang, D. Stenzel, A. Sarkar, R. Azmi, T. Bergfeldt, S.S. Bhattacharya, R. Kruk, H. Hahn, S. Schweidler, T. Brezesinski, B. Breitung, Lithium containing layered high entropy oxide structures, Scientific Reports. 10 (2020).
[104] V.M. Sc, S. Abhishek, Development of Fully Printed Oxide Electronics for Flexible Substrates, 2021.
[105] T.B. Daunis, K.A. Schroder, J.W.P. Hsu, Photonic curing of solution-deposited ZrO_2 dielectric on PEN: a path towards high-throughput processing of oxide electronics, Npj Flexible Electronics. 4 (2020).
[106] J. West, J.W. Sears, S. Smith, M. Carter, Photonic sintering – an example: photonic curing of silver nanoparticles, in: Sintering of Advanced Materials, Elsevier, 2010: pp. 275–288.
[107] U.P. Hadley, Probing Inside a Scanning Electron Microscope, 2010.
[108] B.J. Inkson, Scanning Electron Microscopy (SEM) and Transmission Electron Microscopy (TEM) for Materials Characterization, in: Materials Characterization Using Nondestructive Evaluation (NDE) Methods, Elsevier Inc., 2016: pp. 17–43.
[109] R.F. Egerton, An Introduction to EELS, in: R.F. Egerton (Ed.), Electron Energy-Loss Spectroscopy in the Electron Microscope, Springer US, Boston, MA, 2011: pp. 1–28.
[110] A. Ali, Y.W. Chiang, R.M. Santos, X-Ray Diffraction Techniques for Mineral Characterization: A Review for Engineers of the Fundamentals, Applications, and Research Directions, Minerals. 12 (2022).
[111] N. Elgrishi, K.J. Rountree, B.D. McCarthy, E.S. Rountree, T.T. Eisenhart, J.L. Dempsey, A Practical Beginner's Guide to Cyclic Voltammetry, Journal of Chemical Education. 95 (2018) 197–206.

[112] P. Iurilli, C. Brivio, V. Wood, On the use of electrochemical impedance spectroscopy to characterize and model the aging phenomena of lithium-ion batteries: a critical review, Journal of Power Sources. 505 (2021).
[113] A. Sarkar, R. Djenadic, D. Wang, C. Hein, R. Kautenburger, O. Clemens, H. Hahn, Rare earth and transition metal based entropy stabilised perovskite type oxides, J Eur Ceram Soc. 38 (2018) 2318–2327.
[114] A. Sarkar, Q. Wang, A. Schiele, M.R. Chellali, S.S. Bhattacharya, D. Wang, T. Brezesinski, H. Hahn, L. Velasco, B. Breitung, High-entropy oxides: Fundamental aspects and electrochemical properties, Advanced Materials. 31 (2019) 1806236.
[115] M. Biesuz, L. Spiridigliozzi, G. Dell'Agli, M. Bortolotti, V.M. Sglavo, Synthesis and sintering of (Mg, Co, Ni, Cu, Zn)O entropy-stabilized oxides obtained by wet chemical methods, Journal of Materials Science. 53 (2018) 8074–8085.
[116] F. Li, G.J. Zhang, H. Abe, Low-temperature synthesis of high-entropy $(Mg_{0.2}Co_{0.2}Ni_{0.2}Cu_{0.2}Zn_{0.2})O$ nanoparticles via polyol process, Open Ceramics. 9 (2022).
[117] A. Sarkar, R. Djenadic, N.J. Usharani, K.P. Sanghvi, V.S.K. Chakravadhanula, A.S. Gandhi, H. Hahn, S.S. Bhattacharya, Nanocrystalline multicomponent entropy stabilised transition metal oxides, J Eur Ceram Soc. 37 (2017) 747–754.
[118] L. Lin, K. Wang, R. Azmi, J. Wang, A. Sarkar, M. Botros, S. Najib, Y. Cui, D. Stenzel, P. Anitha Sukkurji, Q. Wang, H. Hahn, S. Schweidler, B. Breitung, Mechanochemical synthesis: route to novel rock-salt-structured high-entropy oxides and oxyfluorides, Journal of Materials Science. 55 (2020) 16879–16889.
[119] A.D. Dupuy, X. Wang, J.M. Schoenung, Entropic phase transformation in nanocrystalline high entropy oxides, Materials Research Letters. 7 (2019) 60–67.
[120] M.R. Arefi, S. Rezaei-Zarchi, Synthesis of zinc oxide nanoparticles and their effect on the compressive strength and setting time of self-compacted concrete paste as cementitious composites, International Journal of Molecular Sciences. 13 (2012) 4340–4350.
[121] J. Dąbrowa, M. Stygar, A. Mikuła, A. Knapik, K. Mroczka, W. Tejchman, M. Danielewski, M. Martin, Synthesis and microstructure of the $(Co,Cr,Fe,Mn,Ni)_3O_4$ high entropy oxide characterized by spinel structure, Materials Letters. 216 (2018) 32–36.
[122] N. Qiu, H. Chen, Z. Yang, S. Sun, Y. Wang, Y. Cui, A high entropy oxide $(Mg_{0.2}Co_{0.2}Ni_{0.2}Cu_{0.2}Zn_{0.2}O)$ with superior lithium storage performance, Journal of Alloys and Compounds. 777 (2019) 767–774.
[123] J.B. Goodenough, K.S. Park, The Li-ion rechargeable battery: A perspective, J Am Chem Soc. 135 (2013) 1167–1176.
[124] M. Fichtner, K. Edström, E. Ayerbe, M. Berecibar, A. Bhowmik, I.E. Castelli, S. Clark, R. Dominko, M. Erakca, A.A. Franco, A. Grimaud, B. Horstmann, A. Latz, H. Lorrmann, M. Meeus, R. Narayan, F. Pammer, J. Ruhland, H. Stein, T. Vegge, M. Weil, Rechargeable Batteries of the Future—The State of the Art from a BATTERY 2030+ Perspective, Advanced Energy Materials. (2021).
[125] Z. Ye, L. Qiu, W. Yang, Z. Wu, Y. Liu, G. Wang, Y. Song, B. Zhong, X. Guo, Nickel-Rich Layered Cathode Materials for Lithium-Ion Batteries, Chemistry - A European Journal. 27 (2021) 4249–4269.
[126] S.S. Zhang, Problems and their origins of Ni-rich layered oxide cathode materials, Energy Storage Materials. 24 (2020) 247–254.
[127] Y. Su, G. Chen, L. Chen, Q. Li, Y. Lu, L. Bao, N. Li, S. Chen, F. Wu, Advances and Prospects of Surface Modification on Nickel-Rich Materials for Lithium-Ion Batteries†, Chinese Journal of Chemistry. 38 (2020) 1817–1831.
[128] W. Liu, X. Li, D. Xiong, Y. Hao, J. Li, H. Kou, B. Yan, D. Li, S. Lu, A. Koo, K. Adair, X. Sun, Significantly improving cycling performance of cathodes in lithium ion batteries: The effect of $Al_2O_{0.3}$ and $LiAlO_2$ coatings on $LiNi_{0.6}Co_{0.22}Mn_{0.2}O_2$, Nano Energy. 44 (2018) 111–120.
[129] A. Martens, C. Bolli, A. Hoffmann, C. Erk, T. Ludwig, M. el Kazzi, U. Breddemann, P. Novák, I. Krossing, Coating of NCM 851005 Cathode Material with $Al0@Al_2O_3$ and Subsequent Treatment with Anhydrous HF, Journal of The Electrochemical Society. 167 (2020) 070510.
[130] C. Qin, J. Cao, J. Chen, G. Dai, T. Wu, Y. Chen, Y. Tang, A. Li, Y. Chen, Improvement of electrochemical performance of nickel rich $LiNi_{0.6}Co_{0.2}Mn_{0.2}O_2$ cathode active material by ultrathin TiO_2 coating, Dalton Transactions. 45 (2016) 9669–9675.

[131] F. Schipper, H. Bouzaglo, M. Dixit, E.M. Erickson, T. Weigel, M. Talianker, J. Grinblat, L. Burstein, M. Schmidt, J. Lampert, C. Erk, B. Markovsky, D.T. Major, D. Aurbach, From Surface ZrO_2 Coating to Bulk Zr Doping by High Temperature Annealing of Nickel-Rich Lithiated Oxides and Their Enhanced Electrochemical Performance in Lithium Ion Batteries, Advanced Energy Materials. 8 (2018).
[132] S.W. Lee, M.S. Kim, J.H. Jeong, D.H. Kim, K.Y. Chung, K.C. Roh, K.B. Kim, Li_3PO_4 surface coating on Ni-rich $LiNi_{0.6}Co_{0.2}Mn_{0.2}O_2$ by a citric acid assisted sol-gel method: Improved thermal stability and high-voltage performance, Journal of Power Sources. 360 (2017) 206–214.
[133] P. Yan, J. Zheng, J. Liu, B. Wang, X. Cheng, Y. Zhang, X. Sun, C. Wang, J.G. Zhang, Tailoring grain boundary structures and chemistry of Ni-rich layered cathodes for enhanced cycle stability of lithium-ion batteries, Nature Energy. 3 (2018) 600–605.
[134] I.D. Scott, Y.S. Jung, A.S. Cavanagh, Y. Yan, A.C. Dillon, S.M. George, S.H. Lee, Ultrathin coatings on nano-$LiCoO_2$ for Li-ion vehicular applications, Nano Letters. 11 (2011) 414–418.
[135] L. Wang, J. Qin, Z. Bai, H. Qian, Y. Cao, H.M.K. Sari, Y. Xi, H. Shan, S. Wang, J. Zuo, X. Pu, W. Li, J. Wang, X. Li, Surface Reconstruction of Ni-Rich Layered Cathodes: In Situ Doping versus Ex Situ Doping, Small Structures. 2100233 (2022) 2100233.
[136] J. Sicklinger, M. Metzger, H. Beyer, D. Pritzl, H.A. Gasteiger, Ambient Storage Derived Surface Contamination of NCM811 and NCM111: Performance Implications and Mitigation Strategies, Journal of The Electrochemical Society. 166 (2019) A2322–A2335.
[137] F. Walther, F. Strauss, X. Wu, B. Mogwitz, J. Hertle, J. Sann, M. Rohnke, T. Brezesinski, J. Janek, The Working Principle of a $Li_2CO_3/LiNbO_3$ Coating on NCM for Thiophosphate-Based All-Solid-State Batteries, Chemistry of Materials. 33 (2021) 2110–2125.
[138] F. Reissig, M.A. Lange, L. Haneke, T. Placke, W.G. Zeier, M. Winter, R. Schmuch, A. Gomez-Martin, Synergistic Effects of Surface Coating and Bulk Doping in Ni-Rich Lithium Nickel Cobalt Manganese Oxide Cathode Materials for High-Energy Lithium Ion Batteries, ChemSusChem. 15 (2022).
[139] S. Schweidler, L. De Biasi, G. Garcia, A. Mazilkin, P. Hartmann, T. Brezesinski, J. Janek, Investigation into Mechanical Degradation and Fatigue of High-Ni NCM Cathode Material: A Long-Term Cycling Study of Full Cells, ACS Applied Energy Materials. 2 (2019) 7375–7384.
[140] P.A. Sukkurji, Y. Cui, S. Lee, K. Wang, R. Azmi, A. Sarkar, S. Indris, S.S. Bhattacharya, R. Kruk, H. Hahn, Q. Wang, M. Botros, B. Breitung, Mechanochemical synthesis of novel rutile-type high entropy fluorides for electrocatalysis, Journal of Materials Chemistry A. 9 (2021) 8998–9009.
[141] T. Wang, H. Chen, Z. Yang, J. Liang, S. Dai, High-Entropy Perovskite Fluorides: A New Platform for Oxygen Evolution Catalysis, J Am Chem Soc. 142 (2020) 4550–4554.
[142] X. Hua, R. Robert, L.S. Du, K.M. Wiaderek, M. Leskes, K.W. Chapman, P.J. Chupas, C.P. Grey, Comprehensive study of the CuF2 conversion reaction mechanism in a lithium ion battery, Journal of Physical Chemistry C. 118 (2014) 15169–15184.
[143] M.G. Cottam, D.J. Lockwood, Spin-phonon interaction in transition-metal difluoride antiferromagnets: Theory and experiment, Low Temperature Physics. 45 (2019).
[144] F. Waltz, M.A. Swider, P. Hoyer, T. Hassel, M. Erne, K. Möhwald, M. Adlung, A. Feldhoff, C. Wickleder, F.W. Bach, P. Behrens, Synthesis of highly stable magnesium fluoride suspensions and their application in the corrosion protection of a Magnesium alloy, Journal of Materials Science. 47 (2012) 176–183.
[145] A. Rehmer, K. Scheurell, G. Scholz, E. Kemnitz, Sol-gel-synthesis of nanoscopic complex metal fluorides, Nanomaterials. 7 (2017) 1–13.
[146] W. Tong, G.G. Amatucci, Silver copper fluoride: A novel perovskite cathode for lithium batteries, Journal of Power Sources. 362 (2017) 86–91.
[147] F. Wang, S.W. Kim, D.H. Seo, K. Kang, L. Wang, D. Su, J.J. Vajo, J. Wang, J. Graetz, Ternary metal fluorides as high-energy cathodes with low cycling hysteresis, Nature Communications. 6 (2015) 1–9.
[148] J. Kohl, D. Wiedemann, S. Nakhal, P. Bottke, N. Ferro, T. Bredow, E. Kemnitz, M. Wilkening, P. Heitjans, M. Lerch, Synthesis of ternary transition metal fluorides Li 3MF 6via a sol-gel route as candidates for cathode materials in lithium-ion batteries, Journal of Materials Chemistry. 22 (2012) 15819–15827.

[149] J. Li, L. Xu, K. Wei, S. Ma, X. Liu, Y. Zhao, Y. Cui, In situ forming of ternary metal fluoride thin films with excellent Li storage performance by pulsed laser deposition, Ionics (Kiel). (2020).
[150] C. Li, K. Chen, X. Zhou, J. Maier, Electrochemically driven conversion reaction in fluoride electrodes for energy storage devices, Npj Computational Materials. 4 (2018) 1–15.
[151] Y. Han, J. Hu, C. Yin, Y. Zhang, J. Xie, D. Yin, C. Li, Iron-based fluorides of tetragonal tungsten bronze structure as potential cathodes for Na-ion batteries, Journal of Materials Chemistry A. 4 (2016) 7382–7389.
[152] D. Cao, C. Yin, D. Shi, Z. Fu, J. Zhang, C. Li, Cubic Perovskite Fluoride as Open Framework Cathode for Na-Ion Batteries, Advanced Functional Materials. 27 (2017) 1701130–9.
[153] H. Chen, J. Fu, P. Zhang, H. Peng, C.W. Abney, K. Jie, X. Liu, M. Chi, S. Dai, Entropy-stabilized metal oxide solid solutions as CO oxidation catalysts with high-temperature stability, Journal of Materials Chemistry A. 6 (2018) 11129–11133.
[154] F. Wang, R. Robert, N.A. Chernova, N. Pereira, F. Omenya, F. Badway, X. Hua, M. Ruotolo, R. Zhang, L. Wu, V. Volkov, D. Su, B. Key, M. Stanley Whittingham, C.P. Grey, G.G. Amatucci, Y. Zhu, J. Graetz, Conversion reaction mechanisms in lithium ion batteries: Study of the binary metal fluoride electrodes, J Am Chem Soc. 133 (2011) 18828–18836.
[155] X. Chen, Y. Wu, High-entropy transparent fluoride laser ceramics, Journal of the American Ceramic Society. (2019) 1–7.
[156] Q. Wang, A. Sarkar, D. Wang, L. Velasco, R. Azmi, S.S. Bhattacharya, T. Bergfeldt, A. Düvel, P. Heitjans, T. Brezesinski, H. Hahn, B. Breitung, Multi-anionic and -cationic compounds: new high entropy materials for advanced Li-ion batteries, Energy & Environmental Science. (2019) 17–19.
[157] A.P. O'Mullane, M. Escudero-Escribano, I.E.L. Stephens, K. Krischer, The Role of Electrocatalysis in a Sustainable Future: From Renewable Energy Conversion and Storage to Emerging Reactions, ChemPhysChem. 20 (2019) 2900–2903.
[158] X. Cui, B. Zhang, C. Zeng, S. Guo, Electrocatalytic activity of high-entropy alloys toward oxygen evolution reaction, MRS Communications. 8 (2018) 1230–1235.
[159] T. Wang, H. Chen, Z. Yang, J. Liang, S. Dai, High-Entropy Perovskite Fluorides: A New Platform for Oxygen Evolution Catalysis, J Am Chem Soc. 142 (2020) 4550–4554.
[160] S. Ramasamy, J. Jiang, H. Gleiter, R. Birringer, U. Gonser, Investigation of nanocrystalline FeF2 by Mössbauer spectroscopy, Solid State Communications. 74 (1990) 851–855.
[161] M.C. Troparevsky, J.R. Morris, M. Daene, Y. Wang, A.R. Lupini, G.M. Stocks, Beyond Atomic Sizes and Hume-Rothery Rules: Understanding and Predicting High-Entropy Alloys, Jom. 67 (2015) 2350–2363.
[162] J.W. Stout, S.A. Reed, The Crystal Structure of MnF_2, FeF_2, CoF_2, NiF_2 and ZnF_2, J Am Chem Soc. 76 (1954) 5279–5281.
[163] M.J. Armstrong, A. Panneerselvam, C. O'Regan, M.A. Morris, J.D. Holmes, Supercritical-fluid synthesis of FeF2 and CoF2 Li-ion conversion materials, Journal of Materials Chemistry A. 1 (2013) 10667–10676.
[164] R.D. Shannon, Revised Effective Ionic Radii and Systematic Studies of Interatomic Distances in Halides and Chalcogenides, Acta Crystallographica Section A. 32 (1976) 751–767.
[165] V. Šepelák, A. Feldhoff, P. Heitjans, F. Krumeich, D. Menzel, F.J. Litterst, I. Bergmann, K.D. Becker, Nonequilibrium cation distribution, canted spin arrangement, and enhanced magnetization in nanosized MgFe2O4 prepared by a one-step mechanochemical route, Chemistry of Materials. 18 (2006) 3057–3067.
[166] C.D. Wagner, Auger Parameter in Electron Spectroscopy for the Identification of Chemical Species, Analytical Chemistry. 47 (1975) 1201–1203.
[167] M.C. Biesinger, Advanced analysis of copper X-ray photoelectron spectra, Surface and Interface Analysis. 49 (2017) 1325–1334.
[168] S. Da-Ming, S. Zhao-Qi, L. Ai-Xia, X. Zhi-Yuan, XPS analysis of the oxidation of Ag-MgF_2 cermet film, Vacuum. 52 (1999) 383–386.
[169] E. Quesnel, L. Dumas, D. Jacob, F. Peiró, Optical and microstructural properties of MgF_2 UV coatings grown by ion beam sputtering process, Journal of Vacuum Science & Technology A: Vacuum, Surfaces, and Films. 18 (2000) 2869–2876.
[170] S. Mori, P. Cong, Y. Shinden, H. Nanao, Tribochemical reactions and lubricating effects of fluorinated methanes for Al2O3 ceramic, Tribology Letters. 17 (2004) 83–89.

[171] R. Azmi, M. Masoumi, H. Ehrenberg, V. Trouillet, M. Bruns, Surface analytical characterization of $LiNi_{0.8-y}Mn_yCo_{0.2}O_2$ ($0 \leq y \leq 0.4$) compounds for lithium-ion battery electrodes, Surface and Interface Analysis. 50 (2018) 1132–1137.
[172] C.R. Mariappan, V. Kumar, R. Azmi, L. Esmezjan, S. Indris, M. Bruns, H. Ehrenberg, High electrochemical performance of 3D highly porous Zn0.2Ni0.8Co2O4 microspheres as an electrode material for electrochemical energy storage, CrystEngComm. 20 (2018) 2159–2168.
[173] J. Wang, D. Stenzel, R. Azmi, S. Najib, K. Wang, J. Jeong, A. Sarkar, Q. Wang, P.A. Sukkurji, T. Bergfeldt, M. Botros, J. Maibach, H. Hahn, T. Brezesinski, B. Breitung, Spinel to Rock-Salt Transformation in High Entropy Oxides with Li Incorporation, Electrochem. 1 (2020) 60–74.
[174] R. Azmi, V. Trouillet, M. Strafela, S. Ulrich, H. Ehrenberg, M. Bruns, Surface analytical approaches to reliably characterize lithium ion battery electrodes, Surface and Interface Analysis. 50 (2018) 43–51.
[175] V. Kumar, C.R. Mariappan, R. Azmi, D. Moock, S. Indris, M. Bruns, H. Ehrenberg, G. Vijaya Prakash, Pseudocapacitance of Mesoporous Spinel-Type MCo_2O_4 (M = Co, Zn, and Ni) Rods Fabricated by a Facile Solvothermal Route, ACS Omega. 2 (2017) 6003–6013.
[176] G. Scholz, S. Breitfeld, T. Krahl, A. Düvel, P. Heitjans, E. Kemnitz, Mechanochemical synthesis of MgF_2-MF_2 composite systems (M Combining double low line Ca, Sr, Ba), Solid State Sciences. 50 (2015) 32–41.
[177] A. Sadoc, M. Body, C. Legein, M. Biswal, F. Fayon, X. Rocquefelte, F. Boucher, NMR parameters in alkali, alkaline earth and rare earth fluorides from first principle calculations, Physical Chemistry Chemical Physics. 13 (2011) 18539–18550.
[178] Y. Guo, S. Wuttke, A. Vimont, M. Daturi, J.C. Lavalley, K. Teinz, E. Kemnitz, Novel sol-gel prepared zinc fluoride: Synthesis, characterisation and acid-base sites analysis, Journal of Materials Chemistry. 22 (2012) 14587–14593.
[179] N.A. Matwiyoff, L.B. Asprey, W.E. Wageman, M.J. Reisfeld, E. Fukushima, Fluorine-19 nuclear magnetic resonance studies of diamagnetic fluoride complexes of nickel(IV), palladium(IV), and platinum(IV) in anhydrous hydrogen fluoride solutions, Inorganic Chemistry. 8 (1969) 750–753.
[180] Y. Cui, P.A. Sukkurji, K. Wang, R. Azmi, A.M. Nunn, H. Hahn, B. Breitung, Y.Y. Ting, P.M. Kowalski, P. Kaghazchi, Q. Wang, S. Schweidler, M. Botros, High entropy fluorides as conversion cathodes with tailorable electrochemical performance, Journal of Energy Chemistry. 72 (2022) 342–351.
[181] A. Manthiram, A reflection on lithium-ion battery cathode chemistry, Nat. Commun. 11 (2020) 1550.
[182] L. Wang, Z. Wu, J. Zou, P. Gao, X. Niu, H. Li, L. Chen, Li-free cathode materials for high energy density lithium batteries, Joule. 3 (2019) 2086–2102.
[183] K. Chen, M. Lei, Z. Yao, Y. Zheng, J. Hu, C. Lai, C. Li, Construction of solid-liquid fluorine transport channel to enable highly reversible conversion cathodes, Sci. Adv. 7 (2021) eabj1491.
[184] J. Hu, Y. Zhang, D. Cao, C. Li, Dehydrating bronze iron fluoride as a high capacity conversion cathode for lithium batteries, Journal of Materials Chemistry A. 4 (2016) 16166–16174.
[185] F. Wang, S.W. Kim, D.H. Seo, K. Kang, L. Wang, D. Su, J.J. Vajo, J. Wang, J. Graetz, Ternary metal fluorides as high-energy cathodes with low cycling hysteresis, Nature Communications. 6 (2015) 6668.
[186] J.P. Pender, G. Jha, D.H. Youn, J.M. Ziegler, I. Andoni, E.J. Choi, A. Heller, B.S. Dunn, P.S. Weiss, R.M. Penner, C.B. Mullins, Electrode degradation in lithium-ion batteries, ACS Nano. 14 (2020) 1243–1295.
[187] F. Wu, O. Borodin, G. Yushin, In situ surface protection for enhancing stability and performance of conversion-type cathodes, MRS Energy & Sustainability. 4 (2017) 9.
[188] S.H. Yu, X. Feng, N. Zhang, J. Seok, H.D. Abruña, Understanding conversion-type electrodes for lithium rechargeable batteries, Accounts of Chemical Research. 51 (2018) 273–281.
[189] K. Wei, Y. Zhao, K. Chen, K. Sun, T. Wu, Z. Dong, Y. Cui, C. Zeng, C. Li, Low-Overpotential LiF Splitting in Lithiated Fluoride Conversion Cathode Catalyzed by Spinel Oxide, Advanced Functional Materials. 31 (2021) 2009133.

[190] Q. Huang, T.P. Pollard, X. Ren, D. Kim, A. Magasinski, O. Borodin, G. Yushin, Fading mechanisms and voltage hysteresis in FeF_2-NiF_2 solid solution cathodes for lithium and lithium-ion batteries, Small. 15 (2019) 1804670.
[191] S.W. Kim, K.W. Nam, D.H. Seo, J. Hong, H. Kim, H. Gwon, K. Kang, Energy storage in composites of a redox couple host and a lithium ion host, Nano Today. 7 (2012) 168–173.
[192] X. Fan, E. Hu, X. Ji, Y. Zhu, F. Han, S. Hwang, J. Liu, S. Bak, Z. Ma, T. Gao, S.C. Liou, J. Bai, X.Q. Yang, Y. Mo, K. Xu, D. Su, C. Wang, High energy-density and reversibility of iron fluoride cathode enabled via an intercalation-extrusion reaction, Nature Communications. 9 (2018) 2324.
[193] Y. Zhao, K. Wei, H. Wu, S. Ma, J. Li, Y. Cui, Z. Dong, Y. Cui, C. Li, LiF Splitting catalyzed by dual metal nanodomains for an efficient fluoride conversion cathode, ACS Nano. 13 (2019) 2490–2500.
[194] D. Gordon, Q. Huang, A. Magasinski, A. Ramanujapuram, N. Bensalah, G. Yushin, Mixed metal difluorides as high capacity conversion-type cathodes: impact of composition on stability and performance, Advanced Energy Materials. 8 (2018) 1800213.
[195] C. Villa, S. Kim, Y. Lu, V.P. Dravid, J. Wu, Cu-substituted NiF_2 as a cathode material for Li-ion batteries, ACS Applied Materials and Interfaces. 11 (2019) 647–654.
[196] T. Wang, H. Chen, Z. Yang, J. Liang, S. Dai, High-entropy perovskite fluorides: A new platform for oxygen evolution catalysis, J Am Chem Soc. 142 (2020) 4550–4554.
[197] P.A. Sukkurji, Y. Cui, S. Lee, K. Wang, R. Azmi, A. Sarkar, S. Indris, S.S. Bhattacharya, R. Kruk, H. Hahn, Q. Wang, M. Botros, B. Breitung, Mechanochemical synthesis of novel rutile-type high entropy fluorides for electrocatalysis, Journal of Materials Chemistry A. 9 (2021) 8998–9009.
[198] N. Pereira, F. Badway, M. Wartelsky, S. Gunn, G.G. Amatucci, Iron oxyfluorides as high capacity cathode materials for lithium batteries, Journal of The Electrochemical Society. 156 (2009) A407.
[199] L.Y. Kuo, O. Guillon, P. Kaghazchi, On the origin of non-monotonic variation of the lattice parameters of $Li_{0.2}Ni_{0.13}Mn_{0.54}Co_{0.13}O_2$ with lithiation/delithiation: A first-principles study, Journal of Materials Chemistry A. 8 (2020) 13832–13841.
[200] L.Y. Kuo, O. Guillon, P. Kaghazchi, Origin of Structural Phase Transitions in Ni-Rich $Li_xNi_{0.8}Mn_{0.1}Co_{0.1}O_2$with Lithiation/Delithiation: A First-Principles Study, ACS Sustainable Chemistry and Engineering. 9 (2021) 7437–7446.
[201] I. Hwang, S.K. Jung, E.S. Jeong, H. Kim, S.P. Cho, K. Ku, H. Kim, W.S. Yoon, K. Kang, NaF–FeF_2 nanocomposite: New type of Na-ion battery cathode material, Nano Research. 10 (2017) 4388–4397.
[202] D. Dees, E. Gunen, D. Abraham, A. Jansen, J. Prakash, Alternating Current Impedance Electrochemical Modeling of Lithium-Ion Positive Electrodes, Journal of The Electrochemical Society. 152 (2005) A1409.
[203] J. Hwang, K. Matsumoto, R. Hagiwara, Symmetric Cell Electrochemical Impedance Spectroscopy of $Na_2FeP_2O_7$ Positive Electrode Material in Ionic Liquid Electrolytes, Journal of Physical Chemistry C. 122 (2018) 26857–26864.
[204] R. Tatara, P. Karayaylali, Y. Yu, Y. Zhang, L. Giordano, F. Maglia, R. Jung, J.P. Schmidt, I. Lund, Y. Shao-Horn, The effect of electrode-electrolyte interface on the electrochemical impedance spectra for positive electrode in Li-Ion battery, J Electrochem Soc. 166 (2019) A5090–A5098.
[205] Y.S. Chen, J.F. Kang, B. Chen, B. Gao, L.F. Liu, X.Y. Liu, Y.Y. Wang, L. Wu, H.Y. Yu, J.Y. Wang, Q. Chen, E.G. Wang, Microscopic mechanism for unipolar resistive switching behaviour of nickel oxides, Journal of Physics D: Applied Physics. 45 (2012) 065303.
[206] M. Chhetri, S. Sultan, C.N.R. Rao, Electrocatalytic hydrogen evolution reaction activity comparable to platinum exhibited by the Ni/$Ni(OH)_2$/graphite electrode, Proc Natl Acad Sci U S A. 114 (2017) 8986–8990.
[207] C.J. Jenks, S.L. Chang, J.W. Anderegg, P.A. Thiel, D.W. Lynch, Photoelectron spectra of an $Al_70Pd_{21}Mn_9$ quasicrystal and the cubic alloy $Al_{60}Pd_{25}Mn_{15}$, Physical Review B. 54 (1996) 6301–6306.
[208] K. Rui, Z. Wen, Y. Lu, J. Jin, C. Shen, One-step solvothermal synthesis of nanostructured manganese fluoride as an anode for rechargeable lithium-ion batteries and insights into the conversion mechanism, Advanced Energy Materials. 5 (2015) 1401716.

[209] Y. Huang, R. Ding, D. Ying, W. Shi, Y. Huang, C. Tan, X. Sun, P. Gao, E. Liu, Engineering doping-vacancy double defects and insights into the conversion mechanisms of an Mn-O-F ultrafine nanowire anode for enhanced Li/Na-ion storage and hybrid capacitors, Nanoscale Advances. 1 (2019) 4669–4678.
[210] Z. Fu, C. Li, W. Liu, J. Ma, Y. Wang, Q. Qin, Electrochemical reaction of lithium with cobalt fluoride thin film electrode, Journal of The Electrochemical Society. 152 (2005) E50.
[211] N. Yamakawa, M. Jiang, B. Key, C.P. Grey, Identifying the local structures formed during lithiation of the conversion material, iron fluoride, in a Li ion battery: A solid-state NMR, X-ray diffraction, and pair distribution function analysis study, J Am Chem Soc. 131 (2009) 10525–10536.
[212] X. Hua, A.S. Eggeman, E. Castillo-Martínez, R. Robert, H.S. Geddes, Z. Lu, C.J. Pickard, W. Meng, K.M. Wiaderek, N. Pereira, G.G. Amatucci, P.A. Midgley, K.W. Chapman, U. Steiner, A.L. Goodwin, C.P. Grey, Revisiting metal fluorides as lithium-ion battery cathodes, Nature Materials. 20 (2021) 841–850.
[213] A.W. Xiao, H.J. Lee, I. Capone, A. Robertson, T.U. Wi, J. Fawdon, S. Wheeler, H.W. Lee, N. Grobert, M. Pasta, Understanding the conversion mechanism and performance of monodisperse FeF_2 nanocrystal cathodes, Nature Materials. 19 (2020) 644–654.
[214] P. Poizot, S. Laruelle, S. Grugeon, L. Dupont, J. Tarascon, Nano-sized transition-metal oxides as negative electrode materials for lithium-ion batteries, Nature. 407 (2000) 496–499.
[215] C. Sommer, P. Krüger, J. Pollmann, Quasiparticle band structure of alkali-metal fluorides, oxides, and nitrides, Physical Review B - Condensed Matter and Materials Physics. 85 (2012) 1–7.
[216] L.F. Olbrich, A.W. Xiao, M. Pasta, Conversion-type fluoride cathodes: Current state of the art, Current Opinion in Electrochemistry. 30 (2021) 100779.
[217] S. Kim, J. Liu, K. Sun, J. Wang, S.J. Dillon, P. v. Braun, Improved Performance in FeF_2 Conversion Cathodes through Use of a Conductive 3D Scaffold and Al_2O_3 ALD Coating, Advanced Functional Materials. 27 (2017).
[218] W. Zhang, L. Ma, H. Yue, Y. Yang, Synthesis and characterization of in situ Fe_2O_3-coated FeF_3 cathode materials for rechargeable lithium batteries, Journal of Materials Chemistry. 22 (2012) 24769–24775.